

HPCBS

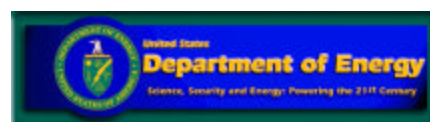
High Performance Commercial Building Systems

Simplified models for heat transfer in rooms

Element 4. Low Energy Cooling
Project 2.3 - Tools and Guides

Guilherme C.C. Carrilho da Graça
University of California, San Diego

2003



Acknowledgement

This work was supported by the California Energy Commission, Public Interest Energy Research Program, under Contract No. 400-99-012 and by the Assistant Secretary for Energy Efficiency and Renewable Energy, Building Technologies Program of the U.S. Department of Energy under Contract No. DE-AC03-76SF00098.

DISCLAIMER

This document was prepared as an account of work sponsored by the United States Government. While this document is believed to contain correct information, neither the United States Government nor any agency thereof, nor The Regents of the University of California, nor any of their employees, makes any warranty, express or implied, or assumes any legal responsibility for the accuracy, completeness, or usefulness of any information, apparatus, product, or process disclosed, or represents that its use would not infringe privately owned rights. Reference herein to any specific commercial product, process, or service by its trade name, trademark, manufacturer, or otherwise, does not necessarily constitute or imply its endorsement, recommendation, or favoring by the United States Government or any agency thereof, or The Regents of the University of California. The views and opinions of authors expressed herein do not necessarily state or reflect those of the United States Government or any agency thereof, or The Regents of the University of California.

This report was prepared as a result of work sponsored by the California Energy Commission (Commission). It does not necessarily represent the views of the Commission, its employees, or the State of California. The Commission, the State of California, its employees, contractors, and subcontractors make no warranty, express or implied, and assume no legal liability for the information in this report; nor does any party represent that the use of this information will not infringe upon privately owned rights. This report has not been approved or disapproved by the Commission nor has the Commission passed upon the accuracy or adequacy of the information in this report.

UNIVERSITY OF CALIFORNIA, SAN DIEGO

Simplified models for heat transfer in rooms

Dissertation submitted in partial satisfaction of the requirements of the degree
Doctor of Philosophy in Engineering Physics

by

Guilherme C.C. Carrilho da Graça

Committee in charge

| | |
|-----------|------------------|
| Professor | Paul Linden |
| Professor | Edward Arens |
| Professor | Colm Caulfield |
| Professor | Philip Haves |
| Professor | Sutanu Sarkar |
| Professor | William R. Young |

2003

...

Copyright

Guilherme C.C. Carrilho da Graça, 2003

All Rights Reserved

The dissertation of Guilherme C.C. Carrilho da Graça
is approved, and it is acceptable in quality and form for
publication on microfilm:

Chair

University of California, San Diego

2003

TABLE OF CONTENTS

| | |
|--|-----|
| Signature Page | iii |
| Table of Contents | iv |
| List of Figures | vii |
| List of Tables | x |
| Vita | xi |
| Abstract | xii |
| Introduction | 1 |
| 1 - Simplified modeling of cross-ventilation flows with recirculation regions. 7 | |
| Introduction..... | 10 |
| 1.1 - Existing approaches..... | 13 |
| 1.2 - Defining the airflow pattern in CV..... | 14 |
| 1.3 - Scaling laws for CV flows with recirculations..... | 29 |
| 1.4 - CFD simulations..... | 35 |
| 1.5 – Results..... | 44 |
| 1.6 – Analysis..... | 56 |
| 1.7 – Applications..... | 57 |
| 1.8 - General guidelines for using the model..... | 73 |
| Conclusion..... | 74 |
| 2 - Heat transfer in cross-ventilated rooms..... | 75 |
| Introduction..... | 78 |
| 2.1 – Air to surface heat transfer in confined flows..... | 80 |
| 2.2 - Global room surface heat transfer coefficient..... | 84 |

| | |
|---|-----|
| 2.3 - Local heat transfer coefficient..... | 106 |
| 2.4. – Validation..... | 113 |
| 2.5 - Heat transfer in recirculating flows with internal gains..... | 122 |
| Conclusions..... | 130 |
| 3 - Multi zone ventilation: a momentum conservation correction for the aperture flow equation..... | 131 |
| Introduction..... | 133 |
| 3.1 - The corrected aperture equation..... | 136 |
| 3.2 - Application to simplified model for pollutant concentration variations in crossventilated rooms..... | 141 |
| 3.3 - Model validation..... | 143 |
| 3.4 – Analysis..... | 147 |
| Conclusions..... | 148 |
| 4 - A simple model for heat transfer in displacement-ventilation..... | 149 |
| Introduction..... | 152 |
| 4.1 – Review of displacement ventilation..... | 156 |
| 4.2 – Theoretical basis for the chosen model representation..... | 171 |
| 4.3 – Description of the model implemented in EnergyPlus..... | 179 |
| 4.4 - Capabilities and limitations of the model..... | 184 |
| Conclusions..... | 186 |
| 5 – Implementation of the models and a flow pattern selection algorithm. | 187 |
| Introduction..... | 188 |
| 5.1 – Criterion for distinction between airflow patterns..... | 192 |
| 5.2 – Example simulations using the CV model in <i>EnergyPlus</i> | 194 |

| | |
|---|-----|
| 5.3 - Simulations using the displacement ventilation model | |
| in <i>EnergyPlus</i> | 198 |
| 5.4 – Example of FPS operation: a free running building with a | |
| solar chimney and night cooling..... | 208 |
| Conclusions..... | 211 |
| Appendix A - Shear layer momentum transfer..... | 216 |
| Appendix B - Heat transfer in a shear layer..... | 221 |
| Appendix C - Simplified analysis of buoyancy effects on the airflow | |
| pattern..... | 224 |
| Appendix D – Software implementation of the model..... | 232 |
| References..... | 244 |

List of Figures

| | |
|---|----|
| Figure 1.1. The three commonly used room ventilation geometries | 10 |
| Figure 1.2. Schematic plan view of a cross-ventilated room | 11 |
| Figure 1.3. Basic compartment geometry considered in the model | 19 |
| Figure 1.4. Top view of the three possible airflow patterns in cross-ventilation. | 20 |
| Figure 1.5. Schematic view of the X velocity profiles and the jet perimeter | 25 |
| Figure 1.6. Plots of momentum, mass flux and pressure variations | 27 |
| Figure 1.7. Surfaces and volumes used for the correlated quantities | 32 |
| Figure 1.8. Plot of the points used in the grid near an internal surface | 36 |
| Figure 1.9. Cross-section view of the room cross-sections used in this study | 40 |
| Figure 1.10. Maximum momentum flux in the recirculation region. | 46 |
| Figure 1.11. Maximum flow rate in the recirculation region. | 47 |
| Figure 1.12. Average velocity in the recirculation region. | 54 |
| Figure 1.13. Average velocity in the recirculation region. | 54 |
| Figure 1.14. Average velocity in the main jet region. | 55 |
| Figure 1.15. Average velocity near the room surfaces. | 55 |
| Figure 1.16. Top view of the four sub regions used to model furniture effects | 57 |
| Figure 1.17. Top view of the positions of the furniture elements used | 58 |
| Figure 1.18. Reductions obtained in the CFD, U_R . | 67 |
| Figure 1.19. Comparison between the reductions obtained in the CFD, U_S . | 67 |
| Figure 1.20. Correlation for turbulent forced convection heat transfer. | 69 |
| Figure 1.21. Average velocity in the jet region | 71 |
| Figure 1.22. Recirculation mass flow rate | 72 |
| Figure 2.1. Typical compartment geometry that leads to cross-ventilation. | 78 |

| | |
|---|-----|
| Figure 2.2. Comparison between free stream and room heat transfer | 80 |
| Figure 2.3. Representation of the global room heat transfer coefficient | 84 |
| Figure 2.4. Variation of the room confinement coefficient C_{CM} with inflow rate | 89 |
| Figure 2.5. Error resulting from approximation in expression 2.11 | 91 |
| Figure 2.6. Temperature calculation points used in the model | 93 |
| Figure 2.7. Variation of the room confinement coefficient with inflow rate | 93 |
| Figure 2.8. Top view of the flow structure in case R | 97 |
| Figure 2.9. Variation of the ratio between h_G for the recirculating airflow | 103 |
| Figure 2.10. Variation of the flow confinement coefficient with inflow rate | 103 |
| Figure 2.11. Average temperature difference in the recirculation region | 104 |
| Figure 2.12. Average value of expression 2.25 | 104 |
| Figure 2.13. Mixed convection heat transfer coefficient | 112 |
| Figure 2.13. Comparison between the predictions of the two models | 118 |
| Figure 2.14. Schematic view of two possible recirculation flow behaviors | 120 |
| Figure 2.15. Vertical plates used to introduce heat gains | 126 |
| Figure 2.16. Comparison between CFD and recirculation region temperatures | 128 |
| Figure 3.1. Experimental setup used by Kato & Murakami | 133 |
| Figure 3.2. Momentum conservation effects in symmetric buoyancy driven case | 134 |
| Figure 3.3. Geometry of the multi-zone building studied | 141 |
| Figure 3.4. Top view of the CFD solution field for case 4 | 143 |
| Figure 3.5. Flow rate through apertures 2 and 3 for the ten cases analyzed | 145 |
| Figure 3.6. Total contaminant flux, rooms 2 and 3 | 146 |
| Figure 3.7. Average concentration in the recirculation region of room 1 | 147 |
| Figure 4.1. Image of a laboratory scaled displacement ventilation flow | 152 |
| Figure 4.2. Variation of the height of the mixed layers in asymmetric plume cases | 167 |

| | |
|--|-----|
| Figure 4.3. Height of the mixed layers with nine equal plumes | 168 |
| Figure 4.4. Three temperature points and temperature gradients | 179 |
| Figure 4.5. The structure of the three-node model | 179 |
| Figure 5.1. Single zone building used to test the implementation of the C—V | 195 |
| Figure 5.2. Predicted temperatures for two summer days in San Francisco | 196 |
| Figure 5.3. Comparison between predicted temperatures for two summer days | 196 |
| Figure 5.4. Predicted temperatures for two summer days in San Francisco | 197 |
| Figure 5.5. Model single zone office building used to test the model | 199 |
| Figure 5.6. Temperatures in the three layers of the displacement ventilation model | 200 |
| Figure 5.7. Room airflow in the variable air volume system | 201 |
| Figure 5.8. Cooling load required by the mixing and displacement systems | 201 |
| Figure 5.9. Temperatures in the displacement natural ventilation system | 203 |
| Figure 5.10. Fractional height of the mixed layer (h/H , squares) | 204 |
| Figure 5.11. The single zone building with a solar chimney attached to the top | 205 |
| Figure 5.12. Temperatures predicted by the displacement ventilation model | 206 |
| Figure 5.13. Temperatures in the displacement natural ventilation system | 207 |
| Figure 5.14. Fractional height of the mixed layer (h/H , in squares) | 208 |
| Figure 5.15. Geometry used to show test the FPS subroutine | 209 |
| Figure 5.16. Results of the simulation of the case shown in figure 5.16 | 210 |
| Figure C.1. Buoyancy driven volumetric flow rate | 231 |
| Figure D.1. Operation sequence for the C—V case “R” modeling subroutine | 237 |
| Figure D.2. Operation sequence for the D-V modeling subroutine | 238 |
| Figure D.3. Organization of the Flow Pattern Selection Algorithm | 240 |

List of Tables

| | |
|--|-----|
| Table 1.1. Dimensions of the apertures used to develop the correlations | 41 |
| Table 1.2. Dimensions of the rooms used to develop the correlations | 41 |
| Table 1.3. Subset of cases used to develop the main correlations | 45 |
| Table 1.4. Subset of cases used to develop the correlations for long rooms | 48 |
| Table 1.5. Subset of cases with C_L smaller than two thirds | 48 |
| Table 1.6. Results of the correlations | 52 |
| Table 1.7. Furniture elements used to develop the correction factors | 62 |
| Table 1.8. Cases used to develop the correction factors E_F | 63 |
| Table 1.9. Corrections to use when furniture areas exceeds criterion 20 | 66 |
| Table 1.10. Comparison between CFD and the correction factors E_F | 66 |
| Table 2.1. Apertures used to develop and test the C-V heat transfer model | 114 |
| Table 2.2. Dimensions of the rooms used to develop and test the correlations | 115 |
| Table 2.3. Results of the simulations for the cases with inflow opening of type D | 116 |
| Table 2.4. Results of the simulations for the cases with inflow opening of type W | 117 |
| Table 2.5. Results of the simulations for the cases with inflow opening of type WD | 118 |
| Table 2.6. Cases used in the validation of the zone temperature estimation | 127 |
| Table 2.7. Cases used in the validation of the recirculation temperature | 128 |
| Table 5.1. Modified input field, to be included in EnergyPlus | 190 |
| Table 5.2. Description of the new input fields | 191 |
| Table 5.3. Basic flow pattern characteristics | 193 |
| Table 5.4. Situations that can lead to transition between flow patterns | 193 |
| Table D.1. Description of the subroutines used in the implementation | 235 |
| Table D.2. New outputs of the displacement ventilation model | 236 |
| Table D.3. New outputs of the CV model | 236 |

Vita

Education

University of California at San Diego (UCSD)

PhD in Engineering Physics (10/99-10/03).

Massachusetts Institute of Technology (MIT)

Master of Science in Building Technology (09/97-05/99).

Instituto Superior Técnico (IST, Lisbon)

Licenciatura in Engineering Physics (09/90-10/95).

Professional Experience

Research Assistant

University of California at San Diego, San Diego, USA
Development of simplified models for heat transfer in building ventilation.

**10/99-
07/03**

Consultant, building physics

Cooperation in several projects and architecture competitions.

09/97-

Research Assistant

Massachusetts Institute of Technology, Boston, USA
Integrated simulation of building natural ventilation.

**03/98-
06/99**

Research Scientist

Ove Arup & Partners, Building Energy Analysis Group,
London, UK
Reengineering of the software ventilation model VENT.

**02/97
–
07/97**

Research Scientist

Departamento de Edifícios (NAI), Laboratório Nacional de
Engenharia Civil, Lisboa, Portugal.
Development and experimental testing of a model for propagation of
structure born noise in buildings.

**10/94
-
01/97**

ABSTRACT OF THE DISSERTATION

Simplified models for heat transfer in rooms

by

Guilherme C.C. Carrilho da Graça

Dissertation submitted in partial satisfaction of the requirements of the degree
Doctor of Philosophy in Engineering Physics

University of California, San Diego, 2003

Professor Paul F. Linden, Chair

Buildings protect their occupants from the outside environment. As a semi-enclosed environment, buildings tend to contain the internally generated heat and air pollutants, as well as the solar and conductive heat gains that can occur in the façade. In the warmer months of the year this generally leads to overheating, creating a need for a cooling system. Ventilation air replaces contaminated air in the building and is often used as the dominant medium for heat transfer between indoor and outdoor environments.

The goal of the research presented in this thesis is to develop a better understanding of the important parameters in the performance of ventilation systems and to develop simplified convective heat transfer models. The general approach used in this study seeks to capture the dominant physical processes for these problems with first order accuracy , and develop simple models that show the correct system behavior trends.

Dimensional analysis, in conjunction with simple momentum and energy conservation, scaled model experiments and numerical simulations, is used to improve airflow and heat transfer rate predictions in both single and multi room ventilation systems.

This study includes the three commonly used room ventilation modes: mixing, displacement and cross-ventilation. A new modeling approach to convective heat transfer between the building and the outside is presented: the concept of equivalent room heat transfer coefficient. The new model quantifies the reduction in heat transfer between ventilation air and internal room surfaces caused by limited thermal capacity and temperature variation of the air for the three modes studied. Particular emphasis is placed on cross-ventilation, and on the development of a simple model to characterize the airflow patterns that occur in this case.

The implementation of the models in a building thermal simulation software tool is presented as well as comparisons between model predictions, experimental results and complex simulation methods. The improved accuracy of the new models, when compared with currently available simple models, is clearly displayed.

Introduction

In many cases, buildings are designed using energy-inefficient indoor climate control systems. This approach is made possible through intensive use of HVAC equipment. These systems ensure adequate temperature and humidity levels at the expense of high energy consumption and increased operational costs. To avoid these problems, naturally driven cooling systems can be employed. In these cases, air movement through the building is powered by buoyancy forces or the wind, or a combination of the two.

In the past, naturally driven cooling systems were the only choice and designers used simple rules-of-thumb. Modern building systems performance standards create a need for accurate and flexible simulation models. Developing improved analysis tools is particularly critical to increased use of low energy, naturally driven cooling systems, because, in these cases, the cooling power is variable and often small.

Modern building systems performance standards create a need for accurate and flexible simulation models that can contribute to better design and increased confidence in the end results. The simple ventilation heat transfer models developed in this thesis can be useful when designing both mechanical and naturally ventilated buildings, still, the main motivation behind this work is to improve simplified modeling of natural ventilation cooling systems, in particular cross-ventilation (CV) geometries.

This thesis presents a study of three commonly used room ventilation geometries: mixing, displacement and cross-ventilation. Mixing ventilation systems are common in

most air-conditioned buildings. In these systems, air is forced to mix by inflow momentum diffusion, leading to the absence of a preferred direction for air motion in the room. CV occurs when the airflow maintains a significant portion of its inflow momentum as it moves across the room. This is in contrast with displacement and mixing ventilation. In displacement ventilation systems, the predominant air movement is vertical, due to heating by internal sources, typically with low momentum fluxes and small horizontal movements across the room.

The two main parts of any room ventilation heat transfer problem are: defining the relevant characteristics of the airflow pattern, and determining the magnitude of the local heat transfer between the airflow in its different paths, internal surfaces and internal heat sources.

Each of the two parts of the problem is a challenge. By definition, any ventilation airflow pattern has a flow component of direct air movement between inlet and outlet, but, as will be clear below, in some regions of the room, air can move in other directions. In the local heat transfer part of this problem, it is clear from energy conservation that all the convective transfer from internal sources and partition surfaces will, at one point in the ventilation process, be transferred to the airflow. Heat transfer between airflow and the internal surfaces depends on the local temperature difference and local heat transfer coefficient. An additional part of the heat transfer problem that also relates to the airflow is determining how much of the energy from the internal gains is transferred to the internal surfaces, therefore not exiting the room in the ventilation air. Clearly, room ventilation heat transfer problems are composed of two sub problems that connect in a

more or less complex way depending on the ventilation system and room geometry. As will become clear in the following parts of this thesis, while mixing ventilation systems are relatively simple to model and understand, displacement ventilation (DV) and cross ventilation (CV) systems pose considerable challenges in both components of the problem.

From a fundamental point of view, all of these four approaches fail in providing simple insight into the mechanisms and system parameters that control the heat transfer process. As mentioned above, high accuracy may be out of scope in this field, simplicity and correct determination of the most relevant parameters and their influence, while keeping first order accuracy (error of less than 30%), is the adequate response to the modeling needs in this area.

For buildings located in hot or mild climates that have a significant amount of thermal mass the cooling load can be substantially reduced by using efficient ventilation strategies [Carrilho da Graça *et al.*, 2001]. Typically, the heat gain removal goals vary from day to night. During the day, it is desirable to remove directly the heat gains or to transfer the gains to the building thermal mass. This transfer is done through the ventilation air and room surfaces. At night, colder outside air can remove heat from the surfaces while heat gains are usually much lower, often negative. Heat transfer between air and room surfaces is important in both of these passive-cooling strategies. Its magnitude has considerable influence on the effective indoor temperature as well as in determining the success of the night cooling system. For similar reasons, an accurate heat transfer model is also relevant to mechanical climate control systems as well as

integrated passive/active systems. Several studies have shown that surface heat transfer has a large impact on energy consumption predictions [Kalema & Haapala, 1995]. Still, the required level of modeling detail is not yet available in most software building simulation tools used today such as DOE [Winkelmann *et al.*, 1993] and TRNSYS [Klein *et al.*, 1976].

The models developed in this thesis are also suitable for integration in current, aperture equation based, simplified ventilation simulation software tools (for a review of these tools see [Feustel *et al.*, 1991]). These tools are adequate for ventilation dimensioning in most design applications. In order to extend its use into more precise building heat transfer analysis, such as EnergyPlus [Crawley *et al.*, 1999], it is necessary to relate accurately the predicted flow rates with the heat transfer between internal room surfaces and ventilation air.

The first part of this thesis presents a simplified model for CV flows with recirculation regions. The model was developed by combining an approximate solution of the Navier-Stokes and energy equations with computational fluid dynamics simulations (CFD) using the low Reynolds number $k\epsilon$ turbulence model. The inputs of the model are the approximate room geometry and the airflow rate. The model extends existing simple models, in order to increase their accuracy and sensitivity to changes in system parameters. The analytical expressions obtained predict characteristic velocities and air flow rates in two regions of the room, the jet and the recirculation region, clearly displaying the controlling parameters for this problem. Applications to design of cross

ventilation systems are presented and the effects of furniture are analyzed in a simple way.

The second part of this thesis presents the extension of the cross ventilation model to heat removal in cross ventilation. In order to analyze internal surface heat transfer (with no internal gains), the concept of a global room surface heat transfer is introduced. The model is validated against CFD simulations. The results show that the average temperature and overall room heat transfer are predicted within the proposed first order accuracy goal.

Part three of this thesis presents an improved multi zone, aperture equation based, building ventilation model. The increased accuracy of this model is obtained by introducing a momentum conservation term in the aperture equation. The model is validated using experimental wind tunnel data and computational fluid dynamics simulations (using the standard $k-\epsilon$ turbulence model) of wind driven CV for several multi zone flow configurations. The corrected aperture equation can be implemented in most existing multi zone aperture equation based ventilation models. The improved model retains the simplicity of current multi zone models while providing increased feedback on the impact of variations in room and building geometry. The improved model is applied to simplified modeling of indoor pollutant removal. The complex transient character of these problems makes a first order accuracy multi zone ventilation model particularly useful in early building ventilation design.

Part four of this thesis presents a simple model for heat transfer in displacement ventilation systems. Criterion for the existence of this ventilation airflow pattern in the presence of heat transfer with the room envelope are developed. Improved quantification of the total heat transfer between ventilation air and building surfaces is achieved.

Part five of this thesis presents the software implementation of the models developed in chapter 1-4 and a study on flow pattern selection resulting in a set of rules that are used to decide between flow patterns in each simulation time step as well as before the simulation. The decision rules and their software implementation are presented as well as an example of the automated use of the flow pattern selection rules in EnergyPlus is presented.

The last section of this thesis presents the conclusions and suggested future developments.

1 - Simplified modeling of cross-ventilation flows with recirculation regions.

Abstract

This chapter presents a study of room cross-ventilation (CV) airflow with emphasis on the recirculation regions, a common feature in these flows. A simplified model is developed using scaling analysis, experimental correlations, computational fluid dynamics, and approximate solutions of the Navier Stokes equation. Simple criterion defining the existence and distinguishing between different types of CV inconsistent flows are established. The model distinguishes two regions in the room, the main jet region and the recirculations, and predicts relevant flow features that are essential inputs when predicting heat and pollutant transfers as well as indoor thermal comfort conditions. A set of analytical expressions are developed, allowing for approximate prediction of airflow rates and characteristic velocities in the jet and recirculation flow regions. The formulas clearly display the first order effects of room geometry and inflow characteristics on CV airflow.

Nomenclature

- A^* : room non dimensional cross-section area ratio.
- A_F : furniture cross-section area (m^2).
- A_{IN} : inlet area (m^2).
- A_R : cross sectional area of the main jet flow in the room (m^2).
- C_D : discharge coefficient for flow through an aperture (non-dimensional).
- C_F : flow rate correlation constant.
- C_J : correlation constant for the average velocity in the room volume occupied by inlet jet flow.
- C_L : flow scaling non-dimensional criterion.
- C_M : momentum correlation constant.
- C_n : correlation constant for correlation index " n ".
- C_{RJ} : correlation constant for the ratio between jet and recirculation velocity.
- C_R : recirculation velocity correlation constant.
- D : shear layer width (m).
- E_F : furniture correction coefficient (non-dimensional).
- F : scaling law function.
- F_{IN} : inlet flow rate (in m^3/s , given by $U_{IN} \cdot A_{IN}$).
- F_R : flow rate in the recirculation region (m^3/s).
- H : room height (m).
- L^* : room non-dimensional length ratio.
- L : room length (m).
- L_F : position (in the x direction) where furniture is placed (m).

M : momentum flux of the jet (in N or J/m).
 P : pressure (pa).
 u : X-axis velocity (m/s).
 U_J : average velocity in the room volume occupied by inlet jet flow (m/s).
 U_M : maximum velocity in the room (m/s).
 U_R : averaged velocity in a given region of the room that is being modeled (m/s).
 U_x : x component of the flow velocity (m/s).
 W_{IN} : width of the inlet aperture (m).
 W : width of the room (m).
 v : Y-axis velocity (m/s).
 b : function that models the variation of the shear layer velocity profile.
 d : size of the boundary layer (m).
 n_L : kinematic viscosity (N.s/m²).
 n_T : equivalent turbulent kinematic viscosity induced component (N.s/m²).
 s : experimentally determined constant that scales mixing in the shear layer.

1 – Introduction

In order to protect occupants and contents from outside conditions, buildings create a semi-enclosed environment that tends to contain internally generated heat and pollutants, as well as solar and conductive heat gains that occur in the façade. In the warmer months of the year this generally leads to overheating, creating a need for a cooling system. The ventilation air that replaces contaminated air throughout the building is often the predominant medium for transfer of heat and pollutants between indoor and outdoor environments.

In many cases, buildings are designed using energy-inefficient indoor climate control strategies. This approach is made possible

through intensive use of HVAC equipment. To mitigate these problems, naturally-driven cooling systems can be employed with air movement through the building being driven by buoyancy forces, or the wind, or a combination of the two. In these systems, the cooling power is variable and often small, making performance simulation and consequent design decisions more challenging and critical to overall success.

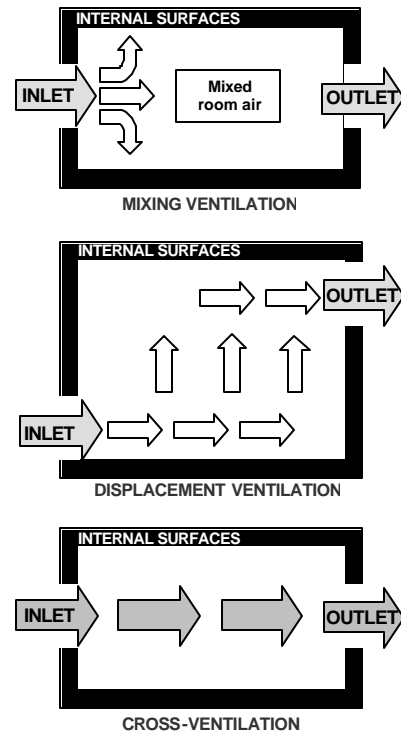


Figure 1.1

Schematic lateral views of the three commonly used room ventilation geometries: mixing, displacement and cross-ventilation. Gray arrows indicate higher momentum flux.

When trying to control the way ventilation air flows through a room, designers often attempt to obtain one of the three ventilation strategies shown schematically in Figure 1.1: mixing, displacement and cross-ventilation (CV). Mixing ventilation systems are used in most air-conditioned buildings, where cool inflow air introduced through vents near the ceiling mixes with room air, with the resultant

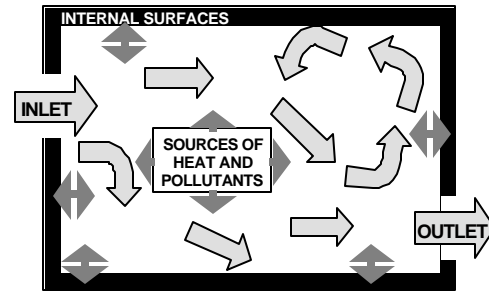


Figure 1.2

Schematic plan view of a cross-ventilated room. Dark gray arrows represent heat flow; light gray arrows represent airflow with significant momentum conservation.

momentum diffusion leading to the absence of a preferred direction for air motion in the room. In displacement ventilation systems, the predominant air movement is vertical, due to buoyancy production by internal heat sources, typically with low momentum fluxes and small horizontal movements across the room. Both of these ventilation flows contrast with CV, where significant conservation of inflow momentum occurs with the inflow traveling freely across the room.

Because of the high momentum conservation, CV strategies are often used when there is need for high ventilation airflow rates. Flows that occur in many naturally ventilated buildings belong to this category, with air flowing through windows, open doorways and large internal apertures across rooms and corridors in the building. This also occurs in many industrial mechanical ventilation systems and hybrid ventilation systems, for both direct heat and pollutant removal and nighttime structural cooling.

CV behavior can also occur in poorly designed mixing ventilation systems, when undesirable short-circuiting occurs between inlet and outlet. ASHRAE [ASHRAE, 2001] classifies this type of flows as entrainment flow. Conversely, cross-ventilated rooms with

recirculation regions fit the ASHRAE [ASHRAE, 2001] definition of entrainment flow and exhibit the characteristic poor mixing between different zones in the room.

Figure 1.2 shows a schematic plan view of a cross-ventilated room with internal gains and thermally active internal surfaces. In order to model heat and pollutant transfer and evaluate thermal comfort, two interrelating components of the CV system must be modeled. These components are: the airflow pattern (light gray arrows in Figure 1.2), and the magnitude of the local transfers of heat and pollutants between the airflow in its different paths, the internal surfaces and heat/pollutant sources (dark gray arrows in Figure 1.2).

Each of the two parts of the problem poses considerable challenges. By definition, any CV airflow pattern has an element of direct air movement between inlet and outlet, but, as will be clear below, in some regions of the room air can move in other directions. In the local heat and pollutant transfer part of this problem, it is clear from conservation principles that all convective and advective transfers from room surfaces and internal sources will, at one point in the ventilation process, be transferred to the airflow. Transfers between airflow and the internal sources depend on the local concentration gradient and transfer coefficient. In particular, when modeling heat transfer, it is relevant to determine how much energy from the internal gains is transferred to the internal surfaces, and not exhausted by the ventilation air. Clearly, room ventilation transfer problems are composed of two sub-problems that connect in a more or less complex way depending on the ventilation system and room geometry. The model described in this chapter will address the definition of the airflow pattern and the convective part local transfer coefficients in CV.

1.1 - Existing approaches

In order to predict airflow characteristics in CV, there are currently three available options: computational fluid dynamics (CFD, typically using Reynolds averaged turbulence models and LES), zonal models, and experimental correlations.

The use of CFD requires extensive expertise and time. In many design situations the need to analyze multi-room ventilation geometries using weather data spanning several days or months makes CFD impractical and simpler ventilation models are more appropriate. Further, in most of these cases, the accuracy level and amount of information required and provided by CFD can be excessive. Often the building geometry and internal furniture elements are not fully defined, making simple modeling approaches and results better than complex flow field simulations.

Zonal models simulate indoor airflow by solving for mass and momentum conservation in a set of zones (often less than twenty). These models generally require user identification of the dominant room airflow components (jets, boundary layers, plumes, etc.) that occupy particular zones of the room. Because the momentum equation is not solved in the iteration procedure, an artificial flow resistance is often imposed between room zones [Allard & Inard, 1992]. As a result static pressure variations and airflow pattern are incorrectly predicted in most cases.

Experimental empirical correlations provide a simple way to model complex ventilation systems such as CV [Givoni, 1976, Aynsley *et al.*, 1977, Ernest *et al.*, 1991]. The simplicity of use of these correlations is a positive aspect, however, because the correlations are obtained for particular geometries, they lack flexibility to handle variable room geometries.

From a fundamental point of view, all of these three approaches fail to provide simple insights into the mechanisms and system parameters that control the CV airflow pattern. As mentioned above, high accuracy may not be required for the design of a cross-ventilated room or building. Simplicity and qualitative identification of the most relevant room geometry parameters and their influence in the airflow pattern is more relevant.

When seeking a simple solution approach for a complex problem such as CV airflow one must accept a trade off in model accuracy. Therefore, in the present model first order accuracy is expected and considered acceptable in view of physical system complexity and other uncertainties that are common in building ventilation design, such as furniture geometry, building use, and outside weather conditions.

1.2 - Defining the airflow pattern in CV

The left side of Figure 1.3 shows a simple room geometry that can lead to CV, with an inlet window facing an outlet on an opposing room surface. To develop the simple model, it will be necessary to make approximations that will simplify the analysis while retaining the ability to model the dominant characteristics of the problem. Achieving this in the present case requires the use of two types of approximations: in the characterization of the physical processes and in the system geometry.

The main approximations in the system geometry are the following.

1. The model is restricted to rectangular rooms with flat surfaces.
2. Air enters the room through one aperture and leaves through an aperture located in the opposing vertical surface (as shown in Figure 1.3).
3. The effects of furniture are not considered in detail (see section 1.7.1).
4. The effects of variations in outlet geometry are neglected.

With regard to 4, Ref. [Baturin & Billington, 1972] shows experimental evidence of the small magnitude of the effects of outlet geometry, confirmed in the CFD simulations presented below. With these approximations, only five parameters are needed to characterize room geometry in the model: width W , height H , length L , area A_{IN} of the inlet aperture, and position of the inlet aperture (close to the center or close to the perimeter of the inlet surface).

We begin the analysis of the approximations used in the physical processes with a discussion of the flow regime, a fundamental question when characterizing any airflow pattern. CV airflows can be seen as an interaction between several “flow elements”: a jet, flat surface boundary layers, shear layers, and stagnation regions. All of these “flow elements” have been studied in detail in the past and their basic behavior can be predicted using simple physical models or correlations. In order to use existing models it is necessary to identify these elements in the CV flow and determine the flow regime in which they occur.

CV flows tend to be turbulent in most regions of the room. The main system features that contribute to a turbulence dominated flow are.

?large characteristic room dimensions (typical room depths (L) around: 5-15 m), combined with flow velocities close to the inlet aperture that typically vary between 0.2 and 2 m/s (Reynolds number based on inflow is always higher than 10^4);

?the existence of turbulent “flow elements” interacting in a confined space, such as: the shear layers that begin at the edge of the inlet aperture and expand as the air travels towards the outlet, and the boundary layers that occur close to the room surfaces (see Figs. 1.3, 1.5 and 1.6).

?significant velocities close the room surfaces (0.1-1m/s). These velocities are generally higher than those commonly found in rooms with HVAC systems.

The shear layers that occur in room airflow have a small laminar region (smaller than 0.1m [Bejan, 1994]). In horizontal forced convection boundary layers, transition to turbulence occurs within the first one half meter (for a forced flow free stream velocity of 0.1m/s or higher [Neiswanger *et al.*, 1987]). Additional sources of turbulence are: jets impinging on room surfaces, flow around furniture, room corners, and most internal heat sources (generation of turbulent kinetic energy through buoyancy induced flow). Between the different flow elements that can occur in CV, there may be regions of light shear, almost stagnant flow. Because most of the momentum transfer occurs in turbulent regions the flow is dominated by turbulent processes and these regions of laminar flow will not be modeled explicitly. However, the presence of these laminar regions is

considered implicitly, since, due to the lower momentum transfer that characterizes them, they form boundaries that establish the spatial limits of the main flow regions.

The CV flows to which the model applies are bounded by a stationary geometry, have fixed airflow rates and are dominated by horizontal momentum flux, as opposed to buoyancy dominated (which typically occurs in displacement ventilation). For ventilation systems with these characteristics, if the flow regime is stable (either laminar, or, as in the present case, dominated by turbulence), the flow pattern will also be stable, approximately self similar and suitable for the application of scaling analysis principles. In these flows, all the velocities in the room are expected to scale linearly with the characteristic velocity of the inlet flow:

$$U_R = C_n \cdot f(L, W, H, A_{IN}, \dots) \cdot U_{IN} \quad (1.1)$$

The function f is expected to depend on L , W , H , A_{IN} , and inlet location. Using dimensional analysis principles it is possible to compose two non-dimensional parameters by using the three independent length scales in this problem:

- 1.The square root of the inlet area.
- 2.The square root of the room cross section ($A_R=W.H$).
- 3.The room length in the CV direction.

The two independent parameters that the function f will depend on are:

$$L^* = \frac{L}{\sqrt{A_{IN}}} , A^* = \frac{A_R}{A_{IN}} \quad (1.2)$$

The velocity scale (U_{IN}) of the inlet jet, is defined using inflow momentum flux:

$$M = \int_{A_{IN}} r \cdot (U_{MAX} g(r))^2 dA, \quad U_{IN} = \sqrt{M/r A_{IN}} \quad (1.3)$$

Inflow momentum flux is one of three possible choices for velocity scaling: inflow momentum flux, kinetic energy flux and mass flux. The correlations developed in section 1.3 will be based on momentum flux arguments, making the scaling in expression 1.3 an obvious choice. Still, it is important to note that, as a result of using a self similar inflow velocity profile ($g(r)$), the final correlation results do not depend on the inflow velocity scaling principle used (different multiplying constants appear in the result depending on the scaling used).

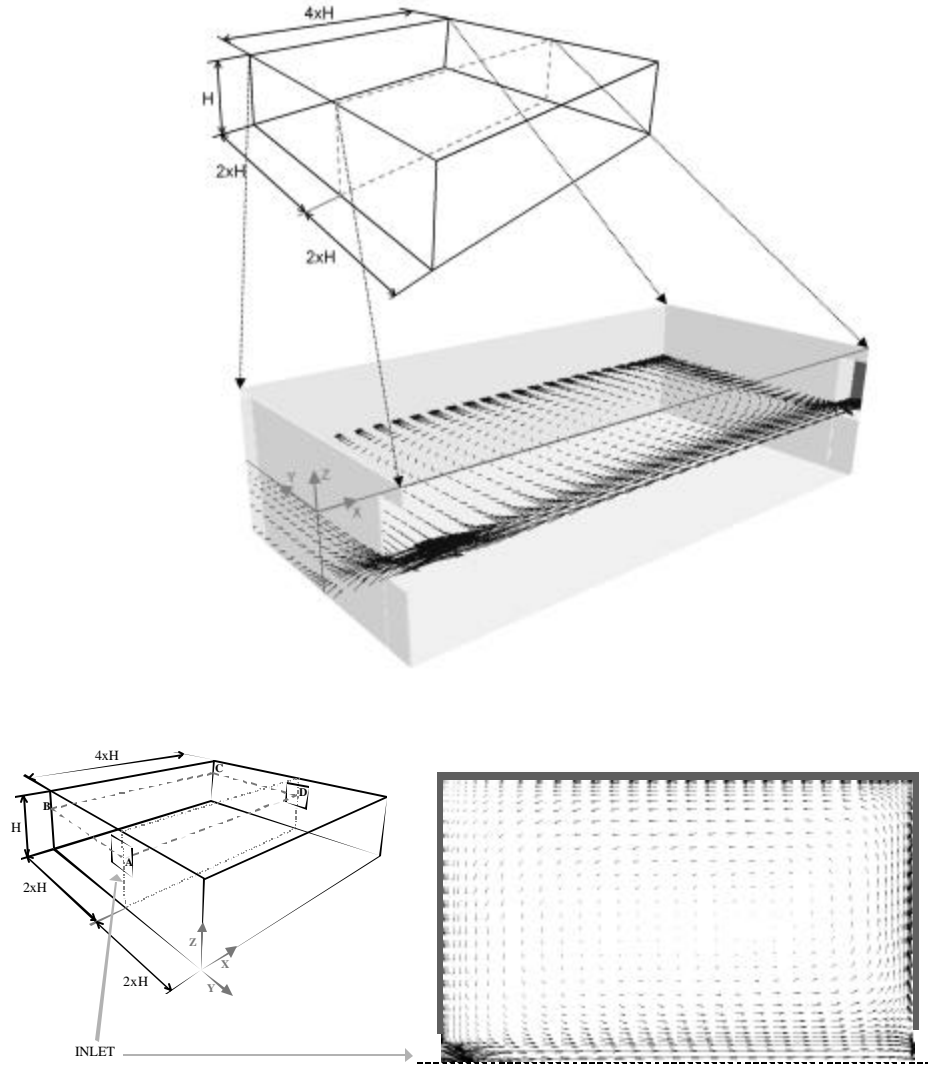


Figure 1.3

Left: basic compartment geometry considered in the model (case W144 in Table 1.3). The room height is H and the length (L) is measured between points B and C. Right: top view of one half of the velocity field (at height $H/2$), result of a CFD simulation using the geometry on the left (taking advantage of the system symmetry to simulate only one half of the room volume)

In order to correlate the velocities in different regions of the room the corresponding correlation constants C_n (on the right hand side of (1.1)) and scaling laws f must be

obtained. By multiplying the velocities predicted using expression 1.1 by the area over which the recirculation flow occurs (in the plane perpendicular to the CV flow direction) correlations for flow rates can be obtained. The remainder of this section will focus on defining the flow pattern in CV rooms.

1.2.1 - The three types of flow pattern

Figure 1.4 shows a schematic representation of the three basic airflow patterns that can occur in CV. Any cross-ventilated room will have an airflow pattern that is either similar to one of the two base cases shown in Figure 1.4 (cases C and R), or a combination of the two with both recirculation and inlet flow attaching to a lateral surface or the ceiling (case CR).

The simplest flow configuration, case C, commonly occurs in corridors and long spaces whose inlet aperture area is similar to the room cross-sectional area. In this case, the flow occupies the full cross section of the room and the transport of pollutants and momentum is unidirectional, similar to turbulent flow in a channel. The flow velocity

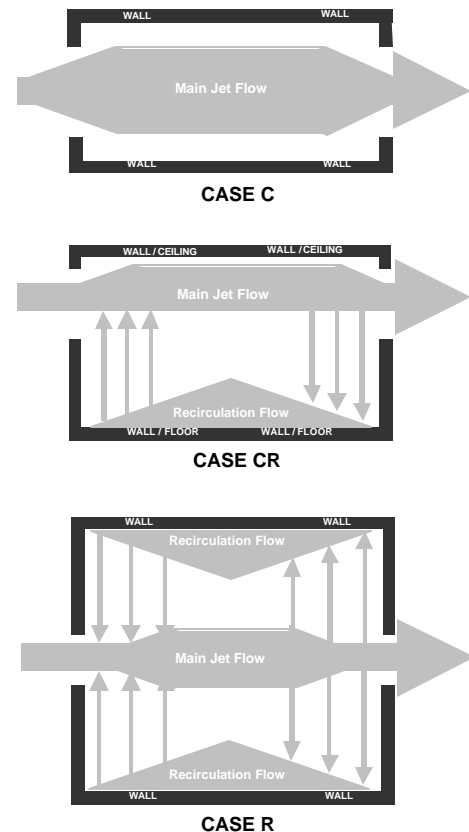


Figure 1.4
Top view of the three possible airflow patterns in cross-ventilation.

profile across the channel is approximately flat as a result of the high degree of mixing that is characteristic of turbulent flows. The average airflow velocity in the cross section can be obtained approximately by dividing the flow rate by the cross sectional area of the space.

A more complicated airflow pattern occurs when the inlet aperture area is an order of magnitude smaller than the cross sectional area of the room $A_R = W.H$ (for the case shown in Figure 1.3, $A_R = 4.H^2$). In these cases, the main CV region in the core of the room entrains air from the adjacent regions and forms recirculations that ensure mass conservation, with air moving in the opposite direction to the core jet flow (see case R and CR in Figure 1.4). These recirculating flow regions have been observed in many experiments. The most relevant to the present problem are [Aynsley *et al.*, 1977, Baturin & Billington, 1972, Neiswanger *et al.*, 1987, Ohba *et al.*, 2001]. In these room geometries, when the inlet is located close to the center of the inlet surface, most of the contact between ventilation flow and the internal surfaces occurs in the recirculation regions that occupy the majority of the room volume.

A set of CFD simulations (described in section 4), based on geometries similar to Fig. 1.3, confirmed the relation between the non-dimensional coefficient A^* (in (1.2)) and the flow pattern. Based on this coefficient it is possible to distinguish between the three cases presented in Fig. 1.4:

- Case C, $A^* @ 1$:** the flow attaches to the room surfaces and is similar to turbulent flow in a channel.
- Case R, $A^* >> 1$:** the flow can be divided in two regions: the jet region (connecting the inlet and the outlet), and the recirculation region, composed of

the return flow that occurs along the cross flow perimeter of the room. In the recirculation region, the maximum velocity occurs close to the internal surfaces and the flow is similar to an attached jet (a wall jet).

Case CR, $A^* @2$: a combination of cases *R* and *C*. The jet flow attaches to part of the room perimeter (as in case *C*). But, in most cases, the recirculation flow occupies the majority of the room.

Most rooms have inlets that are almost one order of magnitude smaller than the room cross-section, resulting in a flow pattern closer to case *R* or *CR*. Since the characterization of the flow in case *C* is straightforward, the following analysis will discuss geometries of types *R* and *CR*. These geometries present a considerable challenge because the transport of heat and pollutants is not unidirectional and there is no analytical solution for the room airflow pattern.

1.2.2 - Characterization of the flow in the recirculation region

As a first step, we analyze the CFD generated velocity field in the horizontal plane of a cross-ventilated room, shown on the right hand side of Fig. 1.3. The flow in the recirculation regions is composed by wall “currents” resembling attached jets that form close to the outlet and are re-entrained in the first half of the path of the inflow jet in the room. These wall currents are bounded by a boundary layer in the region adjacent to the internal surfaces, and, as will be shown below, are subject to pressure gradients that are a consequence of the presence of the inflow jet in a confined space.

The recirculation regions are a fundamental part of this CV flow. The effectiveness of the mixing between recirculating and main jet flows will determine the flow rate of the recirculation flow and the airflow velocities in this region (average velocity in the occupied zone and close to the internal surfaces). The flow rate in the recirculation region determines the capacity of the recirculating flow to absorb and release heat and pollutants without significant concentration variations. Finally, prediction of the velocities in the main jet and recirculation regions are essential for estimating comfort and meeting particular design goals (such as maximum and minimum indoor velocities). Because there is no analytic solution for the flow field in the room, the need for a correlation arises as a simple solution to account for room confinement and energy dissipation effects. In the process of developing the correlation, the dominant physical processes in this flow will be identified and modeled. Due to the importance of jets in the airflow pattern, it is useful to review here the most relevant aspects of jet flow for the present problem.

1.2.3- Characterization of the flow in the jet region

The jets that occur in CV are approximately axisymmetric for most of the propagation path in the room provided there is no contact with a room surface. Whenever the jet is close to a room surface, attachment occurs and a wall jet is generated. The velocity scale of the jets can be adequately represented by the average inlet velocity ($U_{JET} \gg U_{IN}$, see (1.3)), and the characteristic diameter is $\approx \sqrt{A_{IN}}$.

Jets entrain ambient fluid throughout the propagation path leading to a continuous increase of their mass flow rate. In the initial part of the propagation path, a jet is essentially a shear layer that develops along the perimeter of the inlet aperture (see Fig. 1.5). When the shear layer reaches the center of the jet, so that it occupies it fully, the jet enters the transition stage and a self-similar, Gaussian, velocity profile is formed. This transition stage is initiated between 4 to 8 jet characteristic diameters from the inlet, and ends at around 20 diameters [Tennekes & Lumley, 1994, Malmstrom *et al.*, 1997]. In the transition stage, the amplitude of the jet starts to decay.

Because most building apertures have diameters close to one meter, most jets that occur in CV do not reach the transition stage in the room (this is the case for the jet shown in Figure 1.3), possibly reaching the beginning of this transition stage for very long rooms. This should not be surprising since CV by definition is characterized by significant momentum flux conservation and a jet in the transition region spreads, increasing the likelihood of contact with room surfaces, and consequent momentum loss.

It should be noted that common building apertures, such as doors and windows (not preceded by a corridor with the same cross-section as the aperture), result in an inlet

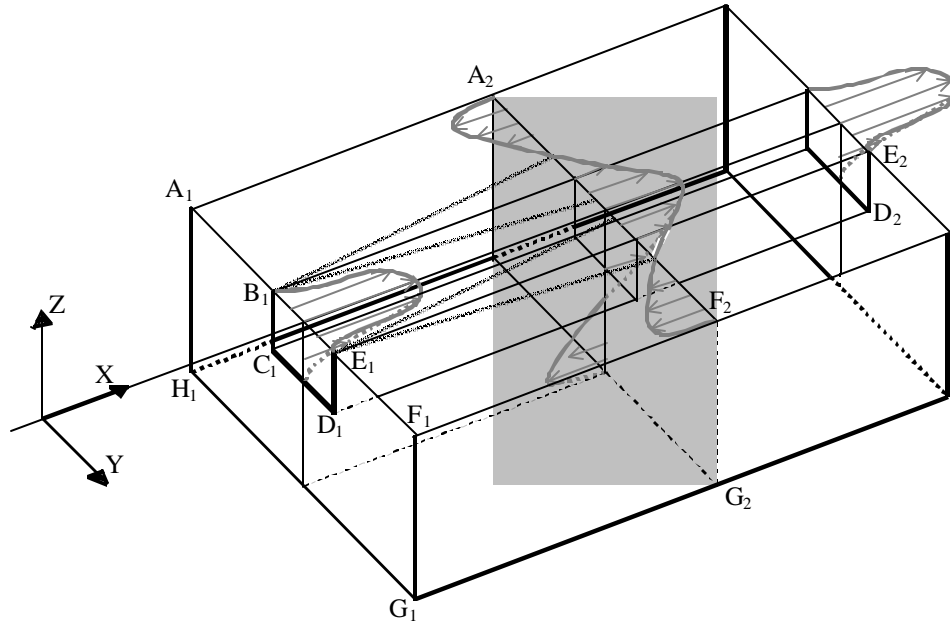


Figure 1.5

Schematic view of the X velocity profiles and the jet perimeter shear layer in the lower half of a cross-ventilated room with a flow of type R.

flow that has significant radial velocity due to flow convergence just before the inlet. This is distinct from the flat, two dimensional inflow velocity profile that is characteristic of experiments with jets. However, the jets that occur in CV flows have shear layers developing from the inlet and a nearly flat inlet velocity profile (in the vena contracta region that occurs after the inlet). Further, it will become clear below that any effects from non-square velocity profiles that may exist in the flow are considered in the correlation process by using integral analysis in conjunction with extensive CFD simulations.

As consequence of mass continuity, the jet rejects air close to the outlet, a clear display of confinement effects, typically in the last third of its propagation path in the room (this is shown schematically in Fig. 3.4, cases R and CR). Because there is mass rejection, as opposed to entrainment, the flow in this region cannot be classified as a jet.

The magnitude of the confinement effects in the flow can be scaled by comparing the characteristic jet diameter with the room dimensions. Typically, room surfaces are less than ten jet diameters away from the core of the jet at any point of its path in the room. This proximity results in non-negligible static pressure and jet momentum flux variations inside the room along with significant momentum flux in the recirculation (although never dominant when compared with inlet momentum flux). As room dimensions tend towards two orders of magnitude bigger than the jet diameter, the jet tends towards free jet behavior [Hussein *et al.*, 1994]. In this case, the momentum flux in the recirculation flow becomes very small as a result of the return flow occurring in a large area (when scaled by the inlet area, $A^* \approx 100$).

Fig. 1.6 shows plots of mass and momentum flux variations in the room (both fluxes across the Y-Z plane) for the case plotted in Figure 1.3. As expected, from mass conservation principles, the mass flow rate in the return flow varies in proportion with the variations in the mass flow rate of the jet. The plots shown in figure 1.6 were obtained by post processing the result file of a CFD simulation (see details in section 1.4) using post processing routines implemented in *Mathematica 3.0* [Wolfram *et al.*, 2002]. A computational volume is considered to be in the jet region whenever its x velocity component is higher than 5% of the average inflow velocity.

The momentum fluxes show a similar behavior but, in this case, with more complex implications. The recirculation flux is a negative flux of negative momentum (negative X velocity). Therefore, both momentum fluxes are positive and increase simultaneously resulting in a total momentum flux that has a maximum close to two thirds of the way along the room. The pressure at the mid-plane level varies, as expected, in opposition to the momentum: a minimum occurs close to halfway along the room. When entering the

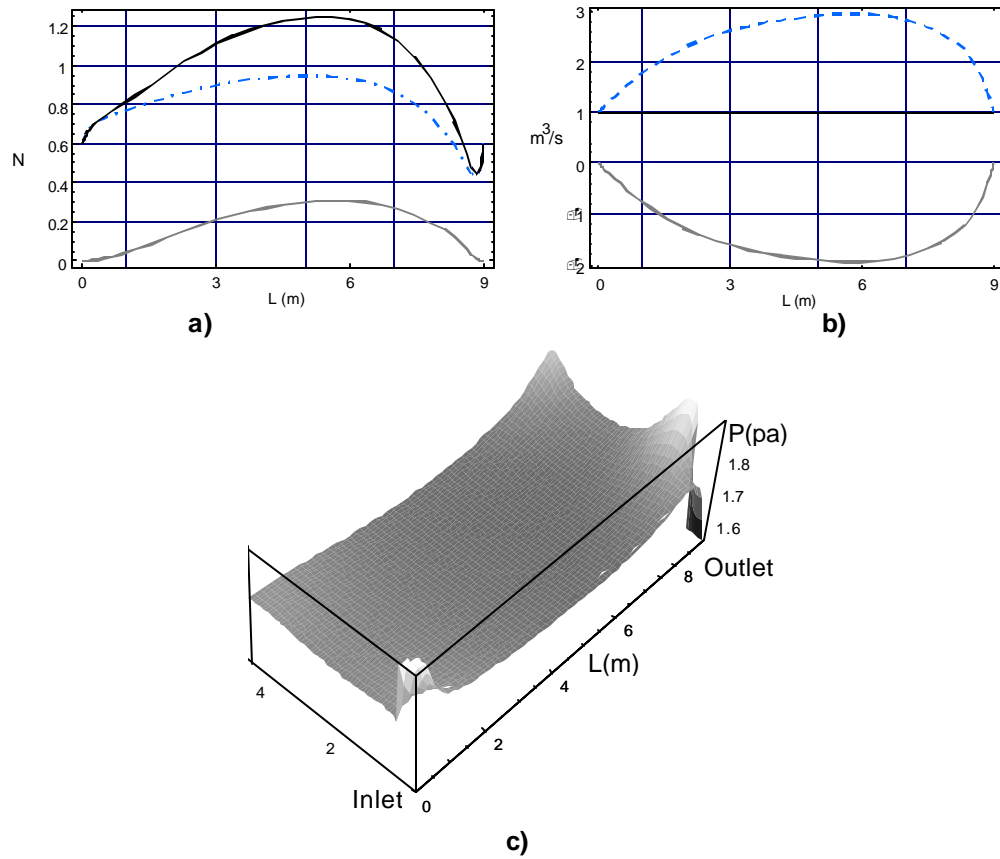


Figure 1.6

Plots of momentum, mass flux and pressure variations for the case plotted in figure 1.3.

a) Momentum flux in the X direction across the cross section of the C—V flow (N). b) Mass flux in the X direction in the cross section of the C-V flow (m^3/s). In both plots: dashed line - total flux in the jet region of the flow - gray line: total flux in the recirculation region, black line - total in the flow. .c) One half of the symmetrical pressure field at one half of the room height.

room the jet is accelerated by a negative pressure gradient. Since the recirculation flow occurs in the opposite direction, this same pressure gradient also reduces the momentum of the recirculation flow. Air from the recirculation flow is entrained into the jet in a shear layer with a velocity scale U_{IN} (close to the inlet, the velocity of the recirculation flow is negligible). A positive pressure gradient occurs close to the outlet, an effect of the

main jet flow reaching the outlet. This pressure gradient is associated with the deflection of part of the main jet, starting the recirculation flow.

This analysis of Figure 1.6 allows for a clearer picture of the flow behavior in the room. As the inlet jet propagates across the room, momentum is transferred to the room air, creating an entrainment-driven recirculation flow moving in the opposite direction, with a mass flow rate equal to the entrained flow in the main jet. The total momentum flux of the inflow jet is not constant: as the jet entrains, its momentum flux increases as a consequence of the pressure gradient visible in the lower corner of figure 1.6 c). In the second half of the propagation path through the room the external pressure gradient opposes the jet and the momentum flux decreases. Although the jet does not conserve its momentum (it is subjected to a significant pressure gradient), the recirculation receives and conserves, in the mass rejection stage (close to the outlet), the momentum flux that occurs between the jet and the room air in the entrainment process.

The pressure gradient generated by the inlet jet flow dominates and determines the flow in the recirculation region. This flow has a momentum flux that is approximately one order of magnitude lower than the main jet momentum flux. The momentum flux through the inlet aperture is the dominant feature in the CV flow.

The main conclusion from this section is: scaling wall currents in the recirculations using the inlet jet flow is the key to modeling recirculation flow. In particular, we identify the flux of momentum through the inlet aperture as the dominant flow feature and the driving mechanism for the recirculation flow. This momentum flows into the room in the form of a jet whose characteristic dimension is typically not more than an order of magnitude smaller than the room length, resulting in a jet flow that is never fully

developed and strongly confined. The remaining sections of this part of the thesis present the development of this concept and the demonstration of its applicability.

1.3 - Scaling laws for CV flows with recirculations

If the correlation functions that will be developed are successful, it will be possible to obtain simple analytical expressions that characterize room airflow parameters (both in the main jet region and in the recirculation). In order to obtain the scaling relations without solving the problem explicitly the following approximations are used:

- ? Pressure variations inside the room are not considered. Although there is an assumption that pressure gradients scale with inlet momentum flux, the model will not explicitly include the pressure gradients in the correlation scaling.
- ? Variations in the momentum flux in the CV direction will not be considered.
- ? Effects of drag on the indoor surfaces, and consequent energy dissipation are neglected.
- ? It is considered that the jet never enters the transition stage before the mass rejection region close to the outlet; consequently, the jet can be modeled as a set of shear layers that develop in its perimeter and never intercept in the core of the jet (see appendix A).
- ? The analysis will only consider movements in the inflow direction. In some cases there are relevant movements in other directions particularly in rooms with offset apertures.

? The maximum room cross-section area occupied by the recirculation flow is considered to be a constant fraction of the total room cross-section area. The CFD simulation section shows that this fraction is close to one half for a large array of common room geometries. In this way, the cross section area of the recirculation flow is considered to scale linearly with the room cross section.

? We will consider that all maximum values in the recirculation flow occur in the same location in the room, approximately two thirds along the length, at the point where the main jet flow enters the mass rejection stage. The maximum values that are relevant to the correlations are: the fractional area occupied by the flow, the average velocity, the momentum flux, and the mass flux.

Quantifying the individual impact of each of the approximations discussed above is impossible. The combined result of not considering these effects is shown in the overall error of the correlations presented below, in some cases the error is higher than 100%. Existing work on simple scaling of indoor airflows is well summarized in [Etheridge & Sandberg, 1996]. No models exist for scaling recirculation flows. Ref. [Jackman, 1970] presents an experimentally validated scaling law, based on the existence of a direct scaling relation between inflow momentum flux and overall momentum flux in the room (without distinguishing regions in the flow). The scaling law predicts the average velocity inside rooms with small inlets and high ratio between momentum and mass fluxes (unlike the inlets considered in this study, windows and doors, that typically have small momentum to mass flux ratios). The inlet momentum flux scaling assumption proposed by [Jackman, 1970] forms the basis of one of the two scaling hypotheses that will be tested in this paper.

Inlet momentum flux is the source of the flow in the room and the interface for inflow/room flow interaction is the shear layer that develops along the perimeter of the inflow jet. For this reason, both inlet and shear layer momentum flux are candidate concepts to form the base of the recirculation flow scaling law. The two hypotheses will be tested to scale the momentum flux in the recirculation flow are then:

1. Inlet momentum flux.
2. Momentum flux through the jet shear layer.

The second of these hypotheses goes deeper into the governing physics of the flow, if confirmed it will have identified the driving mechanism of recirculation flow. After the momentum flux is scaled, all other relevant CV scaling laws can be based on the momentum scaling principle used.

The inflow momentum flux based scaling principle relies on the following sequence of assumptions: pressure variations in the room are proportional to the inlet momentum flux, these pressure variations cause the changes in the return momentum flux of the room air in the recirculation regions. The result of this hypothesis is the following scaling relation between inlet and return momentum flux:

$$Dp \approx r A_R U_R^2 \Rightarrow A_R U_R^2 \approx A_{IN} U_{IN}^2 \Rightarrow U_R^2 = C_M \frac{A_{IN}}{A_R} U_{IN}^2 = C_M \frac{1}{A^*} U_{IN}^2 \quad (1.4)$$

The right side of (1.4) is the product of: a correlation constant (C_M , to be obtained using the CFD simulations), and a non-dimensional function that depends on the room

geometry parameters that are more influential in this balance of momentum fluxes (see function f in Equation 1.1, in the case of (1.4): $f=1/A$).

A generic scaling function for this problem has the following form:

$$f = (\sqrt{A_{IN}})^m \cdot (\sqrt{A_R})^n \cdot L^p \quad (1.5)$$

When the correlation function f in (1.5) is cast in this form it leads to: $m=2$, $n=-2$ and $p=0$. There is no limit to the number of possible combinations of the variables in the exponent (m , n and p) that ensure the necessary non-dimensionality ($m+n+p=0$).

A shear layer based scaling seems more adequate than inflow momentum flux since it not only depends on inlet momentum flux but also scales the net effect of the shear layer flow driving mechanism. This correlation hypothesis is obtained by using $m=1$, $n=-2$ and $p=1$, resulting in:

$$U_R^2 = C_M \frac{\sqrt{A_{IN}} \cdot L}{A_R} \cdot U_{IN}^2 \quad (1.6)$$

This scaling relation can also be obtained from a simplified solution of the Navier Stokes equations, by evaluating the momentum flux

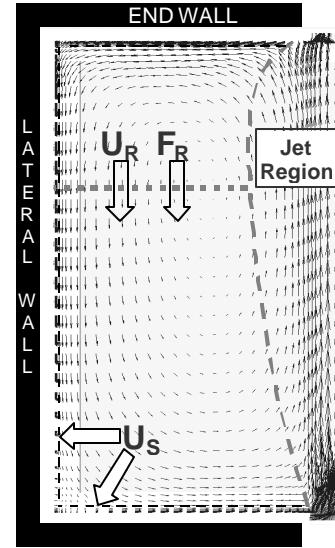


Figure 1.7

Surfaces and volumes used for the calculation of the averaged correlated quantities in a typical CV CFD simulation. As discussed the average velocity and flow rate (U_R , F_R) are estimated in the plane with maximum recirculation momentum flux.

through the shear layer that develops in the perimeter of the inflow jet (see Appendix A). Expressions (1.5) and (1.6) differ in the replacement of the square root of A_{IN} by the room length L . According to the shear layer based correlation (1.6), longer rooms generate higher recirculation momentum fluxes (for constant A^*).

By manipulating (1.4) and (1.6) it is possible to obtain correlations for velocity and flow rate in the recirculation region. A correlation for estimating the average air velocity, essential to estimate forced convection, pollutant advection and occupant thermal comfort in this region can be obtained by defining an average velocity in the cross section of the room area occupied by recirculation flow (see Fig. 1.7). As shown below, this area scales with A_R . Starting from (1.4) we obtain:

$$U_R = C_U \cdot \sqrt{\frac{A_{IN}}{A_R}} \cdot U_{IN} = C_U \cdot \frac{F_{IN}}{\sqrt{A_R \cdot A_{IN}}} \quad (1.7)$$

Multiplying the scaling relation for the average return velocity by the room cross sectional area results in a correlation for the average flow rate:

$$F_R \approx U_R A_R \Rightarrow F_R = C_F \sqrt{\frac{A_R}{A_{IN}}} \cdot F_{IN} \quad (1.8)$$

Similarly for the correlation principle shown in (1.6):

$$U_R = C_U \sqrt{\frac{A_{IN}^{1/2} L}{A_R}} U_{IN} = C_U \sqrt{\frac{L}{A_R \cdot A_{IN}^{3/2}}} F_{IN} \quad (1.9)$$

$$F_R \approx U_R A_R \Rightarrow F_R = C_F \sqrt{\frac{L A_R}{A_{IN}^{3/2}}} \cdot F_{IN} \quad (1.10)$$

In addition to these correlations, it is also necessary to obtain a scaling relation for the average airflow velocity in the volume occupied by the main jet flow in CV flows with recirculations. For this correlation, the inflow momentum scaling (1.4) will be used, an obvious choice given that this flow region is directly in front of the inlet:

$$A_R \cdot U_J^2 \approx A_{IN} \cdot U_{IN}^2 \Rightarrow U_J = C_{UJ} \cdot \frac{F_{IN}}{\sqrt{A_R \cdot A_{IN}}} \quad (1.11)$$

Finally, it is useful to develop a correlation for the near surface velocity. The near surface velocities are dominated either by the characteristic jet region velocity (in the regions where the jet attaches to the indoor surfaces) or by the recirculation flow velocity.

In this context, the near surface velocity can be expected to be a combination of the two scaling laws (1.7) and (1.9):

$$U_S = C_U \sqrt{\frac{L / \sqrt{A_{IN}} (1 - M_C) + M_C}{A_R \cdot A_{IN}}} F_{IN}, \quad (1.12)$$

where M_C is a parameter that characterizes the relative weight of each scaling principle in this correlation for near surface velocity.

Using the non-dimensional room constants, L^* and A^* from (1.2), the correlation expressions above can be cast in a more compact form:

$$\begin{aligned}
 \text{Eqn. (1.9): } U_R &= C_U \sqrt{\frac{L^*}{A^*}} U_{IN} & \text{Eqn. (1.11): } U_J &= C_{UJ} \frac{1}{\sqrt{A^*}} U_{IN} \\
 \text{Eqn. (1.10): } F_R &= C_R \sqrt{L^* A^*} F_{IN} & \text{Eqn. (1.12): } U_S &= C_U \sqrt{\frac{L^* + M_c^2}{A^*}} U_{IN}
 \end{aligned} \tag{1.13}$$

In order to test these correlations and obtain the necessary correlation constants that minimize the modeling error, a set of simulations in cross-ventilated rooms was performed. These simulations are described in the next section.

1.4 - CFD simulations

During the last decade, the use of CFD by researchers and consultants to model engineering flows has been steadily increasing. The main difficulty when using CFD is the choice and application of Reynolds averaged turbulence models [Wilcox, 2000]. Of the several models available, the ke model [Wilcox, 2000] is a common choice because, in many engineering design situations, it can be sufficiently accurate and is relatively simple to use. For this reason, it is often used when simulating indoor and outdoor/indoor isothermal building airflow.

The ke model introduces two equations to model turbulent kinetic energy (k) and its dissipation (ϵ), the results of the solution of these two equations is then used to calculate

an isotropic turbulent kinetic viscosity that is introduced in the momentum equation. There are several significant drawbacks to this simple averaged turbulence model. One is the use of constants in the two equations that depend on the flow modeled or version of the model $k\epsilon$ used. Internal room airflows contain many components that would require distinct sets of constants (attached boundary layers, jets, plumes). An additional problem when applying these models in wall-bounded flows is the modeling of flow regions close to the solid surfaces.

Because the standard $k\epsilon$ model is biased towards simplicity and computational efficiency, the region close to the solid boundaries is not solved numerically, as a way of avoiding the fine resolution needed to handle the high gradients that occur in these regions (in k , ϵ and in the velocity parallel to the solid boundary [Wilcox, 2000]). In this region, the standard $k\epsilon$ approach is to use interpolation functions, commonly known as wall functions, that model the high gradients of k and ϵ near the wall. The results obtained when using wall functions, in particular the value of the turbulence quantities and their consequent influence in the flow pattern, depend on the size of the cells adjacent to the indoor surfaces (measured along the normal direction). It is from this point that the wall functions are connected in the solution of the problem, interpolating the turbulent kinetic

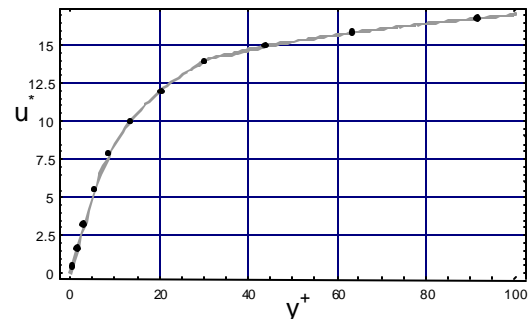


Figure 1.8

Plot of the points used in the grid near an internal surface.

The gray line is a plot of the standard turbulent boundary log law profile, linear for $y^+ < 5$. The plot changes with free stream velocity. The grid was set up so that at least four points are place in the viscous sub layer for free stream velocities of up to 0.5m/s. For definition of u^+ and y^+ see Ref. [Bejan, 1994].

energy and the associated dissipation in the high gradient region between this point and the wall.

In order to avoid this error source, a low Reynolds number near wall approach can be used, extending the numerical solution of the flow to the region close to the internal surfaces, by using a fine grid in the direction of the dominant flow gradients (that are perpendicular to the surface). As in the case of the $k\epsilon$ model used for the “core” region of the flow, there are several alternative low Reynolds number near wall approaches. The simulations presented here use the standard $k\epsilon$ and the low Reynolds number model proposed by Lam & Bremhost [Lam & Bremhost, 1981]. Ref. [Henks & Hoogendoorn, 1989] shows that this model is among the best low Reynolds number turbulence models ($LRk\epsilon$) for predicting velocity and temperature in a natural convection boundary layer. For the cases presented below, preliminary test simulations revealed noticeable differences in the near wall velocities predicted by the low Reynolds number and the wall function approach, reaching 30% for many cases and showing little grid dependence. Clearly, for systems where wall effects are important, an accurate near wall model is essential.

When using the $LRk\epsilon$ model, setting up the calculation grid near the internal surfaces is a critical point. Enough definition must be used so that the model can capture the high gradients mentioned above, in particular in the viscous sub layer region. The size of this region is inversely proportional to the characteristic velocity of the flow near the surface. One problem that occurs in these cases is that the boundary layers have different characteristic velocities and consequently the characteristic dimension of the viscous sub layer varies in different surface locations along the room. For this reason, it is impossible to have a consistent number of viscous sub layer grid points in all the boundary layers in

a given simulation. The near surface grid used, plotted in Figure 1.8, has 11 grid points at less than 0.02m from the room walls and five grid points in the viscous sub layer region.

The simulations were performed using the commercial CFD package, PHOENICS version 3.3 [PHOENICS, 2000]. Among the many options available PHOENICS proved to be the best choice as no other package had all the three turbulence models used in this study. Simulations were considered converged when the normalized residuals were smaller than 10^{-3} and the solution field was stable (the values did not change by more than 10^{-7} (relative change) in each iteration and showed no visible fluctuation or changes after hundreds of iterations). The results files of the simulations were post processed in order to obtain the momentum flux in the recirculation flow and the other flow characteristics that will be correlated below. Results of simulations for different flow rates showed a linear variation of the velocities in the room with inlet velocity, as expected.

As mentioned above, recirculation flow is characterized by negative X velocity and jet region flow occurs where: $U_x > 0$. The velocities near the surface (see U_s in Fig. 1.7) are determined by finding the parallel to surface plane that has the maximum average velocity among all the cell planes that are within 0.1 m from each surface.

1.4.1 - Cases simulated

Appropriate variations of the room geometry were used for all the parameters in the correlations. The values used conform to the restrictions dictated by common

applications in building ventilation, as well as a set of restrictions imposed by the approximations in the model. The rules used were:

? The average inlet velocity should be lower than 2m/s. This rule typically results in maximum velocities close to 1.5m/s in the core of the room, a common upper limit imposed by comfort concerns in naturally ventilated spaces.

? The lower limit used for the average inlet velocity was 0.33 m/s. This limit results from two physical restrictions. First, for lower velocities, stagnation and other buoyancy induced effects can have significant interference in the flow, changing the expected flow pattern that is the basis of the model. Second, turbulent dominated conditions must be ensured in order for the correlations to apply. Natural ventilation flows usually meet or exceed this flow speed. Using this limit leads to an inflow Reynolds number that is always higher than 10^4 .

? Height: 2.25-3.40 m, the lower limit is the common minimum height for a room. The upper limit corresponds to a tall room but does not reach the minimum height for a typical atrium. The model is not applicable to an atrium due to expected buoyancy effects that can change the flow pattern.

? Length: 2.25-13.5 m, the lower limit is typical of small rooms. The upper limit ensures that simulated room jets will be in the developing region for most of the path in the room.

? Width: 2.25-9m, the lower limit ensures that the jet does not attach to the lateral surfaces and recirculation occurs in the flow (one on each side of the main jet flow in the symmetric rooms). The upper limit ensures that the return flow has significant velocity.

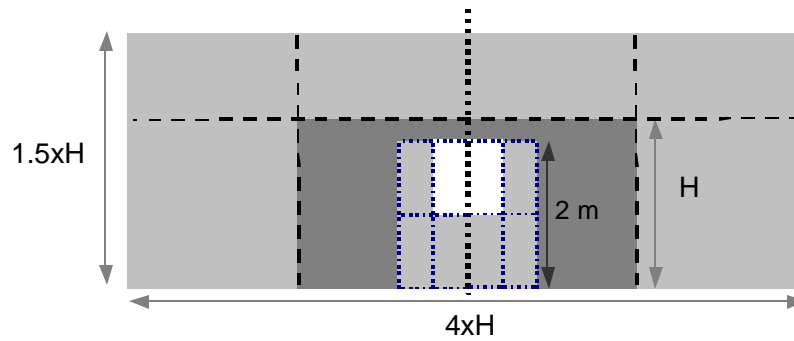


Figure 1.9

Cross-section view of the room cross-sections and apertures used in this study. Note in the center the four apertures used. The vertical dashed in the center signals the symmetry plane used when simulating only one half of the flow domain (see figure 1.6).

? Position of the inlet. In this case, two positions were considered, one in the center of the room and another where the perimeter of the inlet is adjacent to a lateral wall. In all cases, the outlet was similar to the inlet, and similarly located in the opposing surface (see the left side of Figure 1.2).

Four types of inlets/outlets were used, shown in Table 1.1, two windows and two doors:

? A window, with dimensions 1x1m, located at one-meter height (labeled: W).

? A wide window, with dimensions 2x1m, located at one meter height (label WW).

? A door, with dimensions 1x2m (labeled: D).

? A wide door, with dimensions 2x2m (labeled: WD).

Figure 1.9 shows a cross section view of the different rooms and apertures used in this study. Even when restricted to room geometries that conform to the limits described in this section, the variations in room dimensions, in conjunction with all possible inlet and outlet geometries, make testing the correlations a very extensive task. In order to make this task more manageable, the geometries and cases analyzed were restricted by choosing discrete values for each of the geometric parameters mentioned above. The different geometries and cases used in the simulations are presented in Tables 1.1-1.6.

Table 1.1. *Dimensions of the apertures used to develop and test the correlations.*

| Aperture | Area (A_{IN} , m ²) | Perimeter (P , m) | U_{IN} (average, m/s, $F_{IN}=1\text{m}^3/\text{s}$) |
|------------------|------------------------------------|----------------------|---|
| Window (W) | 1 | 4 | 1 |
| Door (D) | 2 | 5 | 0.5 |
| Wide window (WW) | 2 | 6 | 0.5 |
| Wide door (WD) | 4 | 6 | 0.25 |

Table 1.2. *Dimensions of the rooms used to develop and test the correlations.*

| Case | 121 | 122 | 123 | 221 | 222 | 223 | 141 | 142 | 143 | 144 | 146 | 241 | 242 | 243 | 244 | 246 |
|-------------------------|------|------|------|------|------|------|------|------|------|------|------|------|------|------|------|------|
| H (m) | 2.25 | 2.25 | 2.25 | 3.4 | 3.4 | 3.4 | 2.25 | 2.25 | 2.25 | 2.25 | 2.25 | 3.4 | 3.4 | 3.4 | 3.4 | 3.4 |
| W (m) | 4.5 | 4.5 | 4.5 | 4.5 | 4.5 | 4.5 | 9 | 9 | 9 | 9 | 9 | 9 | 9 | 9 | 9 | 9 |
| L (m) | 2.25 | 4.5 | 6.75 | 2.25 | 4.5 | 6.75 | 2.25 | 4.5 | 6.75 | 9 | 13.5 | 2.25 | 4.5 | 6.75 | 9 | 13.5 |
| V.(m ³) | 23 | 46 | 68 | 34 | 69 | 103 | 46 | 91 | 137 | 182 | 273 | 69 | 138 | 207 | 275 | 413 |
| A_R (m ²) | 10.1 | 10.1 | 10.1 | 15.3 | 15.3 | 15.3 | 20.3 | 20.3 | 20.3 | 20.3 | 20.3 | 30.6 | 30.6 | 30.6 | 30.6 | 30.6 |

All the room geometries used to develop the correlations have one inlet and one outlet, with the same dimensions, placed in the center of the inlet and outlet surfaces (the door is placed in the center on the horizontal and adjacent to the floor on the vertical). The horizontal symmetry of all the cases allowed for the simulation of only one half of the flow domain, simplifying the simulations. In addition, simulations of one half of the symmetrical room were used to represent the flows in rooms where the inlet is close to a lateral surface, under the verified assumption (simulations performed by the author, not presented here) that the effect of the missing lateral surface on the flow characteristics of interest is smaller than 10%, therefore acceptable in the present context (we seek first order accuracy). With this purpose, some of the wide window and wide door cases are used to simulate window and door cases with the inlet adjacent to a lateral surface.

The cases simulated were labeled using one letter for the aperture type (W, WW, D and WD), and three numbers for the height width and length. The numbers used for the room dimensions are scaled with room height. The number two is used to label the height in the cases with 3.40 m height for simplicity. All cases were simulated using a one cubic meter per second volumetric flow rate after initial exploratory simulations revealed that scaling coefficients do not depend on the airflow rate as long as turbulent dominated flow is insured. For all the inlets a turbulence dominated airflow pattern can be obtained for flow rates of $0.5 \text{ m}^3/\text{s}$ and even lower in the case of the windows and standard door (see Table 1.1). It is important to use similar flow rates for all rooms and aperture types in order to allow for straightforward comparisons between the recirculation flows that result from different geometries.

Chapter two of this thesis presents the extension of the model to heat transfer in CV rooms discussing in detail the interaction between natural and forced convection. For now, an upper limit for the temperature variation between inlet and outlet is imposed, which places an indirect upper limit in the magnitude of the buoyancy driven flow. Taking into account the maximum height of the rooms used (3.4m), and comparing buoyancy driven mass flow rates for plumes and natural convection boundary layers with the recirculation mass flow rates obtained from CFD, it is possible to conclude that forced convection will dominate the flow pattern whenever the temperature variation between inlet and outlet is smaller than $\approx 2^\circ\text{C}$.

The model may still be applicable to rooms outside these limits as long as all of the following conditions are verified:

- ? Most of the jet path in the room is in the shear layer region (the jet does not enter the transition region before two thirds of the room length).
- ? Buoyancy sources, such as vertical heated or cooled room surfaces and plumes, do not dominate the flow.
- ? The flow is turbulent in the jet region and in the boundary layers close to the room surfaces in the recirculation regions.
- ? In rooms with an horizontal inlet close to the floor or ceiling whenever buoyancy forces do not dominate the recirculation flow. In this case significant buoyancy effects can occur when a cold jet drops from a high inlet and accelerates, increasing the recirculation flow).

1.5 - Results

The constants C_n on the right hand side of the correlation expressions introduced in section 3 were determined using linear regression. Since zero flow or inlet velocity will lead to zero recirculation velocities and flow rates the linear regression lines always pass through the origin. We proceed to analyze the model results that will be plotted against the post-processed CFD results for the correlated quantities. Table 3 shows the designations of the 46 cases used to develop the main correlations.

Figure 1.10, shows the maximum momentum flux in the recirculation region as a function of the right hand side of (1.4) and (1.6). Analysis of this figure shows that the shear layer based correlation leads to smaller prediction errors. This qualitative result is confirmed by the correlation constant, R^2 , significantly higher in the shear layer case ($R^2=0.75$ versus $R^2=0.44$, see Table 1.6). Clearly for the set of cases used in this study, shear layer principles are more effective than inlet momentum flux to scale the momentum flux in the recirculation flow.

The momentum flux in the recirculation occurs through a fraction of the cross section area (where $U_x < 0$), with the remainder occupied by the jet flow. In table 1.3, the row labeled A_F shows the fraction of the room cross-section area occupied by the jet in the point of maximum mass flow rate. Although there is noticeable variation in the values, minimum 0.47, maximum 0.71, most values are close to 0.5. In view of these results, and within the first order accuracy goal, we conclude that the area occupied by the recirculation flow can be scaled using A_R (any constant multiplying value, such as one

half, will be automatically included in the correlation process). The adequacy of this and all other approximations will be visible in the adequacy of the correlations presented.

Table 1.3. *Subset of cases used to develop the main correlations ($1 < C_L < 4$). A_F is the minimum room cross-section fraction occupied by the recirculation flow ($U_x < 0$).*

| Case | D122 | D123 | D142 | D143 | D144 | D146 | D222 | D223 | D242 | D243 |
|-------|------|------|------|------|------|------|------|------|------|------|
| C_L | 2.6 | 3.9 | 1.1 | 1.7 | 2.3 | 3.4 | 2.6 | 3.9 | 1.1 | 1.7 |
| A_F | 0.57 | 0.55 | 0.54 | 0.55 | 0.54 | 0.53 | 0.64 | 0.71 | 0.53 | 0.53 |

| Case | D244 | D246 | W121 | W122 | W123 | W142 | W143 | W144 | W146 | W221 |
|-------|------|------|------|------|------|------|------|------|------|------|
| C_L | 2.3 | 3.4 | 1.3 | 2.6 | 3.9 | 1.1 | 1.7 | 2.3 | 3.4 | 1.3 |
| A_F | 0.52 | 0.53 | 0.52 | 0.53 | 0.56 | 0.52 | 0.52 | 0.52 | 0.51 | 0.5 |

| Case | W222 | W223 | W242 | W243 | W246 | WD122 | WD142 | WD143 | WD144 | WD146 |
|-------|------|------|------|------|------|-------|-------|-------|-------|-------|
| C_L | 2.6 | 3.9 | 1.1 | 1.7 | 3.4 | 3.6 | 1.3 | 1.9 | 2.6 | 3.9 |
| A_F | 0.49 | 0.5 | 0.49 | 0.5 | 0.49 | 0.62 | 0.57 | 0.55 | 0.55 | 0.55 |

| | WD24 | WW12 | WW1 | WW14 | WW14 | WW14 | WW24 | WW24 | WW24 | WW24 |
|-------|------|------|------|------|------|------|------|------|------|------|
| Case | 6 | 2 | 42 | 3 | 4 | 6 | 2 | 3 | 4 | 6 |
| C_L | 3.9 | 3.6 | 1.3 | 1.9 | 2.6 | 3.9 | 1.3 | 1.9 | 2.6 | 3.9 |
| A_F | 0.51 | 0.69 | 0.55 | 0.54 | 0.54 | 0.53 | 0.54 | 0.53 | 0.52 | 0.51 |

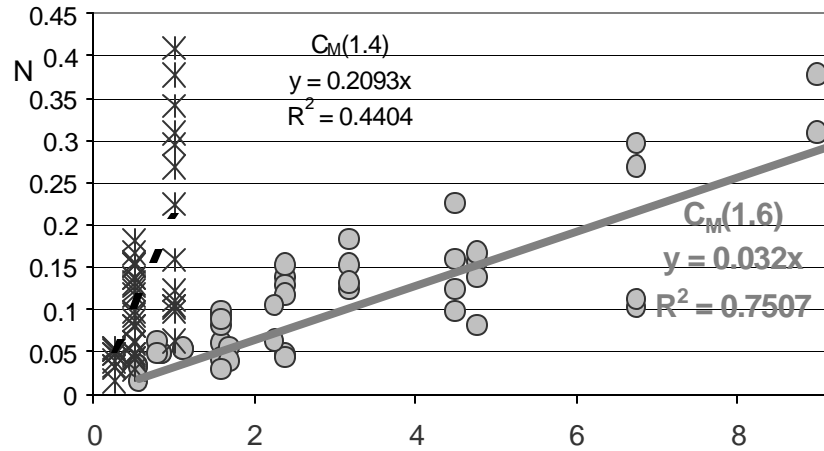


Figure 1.10

Maximum momentum flux in the recirculation region.

Dashed line and stars: momentum based correlation. Gray line and dots: shear layer based correlation. In the horizontal axis the non-dimensional factor: A_{IN}/A_R (momentum based correlation, expression 1.4), $A_{IN}^{1/2} \cdot L/A_R$ (shear layer correlation, expression 1.6).

Tables 1.4 and 1.5 show a set of 20 additional cases where the flow has a different balance, although still characterized by two distinct regions. The common characteristic of the 16 cases, shown in table 1.4, is a large length to width ratio. In these cases, the flow eventually attaches to the lateral surfaces in the region close to the outlet in the last third of the room length. The flow starts with recirculations but towards the outlet becomes similar to case C (see figure 1.4), where the momentum flux in the room scales with inlet momentum flux.

Further, the maxima of the recirculation flow parameters (momentum, mass and velocity) occur in the first half of the room (as opposed to two thirds or further along the

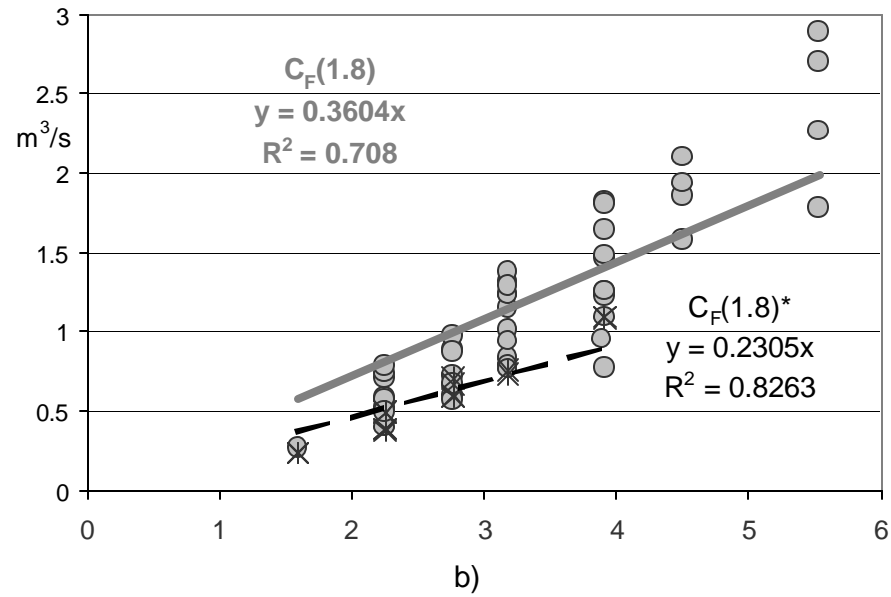
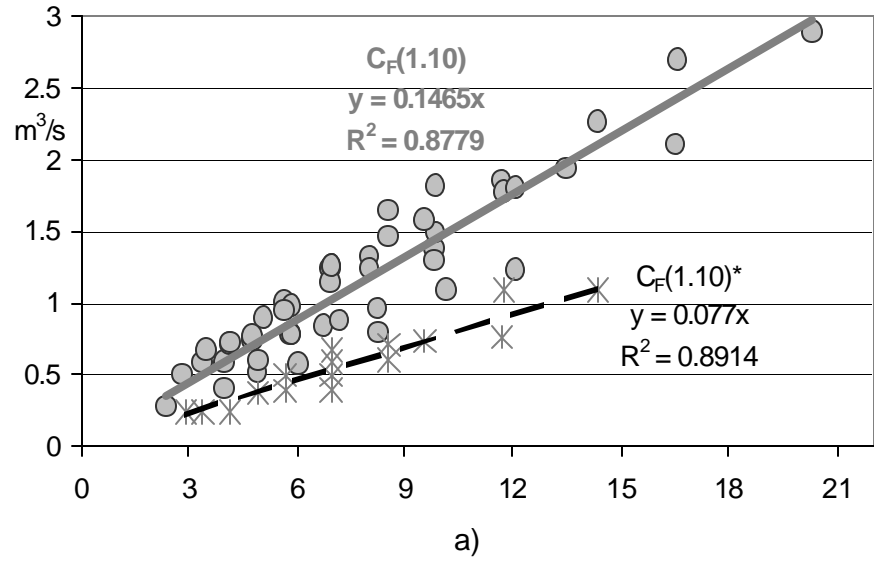


Figure 1.11

Maximum flow rate in the recirculation region.

a) flow rate in the recirculation using expression 1.10, based on shear layer scaling, for the cases in table 1.3 (gray dots) and in table 1.4 (stars).

b) flow rate in the recirculation using expression 1.8, based on inflow momentum flux, for the cases in table 1.3 (gray dots) and in table 1.4 (stars).

In both charts, the horizontal axis is the value of the non-dimensional factor on the right hand side of each correlation expression (see right hand side of expression 1.8 and 1.10).

room, as in the cases in table 1.3). Due to their combined nature, partially type R ,

partially type C, these cases have different slopes in the momentum flux correlations (see correlations labeled (*) in table 1.6). Further, due to the transition between recirculation and attached flow that occurs in these cases, the flow pattern is expected to be particularly sensitive to furniture and buoyancy effects that are always present in real rooms (see se). In addition to these transitional cases, table 1.5 shows a further set of 4 cases where the flow balance is also different from the main set shown in Table 1.3. In these cases the width to length ratio is large, making the recirculation behave differently, with an even smaller momentum flux (due to the small room length) occurring in a relatively large cross section area.

Table 1.4. *Subset of cases used to develop the correlations for long rooms ($C_L > 4$).*

| Case | W124 | W126 | W224 | W226 | WW123 | WW124 | WW126 | WW224 |
|-------|------|------|------|------|-------|-------|-------|-------|
| C_L | 5.1 | 7.7 | 5.1 | 7.7 | 5.4 | 7.2 | 10.8 | 7.2 |
| A_F | 0.47 | 0.47 | 0.48 | 0.49 | 0.64 | 0.62 | 0.63 | 0.58 |

| Case | WW226 | D124 | D126 | D224 | D226 | WD123 | WD124 | WD126 |
|-------|-------|------|------|------|------|-------|-------|-------|
| C_L | 10.8 | 5.1 | 7.7 | 5.1 | 7.7 | 5.4 | 7.2 | 10.8 |
| A_F | 0.57 | 0.52 | 0.53 | 0.68 | 0.63 | 0.6 | 0.6 | 0.6 |

Table 1.5. *Subset of cases with C_L smaller than two thirds.*

| Case | D141 | W141 | WD141 | W241 |
|-------|------|------|-------|------|
| C_L | 0.6 | 0.6 | 0.6 | 0.6 |
| A_F | 0.54 | 0.53 | 0.55 | 0.47 |

Clearly, it is essential to develop a simple criterion to distinguish “standard” CV recirculation cases from these transitional cases. The criterion that most successfully achieves this distinction is:

$$C_L = \frac{2L}{W - W_{IN}}, \quad C_L \leq 4 \quad (1.14)$$

The values of C_L are shown in tables 1.3-1.5 for each case (lines labeled C_L). Note that C_L is below the transition value of 4, for rooms with a length to width ratio below 2 (considering $W_{IN} < W$). The ratio on the right hand side of (1.14) scales the growth of the shear layer that develops at the limit of the main jet flow (proportional to L) with the available room width for shear layer expansion (on the denominator). The use of the width as the length scale for available space for shear layer expansion reflects the low height to width ratio found in most rooms and also in the ones simulated in this study. This low ratio leads to jet attachment to part of the floor and ceiling surfaces that are directly in front of the aperture, limiting the vertical expansion of the shear layer. In the case of a room with height comparable to the width it is more appropriate to use a scaling principle based on characteristic diameters of the room cross section and inlet aperture areas.

One important fact displayed by (1.14) is that rooms where the inlet is placed close to one of the lateral surfaces tend to have more space for shear layer growth. This leads to higher recirculation mass flow rates and velocities. In rooms with the inlet placed close to a lateral surface, the whole room width is available for shear layer expansion, therefore the factor of two in the denominator must be dropped in expression 1.14. When the model is used to predict CV flows where the inlet is close to the floor or ceiling,

generating vertical recirculations, the room and inflow aperture heights, H and H_{IN} , should replace W and W_{IN} in (1.14).

When $C_L > 4$, drag in the room surfaces and attachment of the jet to the lateral surfaces leads to decreased momentum flux in the recirculation, for this reason separate correlations are developed for these cases. In the following plots these cases are represented by stars and have a dashed correlation line. As expected, this line has a smaller slope than the cases where $C_L < 4$. The cases in table 5 ($C_L < 2/3$) were not used to develop the main correlations but are reasonably modeled by these correlations. The correlations are expected to be very imprecise for cases with $C_L < 1/3$ and $C_L > 11$. In the cases with small C_L the model is not applicable because the aspect ratio of the room is too extreme (large cross section to room length ratio) and the dominance of the shear layer momentum transfer in recirculation flow may not occur. The same reasoning applies to the other extreme case, large C_L , in this case due to the large room length.

For the more extreme cases, where $C_L > 11$, the best way to model the flow is to apply the results for case C, ignoring the recirculations.

The upper limit imposed on C_L already indicates that the model should not be applied when the length of expansion for the shear layer is very large. The correct way to scale jet development, in order to prevent the use of the model for rooms where the jet reaches the developed stage (when the maximum velocity drops with x) is using L^* (see (1.2)). In addition to this length limitation, a limit should be imposed on A^* since it can be expected that for very large values of this parameter the momentum flux in the return flow becomes infinitesimal and therefore the present analysis is not applicable. After analyzing the cases in the CFD library as well as few exploratory runs for very large

rooms it was decided to use the following criterion as the upper limit of application of the model:

$$\sqrt{L^* A^*} < 20 \quad (1.15)$$

This limit ensures that one of the conditions to apply the model is present, the other being the need to have a flow that is dominated by forced convection. Expression 1.15 places an upper limit on room dimensions, scaled by inflow aperture length scale. One clear reason why this limit is needed is the fact that dissipation in the recirculation region is neglected. As the room becomes larger dissipation effects increase, while the energy source remains constant (the inflow jet), an upper limit is needed. As could be expected, (1.15) effectively places an upper limit on F_R/F_{IN} , U_R/U_{IN} and U_S/U_{IN} .

Table 1.6 shows the slopes of the lines that minimize the error for the correlations described above (the correlation constants, C). From the results shown in this table we conclude that the correlations proposed achieve first order accuracy. The correlations labeled with a (*) in the table refer to the cases with $C_L > 4$ (long rooms, shown in Table 1.4). As expected the slopes in these correlations are smaller than for the standard correlations (cases in Table 1.3), as a consequence of the higher dissipation that occurs in long rooms.

Table 1.6. Results of the correlations. The equation number is shown in parenthesis. The columns signaled with (*) are for $C_L > 4$. All lines pass by the axis origin. The line labeled Max/Min shows the ratio between minimum and maximum values, obtained from the library of CFD cases used to develop the correlation.

| Correlation | $C_M(6)$ | $C_M(4)$ | $C_R(9)$ | $C_R(9)^*$ | $C_R(7)$ | $C_R(7)^*$ | $C_F(10)$ | $C_F(10)^*$ |
|-------------------------|----------|----------|----------|------------|----------|------------|-----------|-------------|
| Best Fit Slope | 0.032 | 0.209 | 0.298 | 0.162 | 0.68 | 0.487 | 0.147 | 0.077 |
| Linear Regression R^2 | 0.75 | 0.44 | 0.67 | 0.28 | 0.42 | 0.55 | 0.88 | 0.89 |
| Max/Min | 27.5 | 27.5 | 4 | 3.7 | 4 | 3.7 | 10.6 | 4.6 |
| Average Error (%) | 30 | 60 | 16 | 19 | 19 | 60 | 17 | 17 |
| Maximum Error (%) | 111 | 267 | 38 | 64 | 72 | 149 | 55 | 51 |

| Correlation | $C_F(8)$ | $C_F(8)^*$ | $C_J(11)$ | $C_J(11)^*$ | $C_S(12)$ | $C_S(12)^*$ | $C_C(13)$ | $C_C(13)^*$ |
|-------------------------|----------|------------|-----------|-------------|-----------|-------------|-----------|-------------|
| Best Fit Slope | 0.36 | 0.231 | 1.56 | 1.23 | 0.066 | 0.044 | 0.115 | 0.082 |
| Linear Regression R^2 | 0.71 | 0.83 | 0.96 | 0.83 | 0.63 | 0.6 | 0.64 | 0.59 |
| Max/Min | 10.6 | 4.6 | 3.6 | 2.5 | 3.8 | 2.3 | 2.9 | 1.9 |
| Average Error (%) | 28 | 92 | 5 | 9 | 14 | 14 | 11 | 11 |
| Maximum Error (%) | 110 | 163 | 13 | 26 | 55 | 31 | 43 | 24 |

Figure 1.11 shows the correlation lines for the flow rate in the recirculation region for the shear layer based and momentum flux based correlation principles ($C_F(1.10)$ and $C_F(1.8)$ respectively in Table 1.6). As in figure 1.10, analysis reveals better results from the shear layer based correlations (Figure 1.11 a).

Figure 1.12-1.13 shows the characteristic velocity in the recirculation region, again revealing the clear advantages of a shear layer (1.12 a) versus an inflow momentum scaling (1.12 b). Figure 1.14 shows the correlation lines for the average velocity in the main jet region. Finally, figure 1.15 shows the correlations for the near room surface velocities, using a combination of momentum and shear layer scaling principles. As expected, in all these figures the lines for the correlations for the cases with $C_L > 4$ have smaller slopes due to increased dissipation effects.

The four correlations adopted in the model (shown in the Table 1.6) are:

1. Average recirculating flow velocity in the room cross section with maximum flow rate ($1/3 < C_L < 11$):

$$U_R = C_R \sqrt{\frac{L}{A_R \cdot A_{IN}^{3/2}}} F_{IN} , \quad C_R = \begin{cases} 0.298 , & 1/3 \leq C_L \leq 4 \\ 0.162 , & 4 < C_L \leq 11 \end{cases} \quad (1.16)$$

2. Average volumetric velocity in the main jet region ($1/3 < C_L < 11$):

$$U_J = 1.56 \frac{F_{IN}}{\sqrt{A_R \cdot A_{IN}}} , \quad 1/3 \leq C_L \leq 11 \quad (1.17)$$

3. Volumetric flow rate of the return flow ($1/3 < C_L < 11$):

$$F_R = C_F \sqrt{\frac{L A_R}{A_{IN}^{3/2}}} \cdot F_{IN} , \quad C_F = \begin{cases} 0.147 , & 1/3 \leq C_L \leq 4 \\ 0.077 , & 4 < C_L \leq 11 \end{cases} \quad (1.18)$$

4. Average velocity near the room surfaces ($1/3 < C_L < 11$):

$$U_S = C_S \sqrt{\frac{121 \sqrt{A_{IN}} + L}{A_{IN}^{3/2} A_R}} \cdot F_{IN} , \quad C_S = \begin{cases} 0.066 , & 1/3 \leq C_L \leq 4 \\ 0.044 , & 4 < C_L \leq 11 \end{cases} \quad (1.19)$$

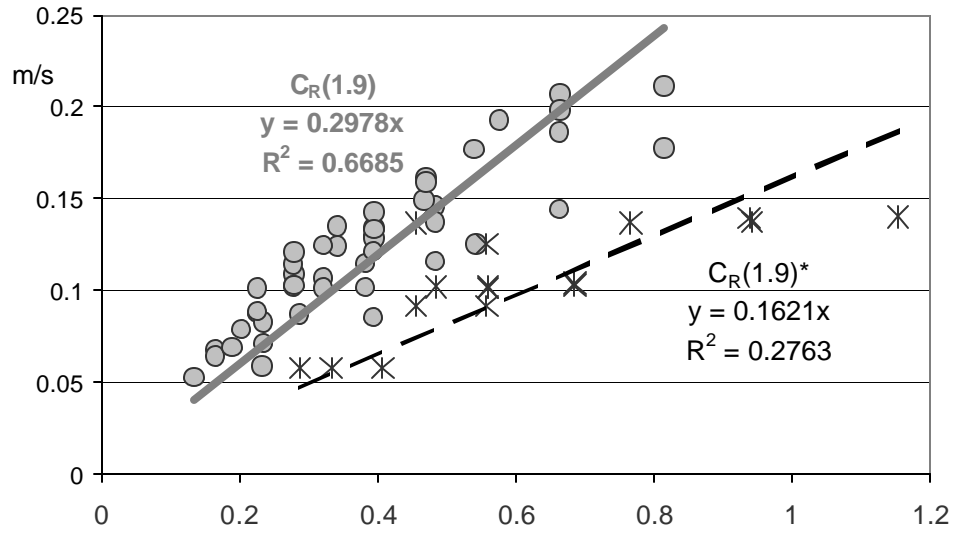
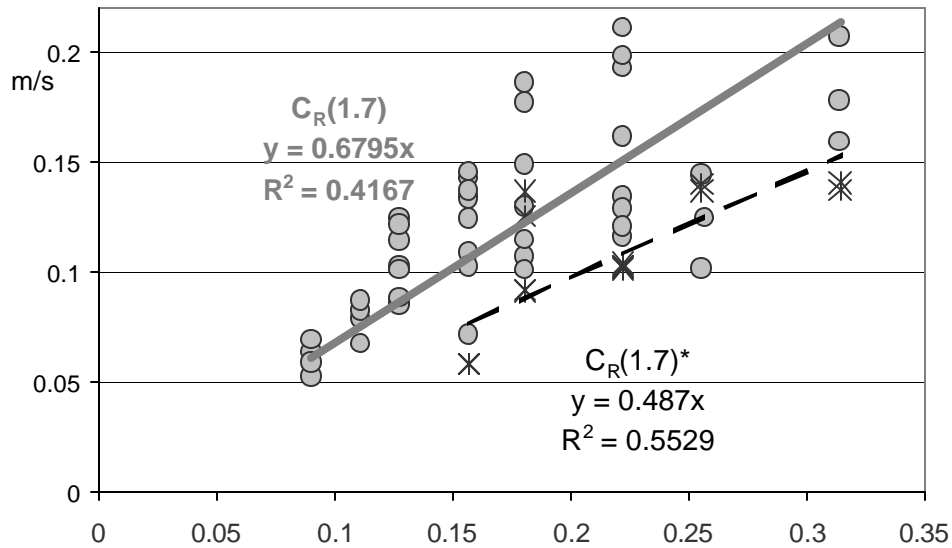


Figure 1.12.

Average velocity in the recirculation region.

Average velocity in the recirculation using expression 1.9, based on shear layer scaling, for the cases in table 3 (gray dots) and in table 4 (stars).



b)

Figure 1.13.

Average velocity in the recirculation region.

Average velocity in the recirculation using expression 1.7, based on inflow momentum flux, for the cases in table 3 (gray dots) and in table 4 (stars).

In both charts, the horizontal axis is the value of the non-dimensional factor on the right hand side of each correlation expression (see right hand side of expression 1.7 and 1.9).

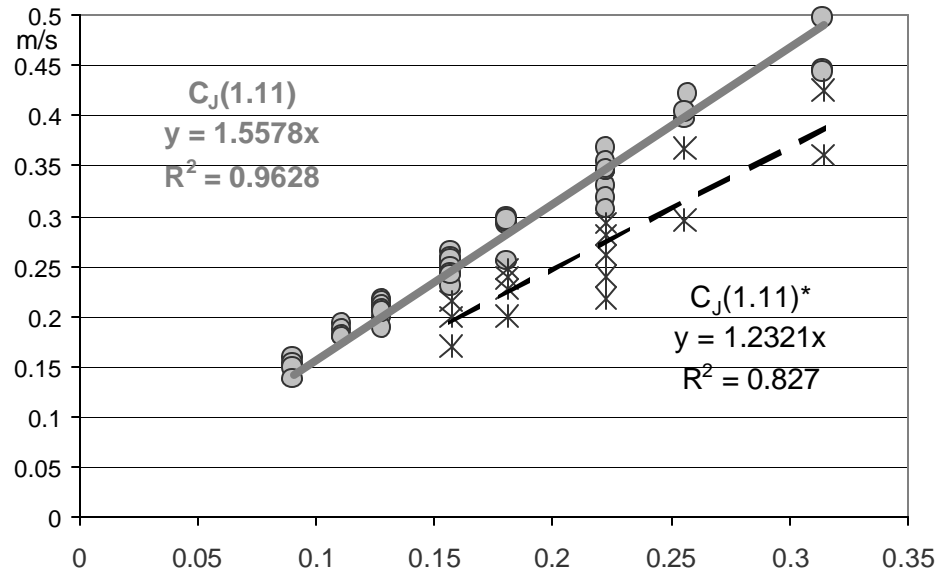


Figure 1.14

Average velocity in the main jet region.

The horizontal axis is the value of the non-dimensional factor on the right hand side of each correlation expression (see right hand side of expression 1.11).

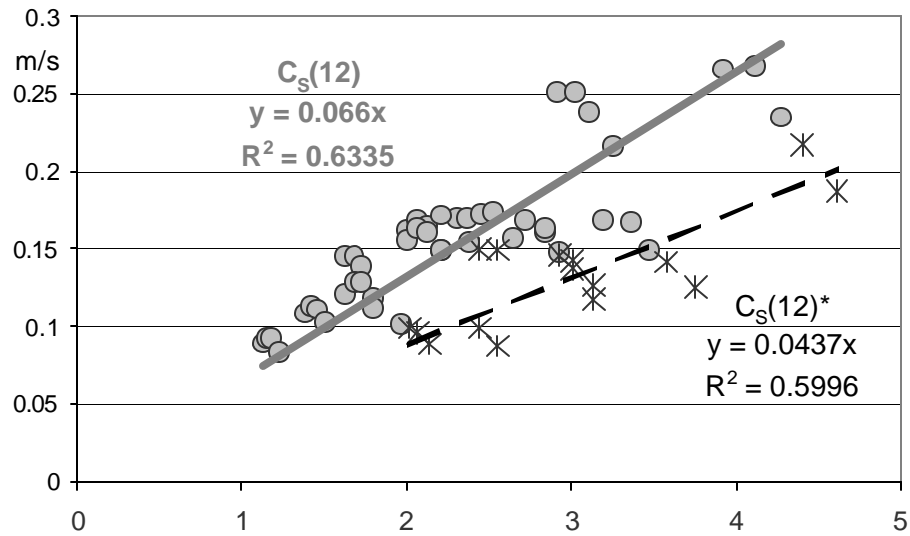


Figure 1.15

Average velocity near the room surfaces.

The horizontal axis is the value of the non-dimensional factor on the right hand side of each correlation expression (see right hand side of expression 1.11).

1.6 - Analysis

From the results in table 6, we note that the most successful correlation is for average velocity in the jet region, achieving predictions with negligible error for a set of cases with a relative variation of 3.6 (line labeled: Max/Min in Table 1.6). It is interesting to see how accurate the shear layer based correlation (Equation 6) is when estimating momentum flux in the cases shown in Table 1.3. This correlation, labeled $C_M(1.6)$ in Table 1.6, can predict the momentum flux with an average error of 30% for a set of CFD post processed values with a maximum variation of a factor of 27.5 in magnitude.

The relative errors of the predictions do not depend on the flow rate. Attempting to predict flow quantities for variable flow rates linearly increases the prediction intervals shown in the fourth line of Table 1.6, making the final results of the model more impressive as the range of predicted values linearly increases with the range of flow rate variations.

1.7 - Applications

The application of the model to design cases requires consideration of a set of particular problems that are discussed in the next paragraphs. The section starts by looking at effects of furniture on the CV flow and then discusses asymmetric rooms, evaluation of surface heat transfer coefficients and applications of the model to estimation of thermal comfort and control of indoor air velocities.

1.7.1 - Effects of furniture

Most rooms contain furniture, therefore, it is essential to estimate the effects of furniture on the flow quantities correlated by (1.16)-(1.19). When trying to model the complex flows that can occur in rooms with furniture there is a need to increase the complexity of the model while expecting lower accuracy in the predictions. Still, the usefulness of quantitative results for this problem is clear, since CFD modeling of rooms with furniture is difficult and not currently feasible in a typical design scenario. In addition, this analysis will be

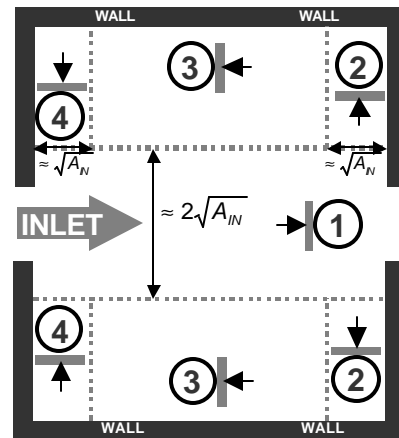


Figure 1.16

Top view of the four sub regions used to model furniture effects. Note the gray bars with black arrows showing the correct orientation for evaluation of furniture cross section area in each zone.

useful if it can reveal general effects and controlling geometric effects that determine furniture effects on the airflow.

The analysis will be restricted to rooms where furniture, occupants, and airflow inlet/outlet are all at less than 2 m height, the most common case. Also, we will consider only simple furniture elements with approximately flat surfaces using bulk geometric dimensions. We will seek a single multiplying correction factor to correct the predictions for the different quantities.

Sections 1.4 and 1.5 present 60 distinct room geometries. The combination of these geometries with, for example, 10 furniture configurations creates an unmanageable number of test cases. In order to keep this number manageable the analysis will focus on cases *W143*, *W243* and *D143* and only a few furniture elements and configurations. Many additional exploratory runs were performed and will not be discussed here due to lack of space. Cases *W143* and *W243* were chosen because they offer enough space to dispose the furniture in the different room zones. Case *D143* is used to test for dependence of the results on inlet geometry.

We begin the analysis by discussing rooms where the effect of furniture elements leads to a clear reduction in overall room dimensions, such as when shelves fully cover one particular wall. These cases can be handled in a straightforward way by reducing the room dimensions, ignoring any effects due to drag in the furniture surfaces, as in section

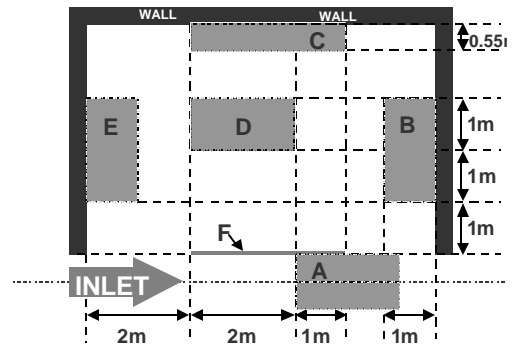


Figure 1.17

Top view of the positions of the furniture elements used to test the correlations.

The dimensions of the objects introduced in the different positions are shown in table 7 and labeled as shown in the figure.

3. Using (1.15)-(1.18) in these cases requires either a corrected room cross section area, given by the room area minus the shelf cross section area (for shelves in the lateral surfaces), or, in the case of the end and back walls, a corrected room length, obtained by subtracting the total depth of the furniture elements along the CV direction from the total room length.

We proceed by discussing rooms with flows of type C. Unsurprisingly, correcting for furniture effects in these flows is straightforward: the characteristic CV velocity can be estimated by correcting the available area for airflow. This should be done by subtracting the furniture cross-section area (A_F) at any given location along the room from the room cross section area. The characteristic velocity is then obtained by dividing the flow rate by this corrected area. Because we consider occupied zones and furniture elements that only reach two meters in height the room cross section area is evaluated only up to this height: $A_R=2.W$. The velocity scale for flows of type C is then given by:

$$U_J = \frac{F_{IN}}{2.W - A_F} \quad (1.20)$$

Modeling the effects of furniture in rooms with flows of type R or CR is more difficult. In order to make the analysis clearer we introduce a coefficient, E_F , that multiplies the right hand side of expressions (1.16)-(1.19) in order to model the effects of furniture. Figure 1.17 shows a set of regions in a room, with flow of type R, defined in such a way that placing furniture elements anywhere within a given zone leads to similar effects on the quantities predicted in (1.16)-(1.19). The definition of these zones was the result of a set of CFD simulations guided by the insights on the flow behavior obtained above. The criterion for numbering the zones was: decreasing effects of furniture on the flow. The

zones are distinguished by their location in the room, characteristic length scale of the flow in the zone and, above all, particular effects on the flow pattern. The gray bars with pointing arrows in the figure show the direction that should be used when estimating the furniture obstruction area (A_F) in the different zones.

As discussed in section 1.3, the characteristic length scales of the flow in the different zones are (see figure 1.16):

$A_{IN}^{1/2}$ in zones 1, 2, and 4,

A_R in zone 3

Whenever furniture elements are isolated in the room, the most common case, shown in figure 1.17, their interference with the CV flow pattern can be accessed by comparing the furniture length scale perpendicular to the cross ventilation direction in the zone with the applicable characteristic length scale for the flow. If the characteristic length of the furniture is smaller than the flow length scale, the effects of furniture are small, less than 10%, and will be neglected. CFD simulations placing several furniture elements in the different zones of the room for cases *W143*, *W243* and *D143*, revealed that furniture effects can be ignored whenever the furniture cross section length scale ($A_F^{1/2}$) is such that:

$$\text{Zone 1,2,4: } \frac{\sqrt{A_F}}{\sqrt{A_{IN}}} \leq \frac{1}{2} \quad \text{Zone 3: } \frac{\sqrt{A_F}}{\sqrt{A_R}} \leq \frac{1}{4} \quad (1.21)$$

These relations translate the small effects found when introducing objects resembling tables and chairs with no significant cross section in the simulations. In the case of zone

three it is even possible to introduce objects with significant obstruction areas, such as a desk with lateral panels, without significantly affecting the flow pattern. The next paragraphs discuss in detail the effects of furniture elements with areas that do not meet criterion (1.21) and present simple corrections for the predictions (1.16) - (1.19).

Figure 1.17 shows a top view of the furniture locations used to test and develop the correlations presented below, while table 7 shows the dimensions of the furniture elements used. Inserting objects in zone one can directly affect the development of the CV flow. In particular, any furniture elements whose cross section area does not meet criterion (1.21) for zone 1 can stop the cross ventilation flow. For this reason the present model is not applicable when furniture with area such that: $\sqrt{A_F} \geq 0.5 \sqrt{A_{IN}}$ is placed before halfway along the room. In these situations the CV flow pattern is destroyed when the main jet is deflected by the furniture and the best way to model the flow is to approximate it as mixed flow (the accuracy of the predictions in this case is low). Whenever the furniture is placed beyond halfway along the room the flow pattern still exhibits clear recirculating flow regions, and the impact of the furniture can be accounted for by replacing the room length by the length along the room where the furniture is placed:

$$E_F = \sqrt{\frac{L - L_F}{L}} \quad (1.22)$$

The correction factor, E_F , should be applied to all correlation formulas (1.16-1.19).

Whenever a furniture element obstructs part of the interface between zones 1 and 3 the recirculation flow can be significantly reduced, as a result of the obstruction and reduction of the entrainment surface. These obstructions can occur when a vertical panel

is placed between the perimeter and the interface between zone 1 and 3. Note that placing a similar panel in the middle of zone 1, aligned with the inflow jet, as a negligible effect since it does not interfere with the entrainment process. As in the previous case, to obtain E_F , we consider obstructions up to the height of 2m and compare characteristic lengths of the obstructed and unobstructed entrainment lateral surface:

$$E_F = \frac{\sqrt{2 \cdot L - A_F}}{\sqrt{2 \cdot L}} \quad (1.23)$$

where, in this case, A_F is the surface area of the furniture panels along the surface that separates regions one and three. In this case the obstructions can begin before halfway along the room but, if the element containing the panel also has a significant cross section area (according to criterion 20), then E_F defined in (1.22) should be used instead of (1.23).

Table 1.7. *Dimensions of the furniture elements used to develop the correction factors E_F , shown in figure 1.17.*

| Object | A | B1 | B2 | C | D1 | D2 | E | F1 | F2 |
|--------|-----|----|----|------|----|----|---|----|----|
| L | 2 | 2 | 2 | 3 | 2 | 2 | 2 | 3 | 3 |
| W | 1.1 | 1 | 1 | 0.55 | 1 | 1 | 1 | 0 | 0 |
| H | 2 | 1 | 2 | 2 | 1 | 2 | 1 | 1 | 2 |

Table 1.8. Cases used to develop the correction factors E_F .

| CASE | Inlet | Room H | Zone 1 | Zone 2 | Zone 3 | Zone 4 |
|------|-------|--------|--------|--------|--------|--------|
| 1 | W | 2.25 | F1 | - | - | - |
| 2 | W | 2.25 | F2 | - | - | - |
| 3 | W | 2.25 | A | - | - | - |
| 4 | W | 2.25 | A | - | C+D2 | - |
| 5 | W | 2.25 | - | - | C+D1 | - |
| 6 | W | 2.25 | - | - | C+D2 | - |
| 7 | W | 2.25 | - | B1 | - | - |
| 8 | W | 2.25 | - | - | - | E |
| 9 | W | 2.25 | - | B1 | - | E |
| 10 | D | 2.25 | A | - | - | - |
| 11 | D | 2.25 | A | - | C+D2 | - |
| 12 | D | 2.25 | - | B1 | - | - |
| 13 | D | 2.25 | - | B2 | - | - |
| 14 | D | 2.25 | - | - | C+D1 | - |
| 15 | W | 3.40 | A | - | - | - |
| 16 | W | 3.40 | - | - | C+D1 | - |
| 17 | W | 3.40 | - | - | C+D2 | - |
| 18 | W | 3.40 | - | B1 | - | - |

Obstructions in zone 2 have strong consequences on the flow in the recirculation region, as a result of the acceleration that occurs as the detrained air from the main jet impacts the end wall. The results of the simulations with obstructions in this region showed that whenever: $\sqrt{A_F} \geq 0.5 \sqrt{A_{IN}}$ the flow in the recirculations is reduced by approximately one half. Therefore, in this case, (1.16), (1.18) and (1.19) should be multiplied by:

$$E_F \approx \frac{1}{2} \quad (1.24)$$

The characteristic jet velocity (1.17) is not affected by obstructions in this zone. Note that zone 2 does not start at the perimeter of the outlet (see figure 1.16). Furniture elements that are placed adjacent to the perimeter of the outlet and protrude into zone 2, fully occupying the CV room cross-section have different effects. In these cases the above-mentioned room dimension reduction correction should be used (expression 1.22). Note that, to achieve this straightforward reduction effect in the room length, furniture must be both in zones 1 and 2.

As shown in (1.20), the effects of furniture in zone 3 should be considered whenever $\sqrt{A_F} \geq 0.25 \sqrt{A_R}$, where A_F is the total cross sectional area of furniture in the recirculations (zone 2 in type R flows). In this zone, the correction factor is given by:

$$E_F = \frac{\sqrt{2 \cdot W - A_F}}{\sqrt{2 \cdot W}} \quad (1.25)$$

As in zone 2, the correction should only be applied to the recirculation quantities and not the jet region velocity (1.17). Note that, in (1.25), A_F should be the total furniture cross-section area in zone 3 of the room, measured in the direction shown in Fig. 1.16.

Finally, zone 4 proved to be the best location for minimizing furniture interference with the flow, as no significant effects were found. This is a consequence of the low flow velocities that occur close to the back wall as the air is re-entrained by the inflow jet, making any flow deflections induced by furniture in this zone lead to small energy dissipation.

Table 1.9 shows the values of E_F that should be used to handle furniture obstructions in the different zones (1.22-1.25). Whenever a room has obstructions in more than one zone the smallest of the several correction factors should be used when correcting (1.15)-(1.19) for the combined effect. As an example: when significant obstructions occur in zones 1 and 2, (1.17) should be corrected by using the E_F that results from the obstruction in zone 1. Table 1.10 shows the results of the corrections compared with the CFD simulations for the cases described in table 1.8. The results are presented in percentage, when compared with the reference cases that have no furniture. Note that these results only reflect the effects of E_F and not the combined effect of (1.14) - (1.18) and their corresponding E_F values. In addition to table 1.10, figures 1.18 and 1.19 show the results for the main jet and recirculation flow velocity. Analysis of these figures reveals that the corrections achieve only moderate accuracy, as expected in view of the complexity of the problem. Still, the correct trends are revealed in a simple and compact form.

Table 1.9. Corrections to use in the different zones when furniture areas exceeds criterion 20.

| Parameter | U_J | U_R | F_R | U_S |
|----------------|--------------------|---------------------------------|-------|-------|
| Zone 1 | $\sqrt{L - L_F/L}$ | | | |
| Zone 1 (panel) | 1 | $\sqrt{2.L - A_F} / \sqrt{2.L}$ | | |
| Zone 2 | 1 | 1/2 | | |
| Zone 3 | 1 | $\sqrt{2.W - A_F} / \sqrt{2.W}$ | | |
| Zone 4 | 1 | 1 | 1 | 1 |

Table 1.10. Comparison between CFD and the correction factors E_F .

| CASE | U_R | | F_R | | U_J | | U_S | |
|------|-------|-------|-------|-------|-------|-------|-------|-------|
| | CFD | E_F | CFD | E_F | CFD | E_F | CFD | E_F |
| 1 | 81 | 88 | 82 | 88 | 93 | 100 | 83 | 88 |
| 2 | 53 | 75 | 64 | 75 | 114 | 100 | 64 | 75 |
| 3 | 62 | 77 | 64 | 77 | 76 | 77 | 61 | 77 |
| 4 | 58 | 66 | 54 | 66 | 78 | 77 | 61 | 66 |
| 5 | 58 | 77 | 71 | 77 | 103 | 100 | 67 | 77 |
| 6 | 50 | 66 | 61 | 66 | 83 | 100 | 67 | 66 |
| 7 | 46 | 50 | 61 | 50 | 99 | 100 | 67 | 50 |
| 8 | 95 | 100 | 96 | 100 | 102 | 100 | 89 | 100 |
| 9 | 48 | 50 | 61 | 50 | 92 | 100 | 65 | 50 |
| 10 | 67 | 77 | 73 | 77 | 94 | 77 | 76 | 77 |
| 11 | 65 | 66 | 66 | 66 | 103 | 77 | 69 | 66 |
| 12 | 42 | 50 | 60 | 50 | 108 | 100 | 67 | 50 |
| 13 | 36 | 50 | 57 | 50 | 112 | 100 | 48 | 50 |
| 14 | 59 | 77 | 72 | 77 | 107 | 100 | 68 | 77 |
| 15 | 74 | 77 | 74 | 77 | 83 | 77 | 59 | 77 |
| 16 | 74 | 77 | 82 | 77 | 95 | 100 | 76 | 77 |
| 17 | 71 | 66 | 78 | 66 | 95 | 100 | 76 | 66 |
| 18 | 56 | 50 | 73 | 50 | 116 | 100 | 66 | 50 |

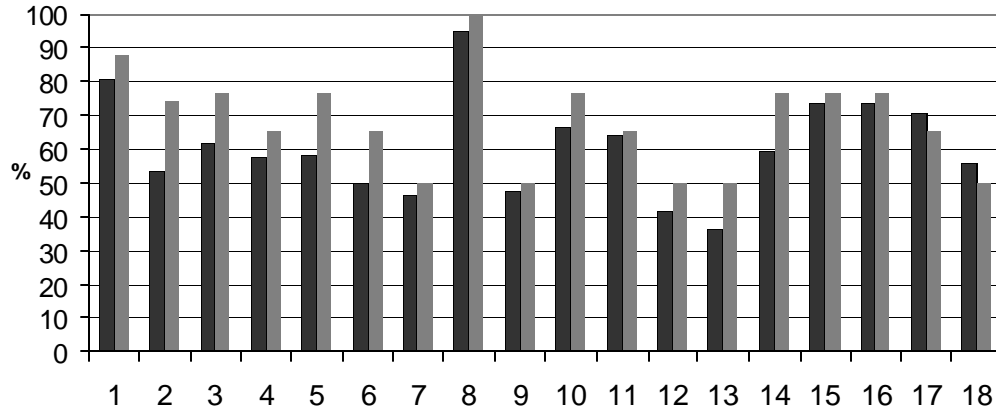


Figure 1.18

Comparison between the reductions obtained in the CFD simulations with the corrections E_F for the recirculation flow region velocity U_R . CFD results in black E_F correction factors in gray, the case descriptions are shown in table 1.8. The case number is shown in the horizontal axis.

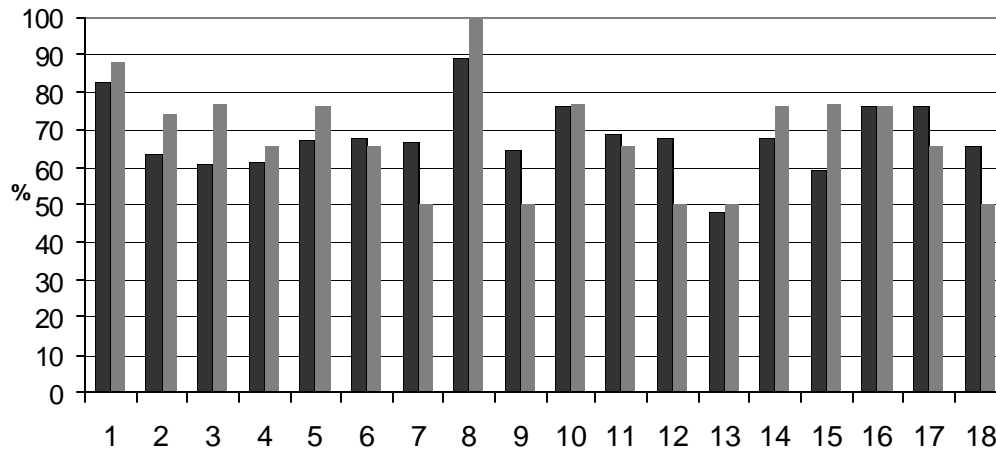


Figure 1.19

Comparison between the reductions obtained in the CFD simulations with the corrections E_F for the recirculation flow region velocity U_S . CFD results in black E_F correction fractions in gray, the case descriptions are shown in table 1.8. The case number is shown in the horizontal axis.

1.7.2 - Applications to asymmetric rooms

So far this chapter discussed symmetric rooms or rooms with part of the inlet and outlet perimeters adjacent to the same lateral surface. Asymmetric rooms are very common. Limited, exploratory, simulations for a few of the cases shown in Table 3, using asymmetric inlet/outlet configurations where the inlet does not face the outlet, indicate that the model and the correlations presented above are directly applicable to asymmetric rooms. It should be noted that in these rooms the smaller of the two recirculation regions tends to have a higher velocity and also reach values of $C_L > 4$ for smaller length to width ratios. It is not correct to apply the correlation principles to each of the two distinct recirculation zones independently, using different areas and room widths for each side. This leads the prediction of higher resultant flow rates (if the results from the two recirculations are added).

For design estimation in asymmetric rooms the best option is to use the standard correlations, estimating the flow rate on each side by multiplying the total flow rate by the fractional area of each side. This fractional area is calculated by multiplying the width of each side of the asymmetrical room (measured from the middle of the inlet) by the room height and dividing the resultant value by the total room cross-section area.

1.7.3 - Estimation of surface convection coefficients

The heat transfer coefficient in a turbulent forced convection boundary layer varies along the length of the boundary layer that forms close to the wall (with exponent -0.2) and with average velocity near the wall (with exponent 0.8) [Bejan, 1994]. The variation along the room length does not need to be modeled within the first order accuracy level of the CV model developed here. In this context it seems more adequate to consider a fixed length for the boundary layers, proportional to the room characteristic length (given by the cubic root of the room volume). In what regards the variation with the boundary layer driving velocity, it seems straightforward to use correlation 19 to scale to refine the

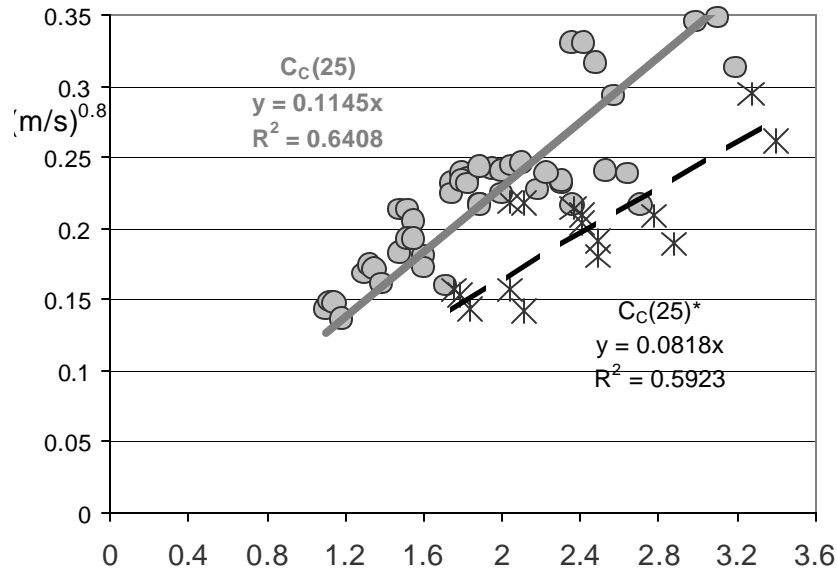


Figure 1.20

Results of the correlation for turbulent forced convection heat transfer.

Standard rooms ($C_L < 4$): gray line. Long rooms ($4 < C_L < 11$): dashed line. The units of the vertical axis are: $(\text{m/s})^{0.8}$ (the left hand side of expression 1.26). On the horizontal axis the values of the coefficient with exponent 0.4 on the right hand side of expression 1.26.

forced convection heat transfer coefficient predictions.

It would be possible to directly use correlation 1.19 with an exponent of 0.8 but given the importance of this application a specific correlation was developed, using the characteristic 0.8 exponent variation for forced convective heat transfer:

$$U_C^{0.8} = C_C \left(\frac{121 + L/\sqrt{A_{IN}}}{A_R/A_{IN}} \right)^{0.4} U_{IN}^{0.8}, \quad C_C = \begin{cases} 0.115, & 1/3 \leq C_L \leq 4 \\ 0.082, & 4 < C_L \leq 11 \end{cases} \quad (1.26)$$

Figure 1.20 shows the results of the correlation for the standard (gray line) and long rooms (dashed line). The accuracy of the model can be considered adequate, allowing for significant improvements in estimation of the heat transfer coefficients.

1.7.4 - Applications to thermal comfort evaluation – control of indoor air velocities

In addition to the correlation expressions presented above, when designing CV rooms, two additional ratios can be useful: the ratio between maximum velocity in the room and velocity in the main jet region and the ratio between velocity in the jet region and velocity in the recirculation.

The first ratio is important whenever a designer must limit the maximum air velocity at any point in the room. The maximum velocity always occurs directly in front and close to the inlet, in the vena contracta [Idelchik, 1986] region. The fractional contraction of the jet (coefficient C_D) is due to the flow through the inlet and can be obtained analytically for a

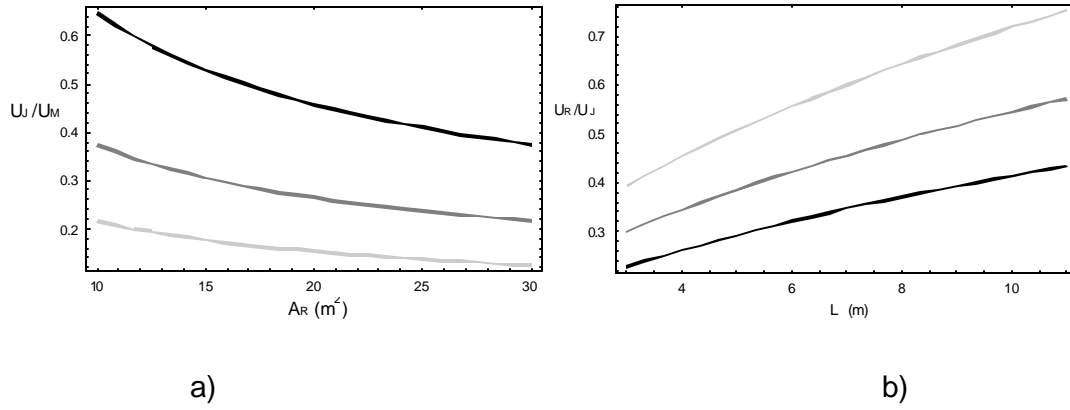


Figure 1.21

a) Ratio between the average velocity in the jet region and the maximum velocity in front of the inlet (expression 1.25). b) Ratio between the velocity in the recirculation and in the main jet region (expression 1.26). In both plots, three inlet sizes: 0.5 m^2 (light gray), 1.5 m^2 (medium gray) and 4 m^2 (black).

two dimensional flow (measurements in three-dimensional flows resulting in similar values [Ohba *et al.*, 2001]). The maximum velocity and the desired ratio are given by:

$$U_M = \frac{F_{IN}}{A_{IN} C_D}, C_D = 0.611$$

$$\frac{U_J}{U_M} = \frac{1.56 C_D}{\sqrt{A^*}} = 1.56 C_D \sqrt{\frac{A_{IN}}{A_R}}, \quad \frac{1}{3} \leq C_L \leq 11 \quad (1.27)$$

In some situations the maximum room airflow velocity is a limitation on the design and maximizing the second relation in (1.27) results in a ventilation system with higher velocities in the jet region of the room while remaining below the maximum allowed velocity (expression 1.27 is always smaller than one, as can be seen Figure 1.21-a).

The second relevant ratio is between velocities in the jet region and in the recirculation region, given by:

$$\frac{U_R}{U_J} = C_{RJ} \sqrt{L^*} = C_{RJ} \sqrt{\frac{L}{A_{IN}^{0.5}}}, \quad C_{RJ} = \begin{cases} 0.191, & \frac{1}{3} \leq C_L \leq 4 \\ 0.104, & 4 < C_L \leq 11 \end{cases} \quad (1.28)$$

This ratio is always smaller than one and independent of the room cross-section area. Figure 1.7-b shows plots of (1.28) for variable inlet areas and room lengths. Longer rooms maximize this ratio up to a limiting length since the flow pattern limitations translated in the criterion shown in (1.14) and (1.15) must be respected.

Figure 1.22-a shows the ratio between inlet flow rate and the recirculation flow rate predicted using (1.18) for cases with $C_L < 4$. It is interesting to note that for rooms with moderate to large volumes and inlets with areas below 2m^2 this ratio is bigger than one and can even reach three. These high recirculation flow rates are achieved with the above mentioned small momentum fluxes, when compared with the inlet flow, because the flow occurs in a large area, approximately one half of the room cross section (see table 1.3, line: A_F).

Figure 1.22-b illustrates possible advantages of using the model in conjunction with other models, in this case the Fanger thermal comfort model [ISO, 1993]. This thermal comfort model is commonly used to simulate building occupant thermal sensation. The

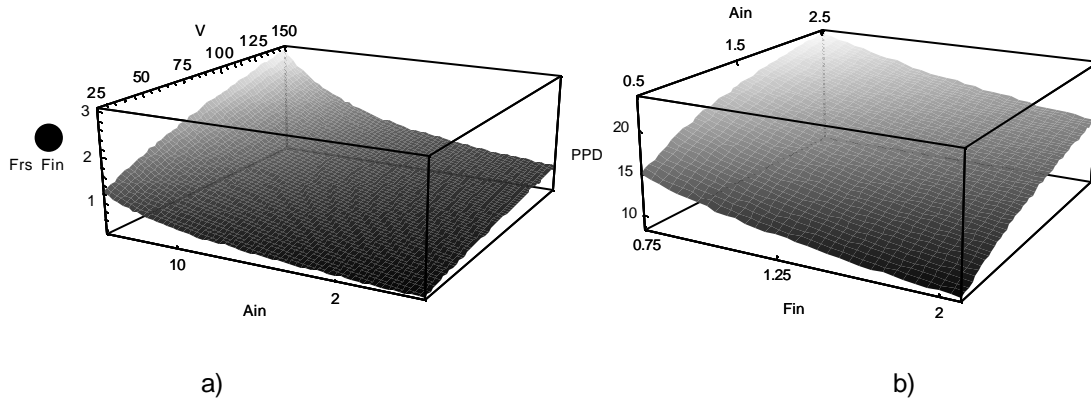


Figure 1.22

a) Ratio between the recirculation mass flow rate F_R (1.18) and the inlet volumetric flow rate (F_{IN}), for variable room volume (m^3) and inlet aperture area (A_{IN} , m^2). b) Percentage of people dissatisfied in the recirculation region of a cross-ventilated room for variable volumetric flow rate (F_{IN} (m^3/s)) and inlet aperture area (A_{IN} (m^2)), calculated using Fanger's comfort model [ISO, 1993]. Calculation performed using $L=8$ m, $T=27.5$ °C; $A_R=15$ m^2 , a metabolic rate of 1.5 met and standard summer clothing [ASHRAE, 2001].

model is based on heat transfer from the body to the environment, predicting occupant average skin temperature from expected activity and clothing levels. The model then predicts the percentage of people dissatisfied by using correlations between occupant sensation and skin temperature, obtained in laboratory tests with real subjects. The impacts of room geometry and flow rate variations on ventilation cooling, due to increased air movement, are easily quantified. As expected, higher flow rates and smaller inlet areas result in higher velocities and increased thermal comfort due to increased heat transfer.

1.8 - General guidelines for using the model

Using the model in a generic ventilation flow requires several steps that are presented here in a condensed form:

1. The airflow inlet and outlet must be in opposing room surfaces.
2. If $A^* \cong 1$ the flow resembles flow in a pipe, modeling is then straightforward and does not require correlations.
3. The room and inlet dimensions must be such that criterion (15) is met.
4. The value of C_L in (14) must be bigger than 1/3 and smaller than 11. In rooms where the perimeter of the inlet is adjacent to a lateral surface C_L must be evaluated using: $W=2.W$.
5. The temperature variation between inlet and outlet must be smaller than 2 °C.
6. When furniture is present introduce the applicable corrections.

Using the model in a software design tool is clearly the ideal situation, avoiding this sequence of steps that can easily lead to error and be quite tedious.

1 - Conclusion

The CV model developed in this chapter meets the proposed first order accuracy goal, while retaining simplicity in its form and application. A simple criterion to distinguish between different types of CV flow (C, R and CR) is introduced (section 2.1). In addition, a criterion that assesses the existence of significant momentum conservation in flows with recirculations is expressed in a simple form, Eq.1.15. The correlations presented in Eqs. 1.16-1.19 model several relevant flow parameters in a compact way, making design and control of CV systems a simpler task. The effects of furniture are treated in section 6.1 allowing for increased accuracy and better decisions on furniture placement. Section 6.4 presents examples of the benefits of the model when applied to design problems.

The obtained expressions and criterion clearly display the effects of the most relevant system geometry parameters and provide simple insight into the mechanisms that control the complex CV airflow. The functional dependences of the flow characteristics on the different room geometry parameters are clearly identified.

The present study should allow for improved understanding of CV flows and contribute to their increased use, which in turn should lead to reductions in building energy consumption and improved performance of CV systems.

2 - Heat transfer in cross-ventilated rooms

This chapter presents a study of heat transfer in cross-ventilated rooms. The results and research method presented in chapter 1 are used to develop a model for surface heat transfer in cross-ventilated rooms. Essential features of the heat transfer process, the shear layer heat transfer and surface mixed convection heat transfer coefficients, are analyzed in detail: As expected, shear layer transfer dominates the heat transfer process between recirculation and jet flow regions. The concept of a global room heat transfer coefficient is introduced and developed for three airflow patterns: perfectly mixed flow and cross ventilation, case C and R. The heat transfer characteristics of the three flow patterns are clearly displayed in the analytical expressions obtained for the global room heat transfer coefficient in each case.

In the second part of this chapter additional analysis is performed, resulting in simple models for room temperatures in ventilated rooms with internal gains. The predictions of the simplified model are compared with detailed CFD simulations of cross ventilation flows with and without internal gains.

Nomenclature

| | |
|-------------|--|
| A_{IN} : | Inlet area (m^2). |
| A_R : | Room cross section area (m^2) |
| A_S : | Total room surface area (m^2). |
| A_{SL} : | Shear layer heat transfer area (m^2) |
| C_{CM} : | Non-dimensional room confinement coefficient. |
| C_L : | Non-dimensional room aspect ratio (expression 1.18, chapter 1). |
| C_p : | Heat capacity of the air at constant pressure ($J/(Kg.K)$). |
| D_h : | Hydraulic diameter (four times the surface area over its perimeter). |
| F : | Ventilation airflow rate (m^3/s). |
| H : | Room height (m). |
| h_f : | Surface averaged forced convection heat transfer coefficient. |
| h_{FS} : | Free stream heat transfer coefficient ($W/(m^2K)$). |
| h_G : | Global heat transfer coefficient ($W/(m^2K)$). |
| h_{GM} : | Global heat transfer coefficient for the fully mixed case ($W/(m^2K)$). |
| h_{GR} : | Global heat transfer coefficient for the recirculation flow case ($W/(m^2K)$). |
| h_{MX} : | Surface averaged mixed convection heat transfer coefficient. |
| h_N : | Surface averaged natural convection heat transfer coefficient. |
| h_S : | Local surface heat transfer coefficient ($W/(m^2K)$). |
| h_{SL} : | Shear layer heat transfer coefficient ($W/(m^2K)$). |
| L : | Room length along the cross ventilation direction (m). |
| P : | Room perimeter in the direction perpendicular to the cross ventilation flow, used in case C (m). |
| Q : | Power transfer between the internal surfaces and the air flowing through the room (W). |
| $Q_{Y=0}$: | Heat transfer in the shear layer mid plane (W). |
| R : | Non-dimensional recirculation flow ratio. |
| $T(x)$: | Room air temperature, averaged in the YZ plane ($^{\circ}C$). |
| T_{IN} : | Average inlet airflow temperature ($^{\circ}C$). |

| | |
|----------------|---|
| $T_J(x)$: | Temperature in the jet region, averaged in the YZ plane (°C). |
| T_{OUT} : | Average temperature of the air leaving the room (K). |
| T_R : | Perfectly mixed room air temperature (°C). |
| $T_R(x)$: | Temperature in the section of the recirculation flow that is parallel to the jet region, averaged in the YZ plane (°C). |
| T_S : | Average inflow temperature (°C). |
| $T_W(r)$: | Temperature in the section of the recirculation that flows along the room walls, averaged in the YZ plane (°C). |
| U_Y : | Characteristic velocity of the forced flow that “drives” the forced convection boundary layer. |
| W : | Room width (m). |
| x : | Coordinate along the length of the boundary layer. |
| x_{Outlet} : | Location of the outlet along the room length (m). |
| a : | Non-dimensional factor used in the standard definition of h_G . |
| b : | Non-dimensional factor used in the standard definition of h_G . |
| e : | Correlation constant, obtained from experiments. |
| q : | Non-dimensional factor characterizing ventilation air heating effect. |
| DT : | Temperature difference between air in the interior of the test chamber and the room surfaces (°C). |
| DT_J : | Temperature variation in the jet region (K). |
| DT_R : | Temperature variation in the recirculation region (K). |
| DT_{SL} : | Temperature variation in the shear layer region (K). |
| ν : | Kinematic viscosity. |
| ρ : | Air density (Kg/m ³). |

2 Introduction

Figure 2.1 shows a simple room geometry that can lead to cross-ventilation. As ventilation air flows across the room, heat transfer between airflow, room surfaces and internal heat sources occurs and the airflow temperature changes between inlet and outlet, reflecting energy conservation. The motivation behind the analysis presented here was to improve understanding of the heat transfer process between room surfaces and ventilation air.

The model that will be developed applies to CV flows that are driven by a momentum source outside the room. This source can be the wind, a mechanical ventilation system or even buoyancy, with heated air flowing across the room in its path towards a higher outlet point in another zone of the building. Cross ventilation flows often occur in wind-driven ventilation systems with inflow through

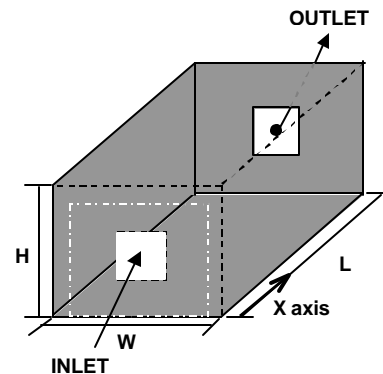


Figure 2.1

Typical compartment geometry that leads to cross-ventilation.

operable windows. Simplified ventilation simulation software tools [Feustel, 2001] are adequate for ventilation dimensioning in many design applications. In order to extend the use of these models in more precise building heat transfer analysis, such as EnergyPlus [Crawley *et al.*, 1999], it is necessary to relate accurately the predicted flow rates with the heat transfer between internal room surfaces and ventilation air. This need becomes

more significant as COMIS (a simplified software model for calculation of naturally driven airflow in multi zone buildings) is now integrated in Energy Plus [Huang, 1999].

For buildings located in hot or mild climates that have a significant amount of thermal mass the cooling load can be substantially reduced by using efficient ventilation strategies [Carrilho da Graça *et al.*, 2001]. Typically, the heat gain removal goals vary from day to night. During the day, it is desirable to remove the heat gains directly or to transfer the gains to the building thermal mass. This transfer is done through the ventilation air and room surfaces. At night, colder outside air can remove heat from the surfaces while heat gains are usually much lower, often negative. Heat transfer between air and room surfaces is important in both of these passive-cooling strategies. Its magnitude has considerable influence in the effective indoor temperature as well as in determining the success of the night cooling system.

Accurate heat transfer models are also relevant to fully mechanical and hybrid climate control systems. Several studies have shown that surface heat transfer has a large impact on energy consumption predictions in mechanical systems [Kalema & Haapala, 1995]. However, for cross ventilation flows, the required level of modeling detail is not available in most design tools used today.

We begin this analysis by looking at heat transfer between ventilation air and internal room surfaces (lateral walls, floor and ceiling). After this an analysis of the combined effect of surface heat transfer and internal gains is presented.

2.1 – Air to surface heat transfer in confined flows

Ventilation air can change temperature as it is exposed to different parts of the internal room surfaces. Often, these surfaces are flat (walls, floors, furniture etc), but, nevertheless, simple use of flat plate correlations is not possible as the forced air flow velocity or free stream air temperature are not known since the confined flow occurring in most rooms does not resemble a free stream. Figure 2.2 shows, schematically, the differences between flat plate heat transfer (2.2 a)), and two types of cross ventilation flows discussed in chapter 1 (case C in 2.2 b) and case R in 2.2 c)).

In figure 2.2 a), the boundary layer that develops exchanges heat with the environment, a heat sink, with infinite thermal capacity.

In 2.2 b) and c), the effects of flow confinement are clear, while flat plate heat

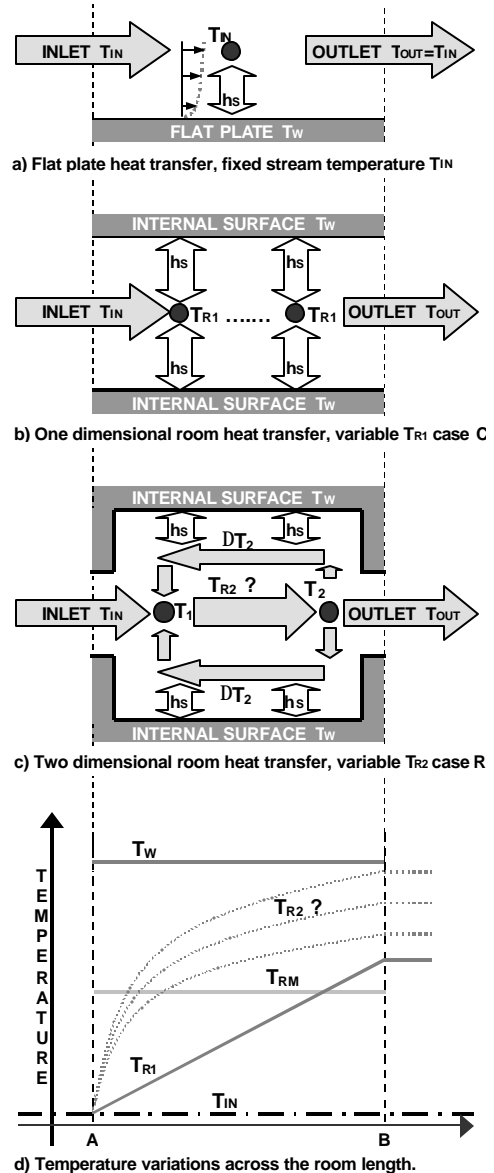


Figure 2.2

transfer occurs at constant free stream temperature ($T_{IN}=T_{OUT}$ in 2.2 a)), all room ventilation situations will have variable temperature gradients as the air temperature changes along the flow pattern (see T_{R1} and T_{R2} in figures 2.2 b), c), d)), as a consequence of heat transfer into a flow stream with limited heat capacity (that depends on the local ventilation rate in different parts of the room volume).

In a one-node, fully-mixed model the room temperature is constant (T_{RM} in figure 2.2 d)). Whenever mixing is not perfect, the temperature gradients that determine the heat transfer with the room surfaces will be incorrectly modeled. Imperfect mixing occurs in all ventilated rooms but is particularly important in cross ventilated rooms or in rooms with displacement ventilation systems (discussed in chapter 3 of this thesis). The differences between CFD simulations of recirculating flows with a fixed heat source in the recirculation region and mixed model predictions can reach 1.5°C (see figure 2.16 below). Confinement effects due to recirculation flow are also very influential in internal surface heat transfer predictions where using a perfectly mixed flow, one node model leads to errors of up to 100% (see figure 2.13 below).

2.1.1 Existing approaches.

In order to predict heat transfer in CV airflows there are currently four available options: computational fluid dynamics (CFD, using Reynolds averaged turbulence models), zonal models, fully mixed room air heat transfer models and experimental correlations.

The problems and advantages of using CFD to model room air flow and heat transfer have been discussed in the introduction of this thesis. In many situations, designers have to analyze multi room ventilation geometries, and, due to the nonlinear interactions that exist in building heat transfer processes, have the need to simulate using local measured weather spanning several days or months. In these cases, the use of CFD is impractical and simpler heat transfer models are needed.

Zonal models simulate room heat transfer by numerically solving for mass and energy conservation in a set of fully mixed zones (often less than twenty). These models generally require user identification of the dominant room airflow components (jets, boundary layers, plumes, etc.) that are “contained” in particular zones [Allard, 1992]. Because the momentum equation is not solved in the iteration procedure, an artificial flow resistance is imposed between room zones. These features make these models complex to use and often imprecise.

Experimental correlations can be a good solution to model complex physical systems. For the present problem, correlations are only available for particular cases [Chandra & Kerestecioglu, 1984, Altmayer et al., 1988, Spitler et al., 1991, Awbi & Hatton, 2000]. Application of these correlations to most geometries found in real design is difficult as the adequate correlation must be identified (by matching the design geometry to the geometries used to develop the correlations) and is often not available.

Fully mixed room air heat transfer models use a single modeling point to characterize indoor air temperature in the room. These models while simple to integrate in energy analysis software, are, in their present form, precise only when the flow is mixed. In all other cases these models fail to predict the magnitude of the heat transfer and also most

room geometry induced effects. This inaccuracy is a consequence of the use of two major approximations:

- Room air is considered fully mixed. Temperature variations inside the room are not modeled. This approximation neglects the effects of the temperature variations that occur as air moves across a room and comes into contact with internal surfaces and heat sources resulting in inaccurate calculation of the thermal capacity of the airflow. With this approximation, even if the correct local heat transfer coefficient is used the result can still be imprecise.
- Difficulties in determining the local forced convection heat transfer coefficient lead modelers to consider only natural convection, ignoring airflow pattern effects.

From a fundamental point of view, these four approaches fail in providing simple insight into the mechanisms and system parameters that control the heat transfer process. As mentioned above, highly accurate results are difficult, if not impossible, to obtain due to many uncertainties in geometry and use of the building. In this context, simplicity and correct determination of the most relevant parameters and their influence, while keeping first order accuracy is a more adequate response.

As a conceptual approach to the problem of room heat transfer in cross ventilation, with the goal of clearly displaying the effects of airflow pattern on room heat transfer, a global room heat transfer coefficient h_G is introduced. As will become clear, the global heat transfer coefficient is a compact and clear form to quantify the total heat transfer for a compartment and display the impact of the room geometry in its value. This preliminary analysis will form the basis for more complex modeling developments that will be

presented next: heat transfer with internal gains and prediction of air temperatures in cross-ventilated rooms.

2.2 - Global room surface heat transfer coefficient

The goal of the analysis presented below is to obtain a coefficient that, similarly to natural and forced convection coefficients, clearly displays the controlling parameters and physical variables that determine the heat transfer process. This coefficient is expected to display the effect of the ventilation flow pattern and the confinement effects caused by the presence of the room in the efficiency of the convective heat transfer process.

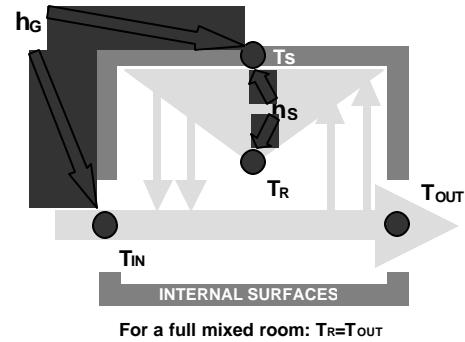


Figure 2.3

Schematic representation of the global room heat transfer coefficient in a cross-ventilated room.

Figure 2.3 shows a schematic representation of this approach: whereas the local convective heat transfer coefficient is applied using the local temperature difference ($T_s - T_R$), the global heat transfer coefficient is defined using the more easily available inflow temperature (T_{IN}). Obtaining the local temperature gradients within the room is the main difficulty when modeling room heat transfer. Therefore, one of the goals of the present analysis is to define the global heat transfer coefficient h_g without any references to the local temperature gradient (except for the weak dependence (approximate

exponent $1/3$) of the local heat transfer coefficient on local temperature gradients, see section 2.3 below). This dependence can be ignored when comparing the effects of different flow patterns but must be considered when predicting overall heat transfer.

The model that is developed below applies to steady state conditions, both in inflow rate and in room temperatures. Whenever there is a change in inflow conditions the flow and internal temperatures will change into a new steady state. The model is not applicable to these transition states. In addition this analysis uses the following approximations:

Room surfaces are considered to be at uniform temperature.

A single, temperature dependent, average surface heat transfer coefficient will be used.

The cross ventilation flows with recirculations are considered to be dominated by momentum driven flow.

No internal gains are considered.

The air enters the room through one inflow aperture surface and exhausts through a single outflow aperture located in the surface in front of the inlet.

The first approximation is not as restrictive as it may seem since, since, as a result of strong radiative coupling, internal room surfaces tend to be at approximately the same temperature in many situations. Clearly, this is not the case whenever radiant heating or cooling systems or localized solar gains are present. The use of the second approximation is essential when trying to obtain simple and compact results. In order to make the analysis presented below clearer, the examples and results shown will always

use internal surfaces that are warmer than the inflow air. The model is applicable to cases where there are different internal surface temperatures, the software implementation presented in chapter 5 allows for this additional complexity. All results obtained are applicable to the reversed configuration: the flow is Boussinesq.

In this analysis h_G will be defined for mixing, and cross ventilation systems. The analysis process begins with a perfectly mixed, zero-dimension approach and develops into one and two dimensions as more complex flows are modeled.

h_G is expected to depend on the following system characteristics:

| | |
|---------------|--|
| Temperatures: | Inlet and indoor surfaces. |
| Flow: | Airflow rate, flow regime (laminar or turbulent) and flow configuration (existence of recirculation regions or attached flow). |
| Geometric: | Inlet area, room width, height, length and area of the heated/cooled surfaces. |

h_G , is defined as:

$$Q = h_G A_S (T_S - T_{IN}) \quad (2.1)$$

In building airflows, the heat generated by viscous dissipation is much smaller than all other heat transfers. As a consequence of energy conservation, the power transferred between the internal surfaces and the air flowing through the room:

$$Q = h_G A_S (T_S - T_{IN}) = r C_p F (T_{OUT} - T_{IN}) \quad (2.2)$$

2.2.1 - Defining h_G in, zero-dimension, perfectly mixed flows

In a room with a perfectly mixed flow the interior is isothermal and there is a unique temperature difference between room air and internal surfaces. In this case, whenever the room has fixed airflow rate, and fixed inlet and surface temperatures, the local heat transfer coefficient (h_S) has a single value for each surface orientation (as opposed to varying locally for each surface). This is different from unmixed-flow, where the air temperature varies along the airflow path. In a mixed system the outflow temperature is equal to the mixed room air temperature (T_R , see figure 2.3) and the internal conditions can be described using a single point, it is a zero dimension system.

In order to distinguish the several global room heat transfer coefficients that will be defined a letter will be added for each case. In the present case the letter M , for mixing, is added (h_{GM}). In the present case, introducing h_S to calculate the air to room surface heat transfer and using (2.1) and (2.2) leads to an explicit analytic form for h_{GM} :

$$\begin{cases} h_S A_S (T_S - T_R) = r C_p F (T_R - T_{IN}) \\ h_{GM} A_S (T_S - T_{IN}) = r C_p F (T_R - T_{IN}) \end{cases} \quad (2.3)$$

Resulting in:

$$h_{GM} = \frac{h_S}{\frac{h_S A_S}{r C_p F} + 1} \quad (2.4)$$

$$T_R = T_{IN} \frac{h_{GM}}{h_S} + T_S \frac{h_G A_S}{r C_p F} \quad (2.5)$$

From simple analyses of 2.4, we see that:

h_{GM} increases with the volumetric flow rate and, as expected, h_{GM} is always smaller than h_S . This is not surprising since h_S is, by definition, the heat transfer coefficient that is applicable when directly exposing the compartment surfaces to outside air, with no losses of heat transfer due to confinement effects.

The fraction in the denominator is a non-dimensional system parameter that scales airflow rate heat capacity with surface heat transfer capacity. This factor could have been guessed by inspection and use of dimensional analysis principles. Say what it means physically

Expression 2.4 displays the known fact that, when all room parameters are fixed, increasing the flow rate always increases the heat removed by the room airflow. Increasing the flow rate reduces the temperature variation between inlet and outlet. This reduced temperature change increases the average temperature difference between air and room surfaces, increasing heat transfer. In addition, the heat transfer coefficient also increases with temperature difference. The combined effect is an increase in the overall heat transfer when the flow rate increases (observable in figure 2.4).

At this point it is useful to define the room confinement coefficient as the ratio between the global room heat transfer coefficient and the free stream heat transfer coefficient for the same set of room surfaces:

$$C_{CM} = \frac{h_{GM}}{h_{FS}} \quad (2.6)$$

In section 2.3 a set of surface heat transfer coefficients will be introduced and details of how the mixed convection heat transfer coefficient is calculated are presented (using (1.26)). When calculating h_{FS} these correlations are used with the air temperature equal to T_{IN} . In order to make comparison possible, the same forced convection coefficients are used in both cases (predicted using correlation 1.26). The variation of C_{CM} with flow rate and

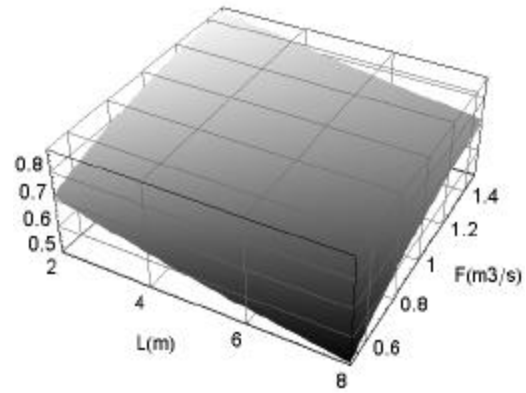


Figure 2.4

Variation of the room confinement coefficient C_{CM} with inflow rate and room length for perfectly mixed flow. $A_{IN}=2\text{m}^2$, $W=9\text{m}$ and $H=2.25\text{m}$.

room length for the perfectly mixed airflow pattern (equivalent to varying surface area since the width and length in these case are fixed) is shown in figure 2.4.

This coefficient displays the following properties:

$C_{CM} < 1$, as expected, since free stream heat transfer is more efficient than confined heat transfer.

The coefficient increases with airflow rate as result of increased heat capacity of the airflow stream. Since, in the free stream case, the air stream has infinite thermal capacity any increase in air stream heat capacity makes the confined case closer to the free case.

2.2.2 - Defining h_g for one and two dimension cross ventilation flows

We now proceed to develop the concept of global room heat transfer for CV flows of type C (see figure 1.4) and type R (recirculating, also shown in figure 1.4). As a consequence of the flow pattern characteristics, defining the global heat transfer coefficient becomes increasingly complex, as we proceed from zero to two dimensions:

Zero dimensions: for mixing ventilation.

One dimension: for CV case C.

Two dimensions: for CV cases R.

2.2.2.1 - Case C

In this case the ventilation flow is similar to flow in a channel, or in a corridor. As discussed in chapter 1, this cross ventilation flow pattern develops whenever the inlet area is similar to the room cross section (see dash dot white line in figure 2.1). When the average internal surface temperature is higher than the inflow temperature, we can expect the ventilation flow to increase its temperature along the path monotonically from inlet to outlet.

In this simpler cross ventilation case there are no recirculation regions and the heat transfer process can be modeled using a simple differential equation. The perimeter (P) along which the heat transfer occurs can be simply obtained by dividing the total internal surface area by the room length:

$$P = \frac{A_s}{L}, \quad x_{Outlet} = L \quad (2.7)$$

The equation for the variation of the temperature along the x-axis for flow in a compartment with heated surfaces with temperature (T_s) using a fixed value for the heat transfer coefficient is:

$$r.C_p.F.\frac{\partial T(x)}{\partial x} = P.h_s.(T(x) - T_s) \quad (2.8)$$

And the solution is:

$$T(x) = T_s - e^{\frac{h_s.P.x}{r.C_p.F}} (T_s - T_{IN}) \quad (2.9)$$

The value of the coefficient of x in the exponent is small for typical compartments. As a consequence, it is possible to use a further approximation: linear temperature variation. Another approximation that simplifies the result is evaluating the heat transfer coefficient at the intermediate value of the temperature variation (see figure 2.5 for an evaluation of the error introduced by the two approximations).

In this case h_{GC} is obtained by solving the following system of equations:

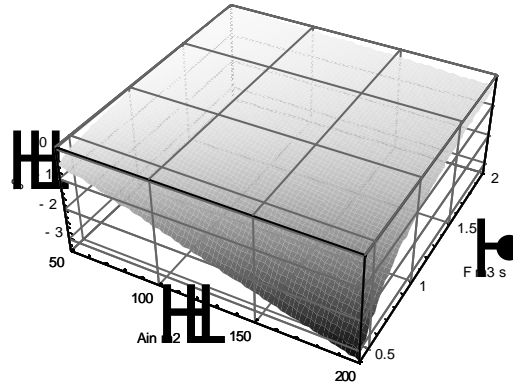


Figure 2.5

Error resulting from the using a linear temperature variation and an average heat transfer coefficient in the solution for case C (expression 2.11).

The reference solution is analytic with exponential temperature variation and variable heat transfer coefficient. This plot was obtained using: $T_s=30^\circ\text{C}$ and $T_{IN}=26^\circ\text{C}$, within the temperature variation considered in this study ($0.5^\circ\text{C} < |T_s - T_{IN}| < 10^\circ\text{C}$) the temperature difference has a small impact on the error introduced by the approximations.

$$\begin{cases} r.C_p.F.DT = A_s.h_s \left(T_s - T_{IN} - \frac{DT}{2} \right) \\ r.C_p.F.DT = A_s.h_{GC}.(T_s - T_{IN}) \end{cases} \Rightarrow h_{GC} = \frac{h_s}{\frac{h_s.A_s}{r.C_p.F} \frac{1}{2} + 1} \quad (2.10)$$

Using this definition, the temperature variation along the x direction is given by:

$$T(x) = T_{IN} + \frac{h_{GC} A_s (T_s - T_{IN})}{r C_p F} \frac{x}{L} \quad (2.11)$$

The analytical expression for the global heat transfer coefficient (2.9) is very similar to the fully mixed case, the difference is in the $\frac{1}{2}$ factor that multiplies the non- ratio in the denominator. As a consequence of this factor the one dimensional heat transfer coefficient is always higher than the fully mixed one. It is more effective to exchange heat with the surfaces of a compartment in a case C configuration than in fully mixed mode. This is due to the higher temperature difference between air and surfaces: whereas in a perfectly mixed system the air is at outflow temperature in the whole room, in case C air only reaches outflow temperature at the outlet (see lines labeled T_{RM} and T_{R1} in figure 2.2).

When the temperature dependent heat transfer coefficient is used an analytical solution is also possible but is quite cumbersome with dependence on the temperature difference in several terms, making simple interpretation impossible. A comparison between the solution in (2.11) and the more complex, exact solution is shown in figure 2.5.

2.2.2.2 - Case R with perfect mixing between jet and recirculation

Figure 2.6 shows the locations of the points used in zoning the heat transfer model for the cross ventilation case R. In the first part of this analysis we will consider perfect mixing between jet and recirculating flow as the two streams join, in point A.

Although perfect mixing between the two streams is an idealized condition that never occurs, it is useful to start this analysis with this case, since it makes testing the effects of flow confinement in the recirculation as the only heat transfer reducing flow feature possible. After this analysis we will obtain h_G for the more realistic case of partial mixing between jet and recirculation flows.

We consider that ventilation air enters the room with temperature T_{IN} . As the inlet jet entrains room air in the initial

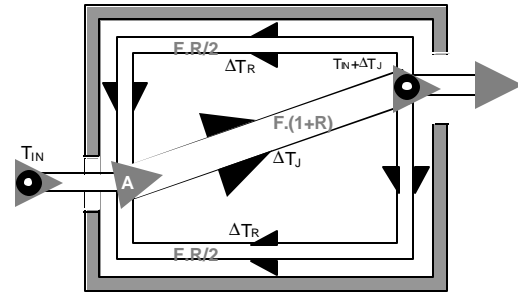


Figure 2.6

Top view of the compartment with the temperature calculation points used in the model.

The jet and recirculation flows mix in point A. For simplicity we consider that the two recirculation flows are symmetric (similar flow rate: $F.R/2$).

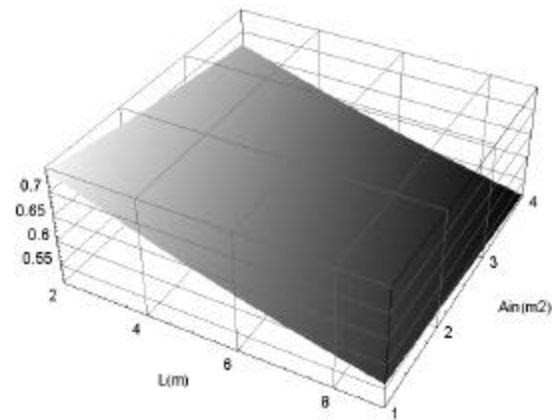


Figure 2.7

Variation of the room confinement coefficient with inflow rate and room length for perfectly mixed flow. $A_{IN}=2m^2$, $W=9m$ and $H=2.25m$.

part of its propagation path, it changes its temperature by an amount DT_J (the difference between inflow and outflow temperature, see figure 2.6) as a result of perfect mixing with the entrained air from the recirculation region (this stream is heated in contact with the room surfaces that are at different temperature from the inlet air). As it approaches the outlet, the main jet flow rejects the entrained air and exits the room with temperature $T_{IN}+DT_J$. As the jet expels air, it feeds the recirculation flow that will exchange heat with the room surfaces and be re-entrained. In the recirculation, the air has a temperature change of DT_R and returns to point A where it merges with the inlet flow with temperature: $T_{IN}+DT_J+DT_R$.

To model this case we use the correlation for airflow rate in the recirculation flow, developed in chapter 1 (we restrict our attention to room with limited length, such that $C_L < 4$, see (1.18)), presented here in a modified form so as to define the ratio (R) between recirculation and inflow airflow rates:

$$R = 0.147 \sqrt{\frac{L A_R}{A_{IN}^{3/2}}} , \quad (2.12)$$

The flow rate in the recirculation can be obtained by multiplying the flow rate F by 2.12 (see, in figure 2.5, the gray airflow rate indications, with $F.R/2$ in each of the two recirculations shown). A relation between the temperature variation in the jet and recirculation regions can be obtained by imposing energy conservation on the mixed flow that occurs in the center of the room (with flow rate: $F.(1+R)$, see figure 2.5):

$$r C_p F R (T_{IN} + DT_R + DT_J) + r C_p F T_{IN} = r C_p F (1+R) (T_{IN} + DT_J) \quad (2.13)$$

Resulting in the simple relation between DT_R and DT_J :

$$DT_J = DT_R R \quad (2.14)$$

The flow in the recirculation is similar to case C and, for simplicity, similar approximations are used: linear temperature increase and evaluation of the temperature difference and surface heat transfer coefficient using the average recirculation flow temperature. The system of equations that must be solved is then:

$$\begin{cases} rC_p FR DT_R = A_s h_s (T_s - (DT_J + T_{IN}) - DT_R / 2) \\ rC_p FR DT_R = A_s h_G (T_s - T_{IN}) \end{cases} \quad (2.15)$$

Solving these two equations results in two predictions, the global heat transfer coefficient:

$$h_G = \frac{h_s}{\frac{h_s A_s}{r C_p F} \left(\frac{1}{2R} + 1 \right) + 1} \quad (2.16)$$

As expected, expression (2.16) predicts lower heat transfer values, when compared with the mixed case (2.4). The additional multiplying term in the denominator (that distinguished this expression from the mixed case) is always bigger than one and approaches one as the recirculation flow ratio increases. The maximum temperature in the recirculation region (T_{RM}) is given by:

$$h_G = T_{IN} + (T_s - T_{IN}) \frac{h_G A_s}{r C_p F R} \quad (2.17)$$

Figure 2.7 shows the ratio between (2.16) and the average heat transfer coefficient in the free stream case (the confinement coefficient). The reducing effect on the heat transfer process resulting from the recirculation is clearly shown: even when there is perfect mixing between the jet and recirculation regions the existence of the recirculation region clearly reduces the overall, global heat transfer coefficient. The plot was obtained using a fixed room cross section area, therefore, increasing the room length leads to increased room surface area and overall heat transfer. As more heat is transferred the reducing effect of the recirculations on overall heat transfer increases. When compared with the more complex solutions presented below the effects of variation of inflow area are smaller (since shear layer mixing effects are not considered).

2.2.2.3 - Case R with partial mixing between jet and recirculation

In most cross ventilation flows with recirculations the mixing between recirculation and inflow jet is only partial. Figure 2.8 shows a schematic representation of the heat transfer process. When dealing with this more complex configuration we introduce two additional approximations:

- The progressive mass exchange between recirculation and jet flow is ignored. We will consider that the recirculation flow has fixed flow rate at all times, given by $F.R.$
- There is no heat exchange between adjacent recirculation flow streams (labeled W and R in figure 2.7).

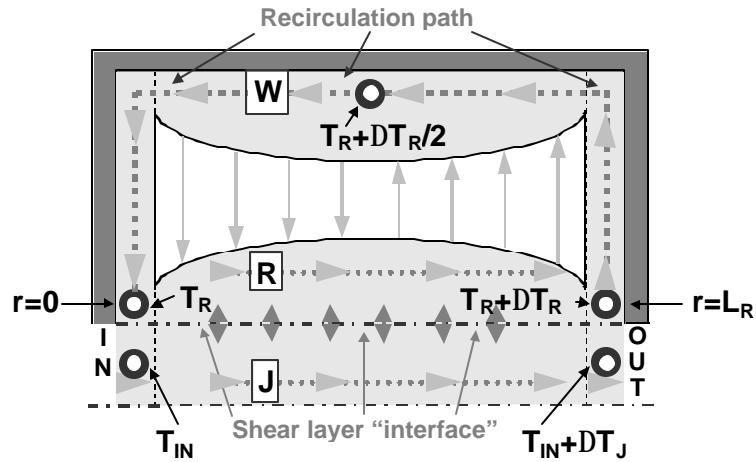


Figure 2.8

Top view of the flow structure in case R.

The light gray arrows show flow direction. The dark gray arrows show heat transfer in the shear layer. The recirculation region coordinate system is shown in the figure, with coordinate r varying between 0 and L_R .

With these approximations the flow is divided into three distinct streams with connected temperature variations:

- The main jet (labeled J in the figure).
- The part of the recirculation flow that exchanges heat with the jet (label R).
- The wall boundary layer part of the recirculation flow (label W).

Heat transfer in a shear layer

An approximate analytical solution for the heat exchange between jet and recirculation flows is presented in appendix B. We reproduce here the main result. It is

possible to use a formulation with a heat transfer area, a convection heat transfer coefficient and an average shear layer temperature difference:

$$Q_{y=0} = A_{SL} h_{SL} DT_{SL} \quad , \quad A_{SL} = L P, \quad h_{SL} = \frac{r C_p F}{C_D A_{IN} 4s \sqrt{p}} \quad (2.18)$$

Locally, the heat transfer process is driven by the variable, local, temperature difference:

$$r C_p F \frac{\partial T_J(x)}{\partial x} = - \frac{A_{SL} h_{SL}}{L} (T_J(x) - T_R(x)) = \frac{P (T_J(x) - T_R(x))}{C_D A_{IN} 4s \sqrt{p}} \quad (2.19)$$

Solution using linear approximations

The shear layer heat transfer results presented above will be used to characterize heat transfer between the R and J streams shown in figure 2.7. To model the shear layer heat transfer process there is a need to solve an additional differential equation. As a starting point in this analysis we will solve an approximate system of equations, where the overall heat transfer across the shear layer is estimated by considering that each of the two layers has a constant temperature, equal to the average between the beginning (at $x=0$) and the end ($x=L$) of the shear layer heat transfer surface:

$$r C_p F (T_J(L) - T_J(0)) = -A_{SL} h_{SL} \left((T_J(x) - \frac{DT_J}{2}) - (T_R(x) + \frac{DT_J}{2}) \right) \quad (2.20)$$

Using (2.14) we obtain a simple, first order approximation expression:

$$r C_p F DT_J = -A_{SL} h_{SL} \left((T_J(0) - T_R(r) + DT_R \frac{R+1}{2}) \right) \quad (2.21)$$

This expression may result in significant errors for very long rooms where the first order approximation used in 2.21 results in overestimation of the shear layer heat transfer. For this reason we only use this approximation as a first step in the analysis. The system of three equations to be solved is:

$$\begin{cases} r C_p F R DT_R = A_S h_S (T_S - (DT_J + T_{IN}) - DT_R / 2) \\ r C_p F DT_J = -A_{SL} h_{SL} (T_J(0) - T_R(r) + DT_R (R+1)/2) \\ r C_p F R DT_R = A_S h_G (T_S - T_{IN}) \end{cases} \quad (2.22)$$

The main result of this system is the global heat transfer coefficient, given by:

$$h_G = \frac{h_S}{\frac{h_S A_S}{r C_p F} + 1 + \frac{h_S A_S}{h_{SL} A_{SL}}} \quad (2.23)$$

Although this result is only approximate it is a useful due to the simplicity with which it displays the reducing effect from the shear layer heat transfer resistance (the third term in the denominator). Expression 2.23 only becomes close to the fully mixed case when the shear layer area and heat transfer coefficient are much bigger than $h_S A_S$.

Solution using differential equations

A more accurate representation of system behavior results from considering both the local heat transfer in the shear layer (varying along the x direction, driven by the temperature profiles $T_J(x)$ and $T_R(x)$) and accurately modeling the heat transfer in the wall boundary layers (with temperature $T_W(r)$). Both transfers can be modeled using differential equations, resulting in the following system of equations:

$$\left\{ \begin{array}{l} r C_p F R \frac{\partial T_W(r)}{\partial r} = \frac{A_s h_s}{L_R} (T_s - T_W(r)) \\ r C_p F R \frac{\partial T_R(x)}{\partial x} = \frac{A_{SL} h_{SL}}{L} (T_J(x) - T_R(x)) \\ r C_p F \frac{\partial T_J(x)}{\partial x} = - \frac{A_{SL} h_{SL}}{L} (T_J(x) - T_R(x)) \\ r C_p F (T_J(L) - T_{IN}) = A_s h_{GR} (T_s - T_{IN}) \end{array} \right. \quad (2.24)$$

With boundary conditions: $T_W(L_R) = T_R(0)$, $T_W(0) = T_R(L)$, $T_J(0) = T_{IN}$

The first equation in 2.24 models heat transfer in the wall layer. The second models the temperature variation of the portion of the recirculation flow that is in contact with the jet, it differs from the third equation only in a sign (the temperature variation in T_R is symmetric to the variation in T_J) and the flow rate ($F.R$ for the recirculation and F for the main jet). The fourth equation defines the global room heat transfer coefficient (h_{GR}), in a similar way as previous cases.

The global heat transfer coefficient is given by:

$$h_{GR} = \frac{r C_p R F (e^{\frac{A_{SL} h_{SL} (1+R)}{r C_p R F}} - 1) (e^{\frac{h_S A_S}{r C_p R F}} - 1)}{A_S (e^{\frac{A_{SL} h_{SL} (1+R)}{r C_p R F}} (e^{\frac{h_S A_S}{r C_p R F}} (1+R) - R) - 1)} \quad (2.25)$$

The temperature in the recirculation region is given by:

$$T_W(r) = T_S - (T_S - T_{IN}) \frac{e^{\frac{h_S A_S}{r C_p R F} L_R} (e^{\frac{A_{SL} h_{SL} (1+R)}{r C_p R F}} - 1)}{e^{\frac{A_{SL} h_{SL} (1+R)}{r C_p R F}} - e^{\frac{h_S A_S}{r C_p R F}} (1+R) + R} \quad (2.26)$$

Whenever the exponent in the first term in the numerator is small a linear approximation can be used. In this case the temperature variation in the recirculation is linear. In any case the maximum temperature in the room is $T_W(0)$.

In order to accurately compare the two-dimensional model results a numerical iterative solution was implemented using surface heat transfer correlations depending on surface orientation presented in the next section. All results presented below are obtained using a simple iterative solution method (iterating between the calculation of h_{GR} and h_S , typically five iterations are sufficient for convergence). Figures 2.9 to 2.11 show a set of plots of expressions 2.25 and 2.26 as well as the room confinement coefficient.

Expression 2.25 is too complex for simple analysis by inspection, however, by analyzing the plots and inspecting the expression, it is possible to conclude that increased room length improves heat transfer in two ways:

Linear improvement in mixing between jet and recirculation (linear increase in shear layer heat transfer area A_{SL}).

Square root increase in recirculation airflow rate (see 2.12) resulting in higher thermal capacity of the recirculation flow which in turn leads to a smaller temperature variation in the recirculation flow ultimately increasing heat transfer.

Figure 2.8 clearly displays the advantages of increased room length on the overall heat transfer in recirculating flows. It is clear in (2.4) that increased flow rate improves heat transfer in perfectly mixed flows. This increase is due to increased heat capacity in the airflow. As shown in figure 2.8, heat transfer in recirculating flows has a stronger increase with flow rate as a result of improved mixing between jet and recirculation that results from increased flow rate.

Figure 2.10 shows the non-dimensional confinement effect coefficient for recirculation flow. When compared with figure 2.4 we see a reversed variation with room length, in the recirculation case there is an increase in heat transfer for the reasons mentioned above. Also the variation with inflow rate is higher.

Figure 2.11 shows the average temperature difference in the recirculation region between mixed and recirculating flow cases. For short rooms or in rooms with large inflow area, the predicted temperature difference increases.

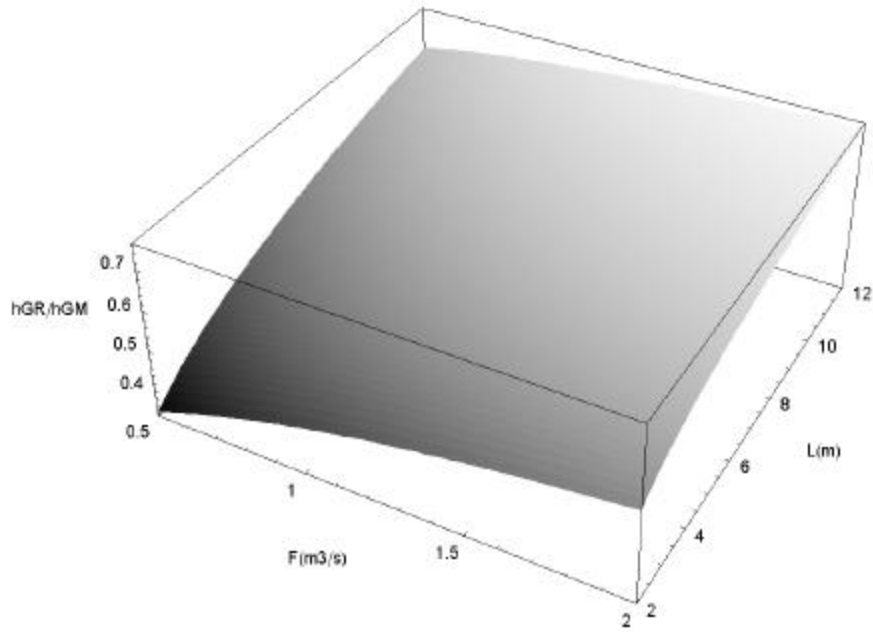


Figure 2.9

Variation of the ratio between h_G for the recirculating airflow pattern (h_{GR} , expression 2.22) and h_G for perfectly mixed flow (h_{GM} , expression 2.3) for variable inflow rate and room length.

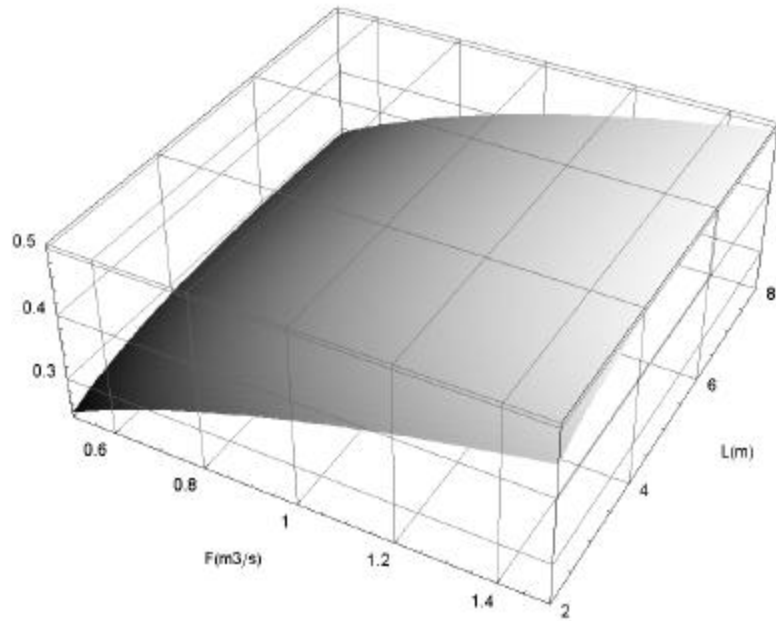


Figure 2.10

Variation of the flow confinement coefficient with inflow rate and room length.

Fractional reduction in heat transfer due to room confinement effects for the cross ventilation recirculating flow case. (h_{GR} , expression 2.22) divided by the free stream heat transfer coefficient for the same set of surfaces and orientations.

Figure 2.12 shows the variation of the average temperature in the recirculation region for variable inflow rate between $r=0$ and $r=L_R$ along the recirculation region (see recirculation coordinate system in figure 2.7). The temperature variation along the recirculation varies inversely with inflow rate (as expected from increased heat capacity of the inflow rate) between 0.5 and 1°C.

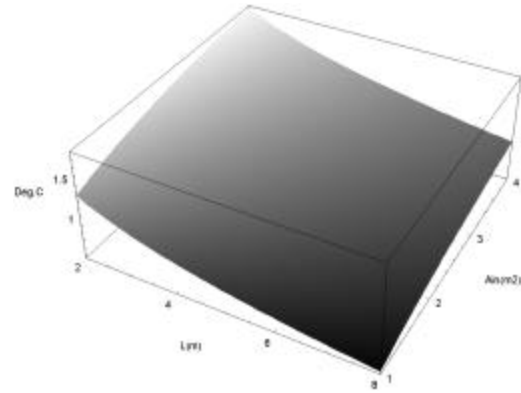


Figure 2.11

Average temperature difference in the recirculation region between recirculating and mixed flow patterns. Plot obtained by subtracting expression 2.5 from the average value of expression 2.25. Plot obtained for a room with 9m width, 2.25m height and a $1\text{m}^3/\text{s}$ inflow rate with a temperature 4°C lower than surface temperature.

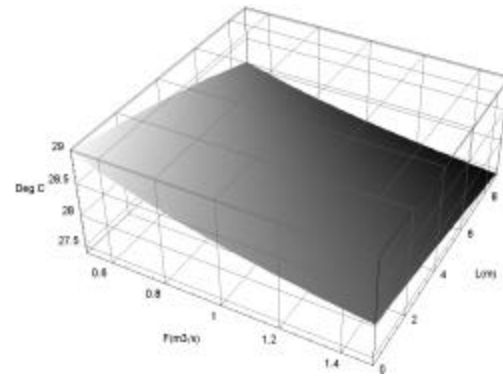


Figure 2.12

Average value of expression 2.25.

Plot obtained for a room with 9m width, 2.25m height, $A_{IN}=2\text{m}^2$ and a $1\text{m}^3/\text{s}$ inflow rate with a temperature 4°C lower than surface temperature.

2.2.3 - Simple model results.

We consider here the three analytical solutions for the global room heat transfer coefficient obtained in the previous sections. Using the special notation shown below, these three solutions differ only in the multiplying factor of the term that characterizes the losses due to confinement/heating effects and in the term that is added in the denominator. The ventilation air heating effect non-dimensional factor is given by:

$$q = \frac{h_s \cdot A_s}{r \cdot C_p \cdot F} \quad (2.27)$$

The room global heat transfer coefficient is then given by:

$$h_G = \frac{h_s}{q \cdot a + b} \quad (2.28)$$

Where the coefficients have different values depending on the flow pattern:

CV, case C $\rightarrow a = 1/2, b = 1$

Full Mixed $\rightarrow a = 1, b = 1$

$$CV, \text{ case } R \rightarrow a = \frac{(e^{\frac{A_{SL} h_{SL} (1+R)}{r C_p R F}} (e^{\frac{h_s A_s}{r C_p R F}} (1+R) - R) - 1)}{(e^{\frac{A_{SL} h_{SL} (1+R)}{r C_p R F}} - 1) (e^{\frac{h_s A_s}{r C_p R F}} - 1) R}, \quad b = 0 \quad (2.29)$$

The cases are ordered by decreasing global heat transfer coefficient (for similar room characteristics).

2.3 - Local heat transfer coefficient

This section presents a review of flat surface convection heat transfer, the second component of the room heat transfer problem as presented in figure 2.2. Curved and inclined room geometries are not treated in this work.

Internal heat sources release heat through convection with the room air and radiative exchange with the internal room surfaces. This study will only address the convective part of this heat transfer. One of the effects of the radiative heat exchanges that occur is to contribute towards making the room temperatures more uniform. Uniform room surface temperatures is one of the approximations used in the models that are being developed.

In CV flow patterns that conform to the conditions mentioned in the previous section, the flow is predominantly turbulent and there is forced flow close to the room surfaces. Since natural convection always occurs when there is a temperature difference between air and surface, room heat transfer always occurs through mixed convection.

In this context, the boundary layers that form close to the thermally active room surfaces are driven by buoyancy and momentum transferred from the dominant CV flow. In order to predict the local mixed convection heat transfer coefficient that results from these two mechanisms it is possible to use the following formula [Siebers et al., 1983]:

$$h_{MX} = (h_F^e + h_N^e)^{1/4} \quad (2.30)$$

This formula was verified experimentally [Seibers et al., 1983] and has been subsequently used in two other studies that are relevant to the present work: with vertical surfaces and horizontal forced flow [Neiswanger et al., 1987] and horizontal surfaces with horizontal and vertically impinging forced flow [Awbi&Hatton, 2000]. In all of these studies, (2.30) was found to agree better with experimental measurements when ϵ was set to 3.2.

In the present room heat transfer problem several of the configurations studied by these authors occur. In the lateral, beginning and end surfaces of the room the boundary layer geometry is similar to the two-dimensional scaled flow model experimental model [Neiswanger et al., 1987] (natural convection is perpendicular to the forced convection). On the horizontal surfaces (floor and ceiling) the boundary layer is driven by forced convection in the horizontal with buoyancy forces acting normally to these surfaces (vertically). This section proceeds by analyzing the natural and forced convection components and ends with an analysis of the combined effects, taking into account the results of the correlations presented in chapter 1.

2.3.1 - Natural convection heat transfer in flat surfaces

In a previous investigation [Awbi &Hatton, 1999] performed a set of measurements in an experimental chamber resulting in correlations for natural convection in horizontal and vertical heated room surfaces. These correlations will be used in the present model. When compared with standard flat surface heat transfer correlations, these correlations have the advantage of resulting from measurements in surfaces of a full size test

chamber, as opposed to the suspended plate based correlations commonly found in the literature. Further, the correlations predict surface average values, taking into account the laminar and turbulent contributions in the vertical boundary layers.

In the case when natural convection buoyancy flux acts into the surface, a heated ceiling, the surface average correlation obtained by [Awbi & Hatton, 1999] may not be adequate. For this case, a warm ceiling or a cold floor, it was found more appropriate to use a correlation obtained by the same authors when only part for of the ceiling surface is thermally active. When the whole ceiling is heated, a stratified environment occurs, leading to a low heat transfer value (one order of magnitude lower than the other surfaces). When only part of the ceiling is heated, recirculation cells occur, disrupting the stratification, this is closer to what happens in CVas the buoyancy fluxes from the remaining surfaces and the cross flow promote air movement close to the ceiling, disrupting the stratification. When the room surfaces are colder than the airflow, it is necessary to apply the heated ceiling correlation for the “cold” floor and vice versa.

The correlations that are used in the model are [Awbi & Hatton, 1999]:

$$\text{Vertical surfaces:} \quad h_N = \frac{1.823}{D_h^{0.121}} DT^{0.293} \quad (2.31)$$

Horizontal surfaces:

$$\text{Natural convection away from the surface:} \quad h_N = \frac{2.175}{D_h^{0.076}} DT^{0.308} \quad (2.32)$$

$$\text{Natural convection into the surface:} \quad h_N = 1.02 DT^{0.16} \quad (2.33)$$

2.3.2 - Forced convection heat transfer in flat surfaces

As explained in section 2, air enters the room in a developing jet composed of two shear layers that quickly become turbulent. Part of the air in the shear layers goes into the recirculation regions forming the wall jets or wall currents that exist in these regions. Since the air is already turbulent, there is no significant laminar region in these boundary layers. For this reason, it is a reasonable approximation to use a correlation for forced convection turbulent boundary layers in all the internal surfaces.

In these conditions it is possible to apply Colburn's analogy between heat and momentum transfers [Bejan, 1994] to estimate the forced component of the convection heat transfer. Colburn proposed the following empirical relation between momentum and convective heat transfers:

$$St_x Pr^{2/3} = \frac{1}{2} C_{fx} \quad (2.34)$$

where the skin friction coefficient, C_{fx} , and the Stanton number, St_x , are given by:

$$C_{fx} = 0.0592 \left(\frac{U_\infty x}{n} \right)^{-1/5} \quad (2.35)$$

$$St_x = \frac{h_F}{r c_p U_\infty} \quad (2.36)$$

Expressions 2.35 and 2.36 are approximations. Using these two approximations and introducing the Stanton number definition, results in:

$$h_F = r c_p U_\infty P_r^{-\frac{2}{3}} \frac{1}{2} C_{fx} = r c_p U_\infty^{\frac{4}{5}} P_r^{-\frac{2}{3}} 0.0296 \left(\frac{x}{n} \right)^{\frac{1}{5}} \quad (2.37)$$

This heat transfer coefficient has a weak dependence on x through an exponent of - 0.2. This is a consequence of boundary layer growth and the resulting reduction in the temperature gradient. Forced convection boundary layer heat transfer is not influenced by buoyancy driven transport (the turbulent eddy formation process is driven by momentum transfer), for this reason there is no temperature or orientation dependence in the result.

In a simple room heat transfer model, it is not feasible to integrate the x dependent coefficient in equation 2.37 for every room surface. Since the x dependence is small, the effects of different lengths, depending on room geometry, are smaller than the model's overall accuracy. Therefore, a further approximation is introduced: an integration is performed only once using a typical room surface length of 6 meters (a characteristic value, half way between very short rooms $L=2m$ and long rooms $L=10m$). This result will be used for all room surfaces.

Performing the integration using standard properties results in:

$$h_F \approx 4.3 U_\infty^{0.8} \quad (2.38)$$

In section 1.5, the typical velocities of the near wall return flow in the recirculations were identified. For typical room geometric and flow parameters a typical range is from 0.05 and 0.5 m/s. Using the previous formula and these values it is possible to compare

the forced and free convection coefficients and their joint effect using [Seibers et al., 1983] approximate formula (2.29).

2.3.3 - Combined effects of forced and free convection heat transfer

The formula proposed by [Seibers et al., 1983] (2.30) reflects an important feature of the mixed convection process. When the heat transfer from one of the two mechanisms in isolation is slightly higher (50%) than the other, it dominates the resultant mixed convection heat transfer process: the mixed convection heat transfer coefficient only increases by 7% when the weaker of the two coefficients is added. This behavior is observable in figure 2.13 where the combined heat transfer coefficient is plotted as a function of the near wall velocity and temperature difference. The main feature in this plot is the dominance of natural convection on the combined heat transfer process for typical geometric parameters and flow rates.

Given that natural convection is dominant in most of the plot and with the goal of introducing further simplification in the model it is useful to introduce two further regions in the plot:

$V_w > 0.2$ High near wall return velocities, the forced convection contribution must be considered. In this region, Seibers formula must be used.

$V_w < 0.2$ In this region it is possible to further approximate the mixed convection heat transfer formula, neglecting forced convection contribution.

For the purpose of estimating the heat transfer value in compartments with isothermal surfaces, we propose to use a single heat transfer coefficient for all the

perimeter of contact between the airflow and the room surfaces (the perimeter is taken in the room cross section).

In cases where natural convection dominates the mixed convection process, the following approximations can be used:

$$\begin{aligned} h_{MX} &\approx h_N, h_N \approx 1.6(T_\infty - T_w)^{1/3}, \\ q_w &= h_S(T_\infty - T_w) = 1.6(T_\infty - T_w)^{4/3} \\ q_{wA} &= a + b(T_\infty - T_w) \end{aligned} \quad (2.39)$$

The error introduced by the approximation when using linear correlation coefficients that optimize the correlation in the temperature variation region is shown in figure 2.13. The 5% error introduced by neglecting the forced convection contribution when $V_w >$

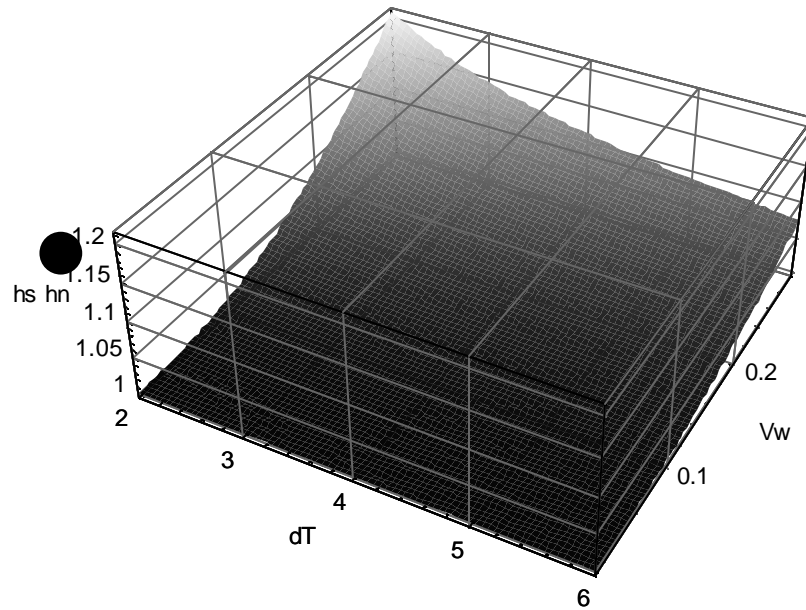


Figure 2.13

Mixed convection heat transfer coefficient, normalized using the natural convection coefficient.

On the two horizontal axis: near surface velocity (forced convection), and temperature difference (natural convection).

than 0.2m/s can be considered small compared with the error introduced by the unique perimeter heat transfer coefficient.

2.4. - Validation

Numerical validation of the cross ventilation model, for a case with a type R flow pattern, was performed using the commercial CFD package PHOENICS using the room geometries and simulation models described in section 1.5. One variation was introduced in the turbulence model, after initial exploratory simulations: the Yap [Yap, 1987] near wall length scale correction was used. This correction to the standard $k\epsilon$ model reduces turbulence levels in separation regions of the flow. Without this correction the simulations show excessive heat transfer between the R and W streams (see figure 2.3), inconsistent with experimental correlations.

2.4.1 - Geometries considered

As we introduce surface heat transfer one additional variation is added: the temperature difference between inflow and wall temperatures. With this additional parameter the number of possible simulations increases. In order to keep the task manageable, simulations were performed only for a subset of the cases presented in section 1.5. The following restrictions were used:

Only cases with $C_L < 4$ (see expression 1.14) are considered. Cases with $C_L > 4$ have an undefined character and, even in the isothermal case are close to the limit of the model. As buoyancy effects come into play in these cases the undefined character is accentuated.

Only two aperture geometries are considered in the main set of validation cases (see table 2.3).

Only two temperature differences between inflow and internal surfaces (2 and 4°C) are considered in the main set of validation cases (see table 2.3).

All surfaces are set to the same temperature.

Variations in airflow rate are introduced since heat transfer is expected to have nonlinear variation with flow rate (see previous section).

Table 2.1 - *Dimensions of the apertures used to develop and test the cross ventilation heat transfer model.*

| Aperture | Area (A_{IN} , m^2) | Perimeter (P , m) | U_{IN} (average, m/s , $F_{IN}=1m^3/s$) |
|--------------------|---------------------------|-------------------------|--|
| Window (W) | 1 | 4 | 1 |
| Door (D) | 2 | 6 | 0.5 |
| Wide door (WD) | 4 | 8 | 0.25 |

Table 2.2 - *Dimensions of the rooms used to develop and test the correlations.*

| Case | 122 | 123 | 124 | 222 | 223 | 142 | 143 | 144 | 242 |
|-------------------------|------|------|------|------|------|------|------|------|------|
| H (m) | 2.25 | 2.25 | 2.25 | 3.4 | 3.4 | 2.25 | 2.25 | 2.25 | 3.4 |
| W (m) | 4.5 | 4.5 | 4.5 | 4.5 | 4.5 | 9 | 9 | 9 | 9 |
| L (m) | 4.5 | 6.75 | 7 | 4.5 | 6.75 | 4.5 | 3.56 | 9 | 4.5 |
| V (m ³) | 46 | 68 | 71 | 69 | 103 | 91 | 72 | 182 | 138 |
| A_R (m ²) | 10.1 | 10.1 | 10.1 | 15.3 | 15.3 | 20.3 | 20.3 | 20.3 | 30.6 |

2.4.2 - Results

The results of the CFD simulations, as well as fully mixed and recirculating flow models are shown in tables 2.3-2.5. Figure 2.13 shows comparative results between CFD and the two simplified models.

Table 2.3. Results of the simulations for the cases with inflow opening of type D (see table 1). Q_{CFD} : total surface heat transfer predicted using CFD. Q_{CVR} : total surface heat transfer predicted using the cross ventilation, recirculating flow model. Q_M : total surface heat transfer predicted using the fully mixed model. Error(%): percentage error of the two models when compared with the CFD predictions.

| Case | A_S (m ²) | DT (°C) | F (m ³) | Q_{CFD} (W) | Q_{CVR} (W) | | Q_M (W) | |
|---------|-------------------------|-----------|-----------------------|---------------|---------------|-----------|-----------|-----------|
| | | | | | | Error (%) | | Error (%) |
| D144T21 | 239.0 | 2.0 | 1.0 | 542.0 | 512.3 | -5 | 685.7 | 27 |
| D144T25 | 239.0 | 2.0 | 0.5 | 351.1 | 335.1 | -5 | 481.6 | 37 |
| D144T41 | 239.0 | 4.0 | 1.0 | 1159.0 | 1106.4 | -5 | 1512.1 | 30 |
| D144T45 | 239.0 | 4.0 | 0.5 | 772.1 | 713.0 | -8 | 1055.2 | 37 |
| D222T21 | 97.2 | 2.0 | 1.0 | 283.3 | 256.5 | -9 | 361.5 | 28 |
| D222T25 | 97.2 | 2.0 | 0.5 | 169.8 | 176.5 | 4 | 284.9 | 68 |
| D222T41 | 97.2 | 4.0 | 1.0 | 590.3 | 561.9 | -5 | 821.2 | 39 |
| D222T45 | 97.2 | 4.0 | 0.5 | 357.0 | 381.8 | 7 | 647.5 | 81 |
| D223T21 | 132.7 | 2.0 | 1.0 | 358.6 | 347.0 | -3 | 463.1 | 29 |
| D223T25 | 132.7 | 2.0 | 0.5 | 218.8 | 237.9 | 9 | 351.1 | 60 |
| D223T41 | 132.7 | 4.0 | 1.0 | 740.3 | 759.0 | 3 | 1041.1 | 41 |
| D223T45 | 132.7 | 4.0 | 0.5 | 468.4 | 513.9 | 10 | 787.8 | 68 |

Table 2.4. Results of the simulations for the cases with inflow opening of type W (see table 1). Q_{CFD} : total surface heat transfer predicted using CFD. Q_{CVR} : total surface heat transfer predicted using the cross ventilation, recirculating flow model. Q_M : total surface heat transfer predicted using the fully mixed model. Error(%): percentage error of the two models when compared with the CFD predictions. The column labeled (C.6) refers to the value of the non dimensional factor in expression 6 of appendix C.

| Case | A_s (m ²) | DT | F (m ³) | (C.6) | Q_{CFD} (W) | Q_{CVR} (W) | | Q_M (W) | |
|---------|-------------------------|-----|-----------------------|-------|---------------|---------------|-----------|-----------|-----------|
| | | | | | | | Error (%) | | Error (%) |
| W122T21 | 79.0 | 2.0 | 1.0 | 0.2 | 235.3 | 271.1 | 15 | 352.2 | 50 |
| W122T25 | 79.0 | 2.0 | 0.5 | 0.4 | 194.4 | 183.0 | -6 | 257.4 | 32 |
| W122T41 | 79.0 | 4.0 | 1.0 | 0.2 | 544.2 | 581.9 | 7 | 770.2 | 42 |
| W122T45 | 79.0 | 4.0 | 0.5 | 0.6 | 456.3 | 398.4 | -13 | 578.4 | 27 |
| W123T41 | 109.4 | 4.0 | 1.0 | 0.4 | 766.5 | 789.0 | 3 | 999.3 | 30 |
| W123T45 | 109.4 | 4.0 | 0.5 | 1.0 | 509.7 | 534.4 | 5 | 721.2 | 41 |
| W123T21 | 109.4 | 2.0 | 1.0 | 0.3 | 347.0 | 368.7 | 6 | 461.0 | 33 |
| W123T25 | 109.4 | 2.0 | 0.5 | 0.7 | 246.0 | 246.2 | 0 | 325.0 | 32 |
| W142T25 | 139.8 | 2.0 | 0.5 | 0.4 | 228.9 | 237.9 | 4 | 364.8 | 59 |
| W142T41 | 139.8 | 4.0 | 1.0 | 0.3 | 651.5 | 775.2 | 19 | 1108.6 | 70 |
| W142T45 | 139.8 | 4.0 | 0.5 | 0.7 | 576.6 | 510.6 | -11 | 811.4 | 41 |
| W144T21 | 241.0 | 2.0 | 1.0 | 0.5 | 537.0 | 592.1 | 10 | 742.1 | 38 |
| W144T25 | 241.0 | 2.0 | 0.5 | 1.2 | 403.8 | 384.3 | -5 | 500.5 | 24 |
| W144T41 | 241.0 | 4.0 | 1.0 | 0.7 | 1239.5 | 1268. | 2 | 1606.9 | 30 |
| W144T45 | 241.0 | 4.0 | 0.5 | 1.7 | 818.7 | 820.7 | 0 | 1087.2 | 33 |
| W222T41 | 99.2 | 4.0 | 1.0 | 0.3 | 629.6 | 652.9 | 4 | 882.9 | 40 |
| W222T45 | 99.2 | 4.0 | 0.5 | 0.6 | 474.1 | 445.9 | -6 | 672.1 | 42 |
| W222T21 | 99.2 | 2.0 | 1.0 | 0.2 | 287.1 | 301.3 | 5 | 397.7 | 39 |
| W222T25 | 99.2 | 2.0 | 0.5 | 0.4 | 211.5 | 205.3 | -3 | 298.5 | 41 |
| W242T25 | 170.1 | 2.0 | 0.5 | 0.5 | 250.6 | 258.4 | 3 | 409.9 | 64 |
| W242T21 | 170.1 | 2.0 | 1.0 | 0.2 | 347.1 | 392.3 | 13 | 558.1 | 61 |
| W242T41 | 170.1 | 4.0 | 1.0 | 0.3 | 745.6 | 848.5 | 14 | 1244.2 | 67 |
| W242T45 | 170.1 | 4.0 | 0.5 | 0.7 | 591.4 | 552.5 | -7 | 910.2 | 54 |

Table 2.5. Results of the simulations for the cases with inflow opening of type WD and W (see table 1), with similar surface area. Q_{CFD} : total surface heat transfer predicted using CFD. Q_{CVR} : total surface heat transfer predicted using the cross ventilation, recirculating flow model. Q_M : total surface heat transfer predicted using the fully mixed model. Error(%): percentage error of the two models when compared with the CFD predictions. The column labeled (C.6) refers to the value of the non dimensional factor in expression 6 of appendix C.

| Case | $A_S (m^2)$ | $DT (°C)$ | $F (m^3)$ | (C6) | $Q_{CFD} (W)$ | $Q_{CVR} (W)$ | | $Q_M (W)$ | |
|----------|-------------|-----------|-----------|------|---------------|---------------|-----------|-----------|-----------|
| | | | | | | | Error (%) | | Error (%) |
| WD142T25 | 112.6 | 2.0 | 0.5 | 1.2 | 163.6 | 131.6 | -20 | 298.1 | 82 |
| WD142T41 | 112.6 | 4.0 | 1.0 | 0.7 | 450.8 | 443.1 | -2 | 857.3 | 90 |
| WD142T21 | 112.6 | 2.0 | 1.0 | 0.4 | 176.4 | 205.4 | 16 | 373.5 | 112 |
| W124T41 | 112.7 | 4.0 | 1.0 | 0.5 | 786.5 | 810.8 | 3 | 1023. | 30 |
| W124T25 | 112.7 | 2.0 | 0.5 | 0.7 | 249.5 | 252.8 | 1 | 331.8 | 33 |

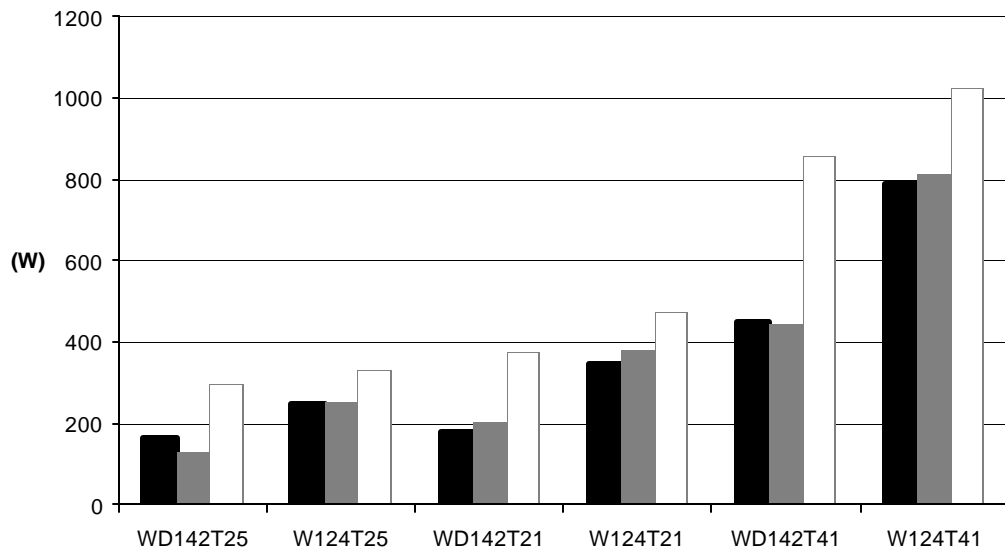


Figure 2.13

Comparison between the predictions of the two models and the numerical validation for the cases in table 5. In black the CFD results, in gray CV case R model results, in white mixed flow model.

2.4.3 - Analysis

We initiate the discussion of the results by analyzing two distinct cases with similar surface area. The case of a short room (case *WD142*, $L=3.6\text{m}$) with a large door as the inflow surface ($A_{IN}=4\text{m}^2$) and the case of a long room (*W124*, $L=7\text{ m}$) with a small window as the inflow surface ($A_{IN}=1\text{m}^2$). The goal of these two extreme geometries is to display the effects of the recirculation flow and to display the effects of variations in the properties of the recirculation flow. For case *WD142* the recirculating flow model is expected to predict lower heat transfer for three reasons:

- The increase in shear layer heat transfer area (the inflow perimeter increases with $A_{IN}^{0.5}$) is not sufficient to compensate for the decrease in characteristic velocity of the shear layer transfer process (decreases with $1/A_{IN}$).
- The forced convection coefficient is expected to be lower in case *WD142* as a result of a lower inflow velocity.
- The flow rate in the recirculation region is also lower in case *WD142*.

Except for changes due to forced convection, the fully mixed approach will predict similar overall surface heat transfer values (in fact a 25% difference is predicted as a result of the use of the forced convection correlation).

Comparison between CFD and CVR results for these cases reveals very positive results (confirmed by the remainder of the cases in the database):

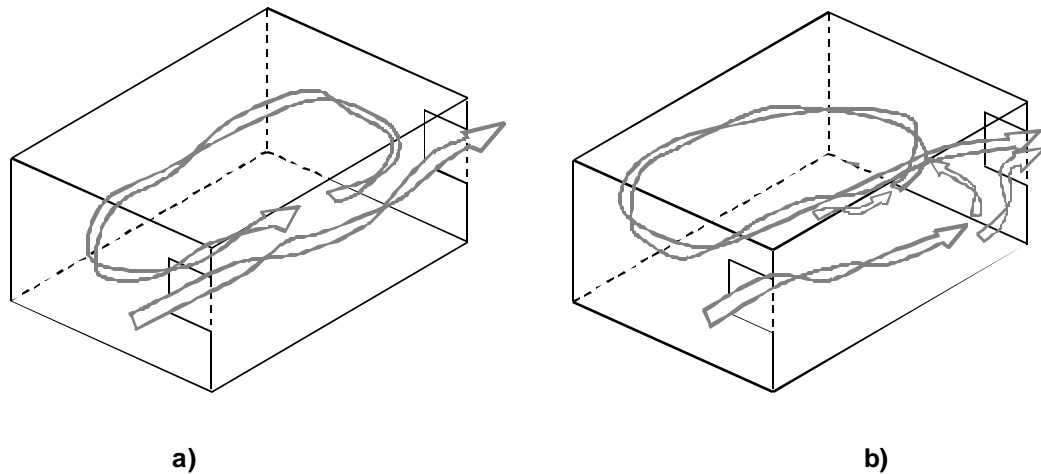


Figure 2.14

Schematic view of two possible recirculation flow behaviors.

- a) the recirculation flow develops horizontally and the outflow is dominated by the jet.
- b) when buoyancy effects are important a more complex flow pattern develops. The recirculation flow moves vertically along its path and the outflow is a combination of jet and recirculation flow.

- The recirculating flow model is able to predict overall heat transfer with accuracy: maximum error 20%, average error 7%.
- The recirculation flow model accurately predicts the trend in overall heat transfer change between the two cases. For cases: *WD142T41* *W124T41*. The model predicts the heat transfer variation within 3%.
- The mixed flow model consistently over predicts the heat transfer value.
- The mixed flow model does not reflect the 50% variation in heat transfer between the two cases.

As discussed, the existence of the recirculations has a reducing effect on overall heat transfer. It is then acceptable to ask whether this reduction could be modeled by

introducing a reduction factor on the surface heat transfer coefficient. The benefits of this analysis and the simplified solutions would not be lost, but a simpler modeling approach would be possible.

When trying to obtain such an ideal factor for the cases described above it becomes clear that this option leads to significant inaccuracy: at best it is possible to obtain an under prediction of 16% in some cases and an over prediction of 20% in others. Further, when this optimized factor is used in the remaining cases that compose the validation, a systematic under prediction of 10-20% is obtained. This is not to say that using such a factor does not represent an improvement over the existing approach, it just does not seem to be superior to the improved model. Also, it is important to analyze the results with no changes in order to display and test the ability to characterize the effects of the flow pattern, the object of the present work.

Heat gains can also affect the airflow pattern and, whenever the heat gains are very high the flow structure can change and the modeling approach can become inadequate. Figure 2.14 a) shows a schematic depiction of the expected flow pattern that forms the base of the model. The recirculation flow follows an horizontal path exchanging heat and momentum with the main jet flow.

As buoyancy effects become stronger the flow starts to resemble case 2.14b). In this case the recirculation not only exchanges with the main jet flow but is also able to reject heat directly by composing part of the outflow. Appendix D presents a scaling factor that can be used to access model applicability. Still, further work is needed to clearly define model applicability.

2.5 - Heat transfer in recirculating flows with internal gains

Whereas surface heat transfer is an important component of room heat transfer, internal gains often dominate the room temperature field and cannot be ignored. Referring to the previously used subdivision of the room into jet and recirculation regions we can see that gains can occur exclusively in the jet region, exclusively in the recirculation region or in both regions. We will focus our attention on heat gains in the recirculation region (non buoyant pollutant sources will be treated in part four) since it presents the biggest challenge (since case *C* is more complex than case *R*).

The effect of gains in the jet region on room air temperature distribution is simpler to model and, within the first order accuracy goal, can be characterized as follows:

- For gains occurring in the jet region (between the inlet and the room outlet) a change in inflow temperature is an adequate, conservative approximation. From energy conservation we conclude that the altered inflow temperature is given by:

$$T_{ING}=T_{IN}+G_J/(r.C_P.F). \quad (2.39)$$

- Gains occurring in the jet region, close to the outlet can be ignored in a first order accuracy model.

Clearly the two approaches described above are only exact when: the gains occur at the inlet and perfectly mix with the inflow jet (for the first case), and whenever the gains occur very close to the outlet (in the second case). In all other situations, the first approach provides a conservative approximation.

2.5.1 - Temperature distribution in rooms with internal gains in the recirculation region

When heat gains occur in the recirculation region significant heat accumulation occurs due to the limited heat transfer ability of the shear layer. Due to this limited ability, the recirculation is partially isolated from the main jet flow and higher temperatures are generated in this region whenever heat gains are present. The concept of a global heat transfer coefficient is not applicable.

In the case of a flow in a room with adiabatic surfaces and heat gains in the recirculation region the indoor air temperatures can be predicted using the solution to the following system of equations:

$$\begin{cases} r C_p F R (T_R(0) - T_R(L)) = G_R \\ r C_p F R \frac{\partial T_R(x)}{\partial x} = \frac{A_{SL} h_{SL}}{L} (T_J(x) - T_R(x)) \\ r C_p F \frac{\partial T_J(x)}{\partial x} = -\frac{A_{SL} h_{SL}}{L} (T_J(x) - T_R(x)) \end{cases} \quad (2.40)$$

This system of equations differs from system 2.24 in several ways. Because there is no wall heat transfer there is no need to split the recirculation flow in two parts (R and W). The temperature increase in the recirculation flow is simply defined by the internal gains (first equation in 2.40). The second and third equations in 2.40 model shear layer heat transfer are similar in the two cases (2.24 and 2.40).

The recirculation flow temperature at $x=0$ is given by:

$$T_R(0) = T_{IN} + \left(\frac{1}{e^{\frac{A_{SL} h_{SL} (1+R)}{r C_p F R}} - 1} + 1 \right) \frac{G_R (1+R)}{r C_p F R} \quad (2.41)$$

The temperature in the recirculation is inversely proportional to the recirculation flow ratio (R) and the shear layer area (measured by the product: $A_{SL} h_{SL}$). As both of these parameters increase this expression tends to (2.39). The recirculation flow temperature at $x=L$ is given by:

$$T_R(L) = T_R(0) + DT_R \quad (2.42)$$

The temperature variations in the recirculation flow is given by:

$$DT_R = \frac{G_R}{r C_p F R} \quad (2.43)$$

2.5.2 - Combined effects of surface heat transfer and internal gains in the recirculation region

In this case, the following system of equations must be solved:

$$\begin{cases} r C_p F R \frac{\partial T_w(r)}{\partial r} = -\frac{A_s h_s}{L_R} (T_s - T_w(r)) - \frac{G_R}{L_R} \\ r C_p F R \frac{\partial T_R(x)}{\partial x} = \frac{A_{SL} h_{SL}}{L} (T_J(x) - T_R(x)) \\ r C_p F \frac{\partial T_J(x)}{\partial x} = -\frac{A_{SL} h_{SL}}{L} (T_J(x) - T_R(x)) \end{cases} \quad (2.44)$$

With the boundary conditions: $T_w(L_R) = T_R(0)$, $T_w(0) = T_R(L)$, $T_J(0) = T_{IN}$.

This system of equations differs from 2.24 in two ways: the fourth equation is not used since the concept of global room heat transfer is not applicable to this case and the heat gains in the recirculation are added to the first equation. For simplicity the heat gains are considered to be evenly distributed along the recirculation path.

The temperature variation in the recirculation region is given by:

$$T_w(r) = T_s + \frac{G_R}{A_s h_s} - \frac{e^{\frac{h_s A_s}{r C_p R F L_R}} \left(e^{\frac{A_{SL} h_{SL} (1+R)}{r C_p R F}} - 1 \right) (G_R + A_s h_s (T_s + T_{IN}))}{e^{\frac{A_{SL} h_{SL} (1+R)}{r C_p R F}} + R - e^{\frac{h_s A_s}{r C_p R F}} (1+R)} \quad (2.45)$$

2.5.3 Limited validation

In this section we present a limited CFD validation of the results obtained in sections 2.5.1 and 2.5.2. The cases described in table 6 are used in the validation. Heat gains are inserted in the recirculation region using two vertical plates, as shown in figure 2.15.

Analysis of the average temperature in the recirculation proves difficult, since, the flow does not have a uniform temperature, and clear asymmetries are visible between the core of the recirculation region and the wall boundary layers. The temperature in the core of the recirculation region is influenced both by the wall boundary layer (temperature T_w) temperatures and by the part of the recirculation that is parallel to the jet (temperature T_R). Since the model does not predict the value of the temperature in the core region, it is misleading to compare average temperature in the

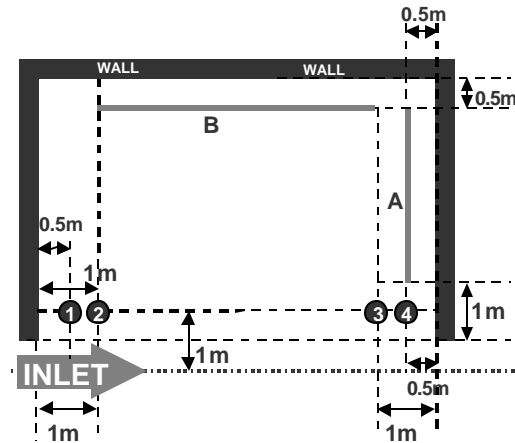


Figure 2.15

Location of the vertical plates used to introduce heat gains in the recirculation region.

The plates are located 0.2m above the room floor, are 0.2m high and have zero thickness. The internal gains are equally distributed in all faces of the plates (all faces had the same overall heat flux).

In order to estimate the temperature in the beginning of the entrainment and detrainment regions the temperature was averaged in points 1, 2, 3 and 4 in the figure, at heights 0.5 and 2.0m above floor. For the room with $L=9\text{m}$ points 2 and 4 were used. For the room with $L=4.5\text{m}$ points 1 and 3 were used.

Referring to the recirculation region coordinates shown in figure 2.7, points 1 and 2 are in the end of the recirculation region ($r=L_R$) and points 3 and 4 are in the beginning ($r=0$).

recirculation region as predicted by the model and the integrated average from the CFD simulation. In addition, these non-isothermal cases it is more difficult to define the boundaries of the recirculation and jet flow as result of increased spreading of the jet due to buoyancy effects. Instead we choose to compare a representative temperature in the beginning of the recirculation region and one in the end of the recirculation, just in the beginning of the shear layer (see locations in figure 2.15).

Table 2.6. Cases used in the preliminary validation of the recirculation zone temperature estimation for cases with no wall heat transfer and heat gains in the recirculation region.

| Case | Total Gains (W) | $F (m^3)$ | $L(m)$ | DT_R (CFD, °C) | | DT_R (CVR, °C) | | DT_{MX} (°C) |
|---------|--------------------|-----------|--------|------------------|-------|------------------|-------|----------------|
| | | | | $r=L_R$ | $r=0$ | $r=L_R$ | $r=0$ | |
| 14415G2 | 400 | 1.5 | 9.0 | 0.47 | 0.36 | 0.43 | 0.31 | 0.22 |
| 14415G4 | 800 | 1.5 | 9.0 | 0.94 | 0.75 | 0.85 | 0.63 | 0.44 |
| 14415G6 | 1200 | 1.5 | 9.0 | 1.29 | 0.94 | 1.28 | 0.94 | 0.67 |
| 14410G2 | 400 | 1.0 | 9.0 | 0.70 | 0.53 | 0.64 | 0.47 | 0.33 |
| 14410G4 | 800 | 1.0 | 9.0 | 1.22 | 0.92 | 1.28 | 0.94 | 0.67 |
| 14410G6 | 1200 | 1.0 | 9.0 | 1.61 | 1.20 | 1.92 | 1.41 | 1.00 |
| 14210G2 | 400 | 1.0 | 4.5 | 0.95 | 0.69 | 0.69 | 0.45 | 0.33 |
| 14210G4 | 800 | 1.0 | 4.5 | 1.86 | 1.46 | 1.96 | 1.48 | 0.66 |
| 14210G6 | 1200 | 1.0 | 4.5 | 2.35 | 2.04 | 2.94 | 2.23 | 1.00 |

Table 2.7. Cases used in the preliminary validation of the recirculation zone temperature estimation.. Q_{CFD} : total room heat transfer (surface plus internal gains) predicted using CFD. Q_{CVR} : total surface heat transfer predicted using the cross ventilation, recirculating flow model. Q_M : total surface heat transfer predicted using the fully mixed model. Error(%): percentage error of the two models when compared with the CFD predictions. The column labeled (C.6) refers to the value of the non-dimensional factor in expression 6 of appendix C.

| Case | Gains | DT (°C) | F (m³) | Q _{CFD} (W) | Q _{CVR} (W) | | Q _M (W) | |
|----------|-------|---------|--------|----------------------|----------------------|-----------|--------------------|-----------|
| | (W) | | | | | Error (%) | | Error (%) |
| 142T21G2 | 400 | 2.0 | 1.0 | 616.4 | 593.5 | -4 | 808.0 | 31 |
| 142T21G2 | 800 | 2.0 | 1.0 | 945.3 | 842.1 | -11 | 1117.3 | 18 |
| 142T41G2 | 400 | 4.0 | 1.0 | 1014.6 | 991.6 | -2 | 857.3 | 38 |
| 142T41G4 | 800 | 4.0 | 1.0 | 1370.5 | 1214.0 | -11 | 1699.0 | 24 |

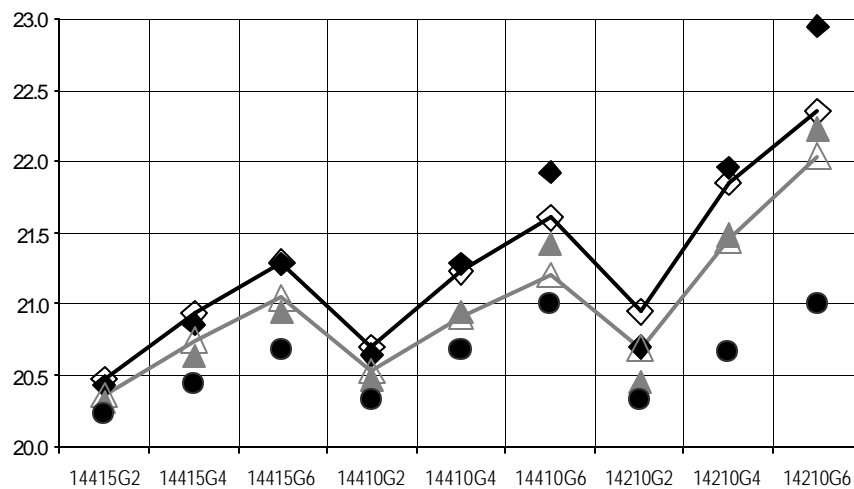


Figure 2.16

Comparison between CFD results and predicted recirculation region temperatures, obtained using the cross ventilation (case R) and the perfectly mixed model.

Black circles: predictions of the mixed model; Gray line: CFD results for the detrainment point (points 3 or 4); Black line: CFD results for the entrainment point (points 1 or 2). Gray triangles: prediction of the CV model for points 3 or 4; Black squares, prediction of the CV model for points 1 or 2.

The limited validation presented here indicates the following:

The recirculating flow model produces results with improved accuracy when compared with the perfectly mixed approach. Still, with higher internal gains (case 14210G6) the model over predicts the temperature increase in the recirculation region. This over prediction may be a consequence of the vertical movement of the inflow jet (as a result of strong negative buoyancy), as shown in figure 2.14. The short circuit effect that results from this vertical motion is not modeled.

The limited set of simulations performed for the case with both surface heat transfer and internal gains indicates that the model performs well, producing improved accuracy when compared with the perfectly mixed flow model. However, more extensive validation is required, including the analysis of the effects of variable inflow geometry, range of model applicability, internal gain location and type (point sources, large plates etc...).

2 - Conclusions

The global room heat transfer coefficient proved to be a useful analytic concept for the cases with simpler airflow pattern (perfectly mixed flow and CV case C), clearly displaying the reduction in heat transfer due to flow confinement effects. In flows of type R the coefficient has a complex expression and simple results are only possible in particular cases: full mixing between recirculation and jet flow and when using simplified shear layer heat transfer modeling. This simplification shows that, in this case shear layer heat transfer strongly influences the heat transfer process.

The results of the CFD validation show that the perfectly mixed approach is inadequate to model cross ventilation flows, resulting in systematic overestimation of overall heat transfer and failing to predict first order changes that are caused by variations in room aspect ratio. The new cross ventilation models results in improved accuracy in modeling of heat transfer in cross ventilation.

In the cases combining internal heat gains with surface heat transfer the validation is limited and further work is needed. The preliminary results indicate that the model is applicable in the combined cases used in the test and leads to improvements similar magnitude to the ones obtained in the case with no internal gains (as previously comparing with the perfectly mixed model).

3 - Multi zone ventilation: a momentum conservation correction for the aperture flow equation

Abstract

This chapter presents two contributions to simplified modeling of airborne pollutant removal in multi-zone cross-ventilated buildings, applicable on two scales: inter-room flows and in-room pollutant concentration. On the first scale we present an improved CV model, obtained by introducing a momentum conservation term in the equation that relates pressure variations to flow through apertures. On the room scale we present an analytical model to predict pollutant levels in two main regions: inlet jet flow and recirculation. The predictions of the model combining these two approaches are compared with CFD simulations of pollutant removal in a multi-zone building. The model retains most of the simplicity of current multi-zone, single node per zone models and can calculate the flow through offset outlet openings, correctly predicting the variation in the flow rates with offset geometry. The predicted airflow and pollutant removal rates display the sensitivity of pollutant concentration to building geometry.

Nomenclature

| | |
|-------------|--|
| A : | Aperture area (m^2). |
| A_r : | Room cross section area available for recirculation flow. |
| A_{IN} : | Inflow aperture area (m^2). |
| C : | Pollutant concentration (Kg/m^3). |
| C_D : | Discharge coefficient for flow through a sharp edged aperture. |
| F_{IN} : | Airflow rate (m^3/s). |
| m_S : | Strength of the pollutant source. |
| P_a : | Static air pressure (Pa). |
| P_{IN} : | Pressure before the aperture (Pa). |
| P_{OUT} : | Pressure after the aperture (Pa). |
| $V(x)$: | Maximum velocity of the jet (m/s). |
| V_L : | Velocity of the flow as it reaches the aperture A2 (see figure 1). |
| ρ : | Air density (Kg/m^3). |

3 Introduction

Currently available simple building airflow and pollutant removal models typically use the Bernoulli equation and a semi-empirical equation that relates pressure variations to flow through apertures (known as the aperture equation) in conjunction with mass and energy conservation principles [Feustel & Dieris, 1991]. Several building geometry features and their consequences are modeled: external pressure, internal/external aperture areas and heights, room volume and pollutant sources. Each building zone, or room, is modeled as a fully mixed volume using a single mathematical node.

In their present form, these models can be inaccurate when used to simulate rooms and buildings with multiple outlet configurations, producing both quantitative and qualitative errors. These problems can occur when there is significant conservation of inflow

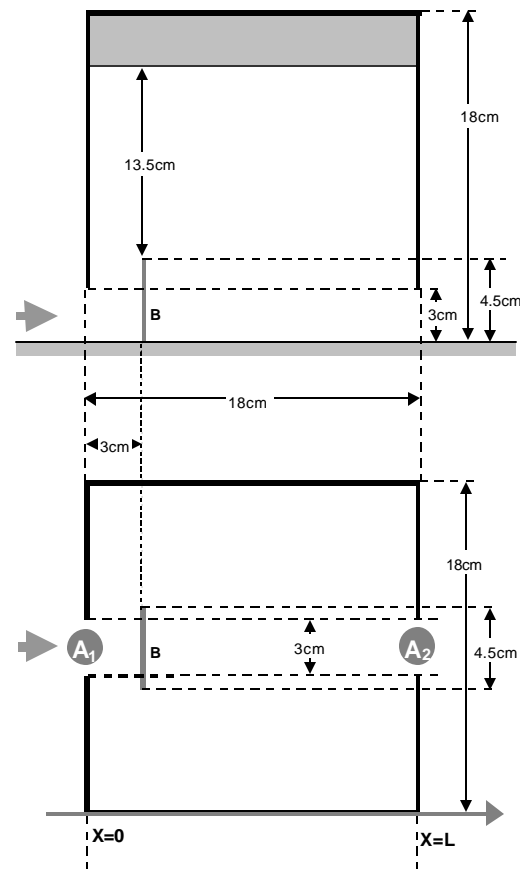


Figure 3.1

Schematic representation of the experimental setup used by Kato & Murakami.

momentum as the air goes through the building, a common flow characteristic in CV ventilation [Aynsley, 1999]. This is due to limitations of the aperture equation (see expression 3.1 below), developed mainly for simplified modeling of airflow in ducts with internal restrictions [Idelchik, 1986].

These limitations can be shown by comparing aperture equation airflow rate predictions with wind tunnel measurements or numerical solution of the Navier-Stokes equations [Kato *et al*, 1991, Murakami *et al.*, 1992]. Figure 3.1 shows the experimental setup used in both references. A scaled single zone building was tested with and without an internal obstruction (see *B* in figure 3.1) in front of the inflow opening. This obstruction is meant to diffuse inflow momentum. Still, the open area around obstacle is much larger than the area of the two apertures; therefore simulations using standard aperture equation models with two (A_1 , A_2) or

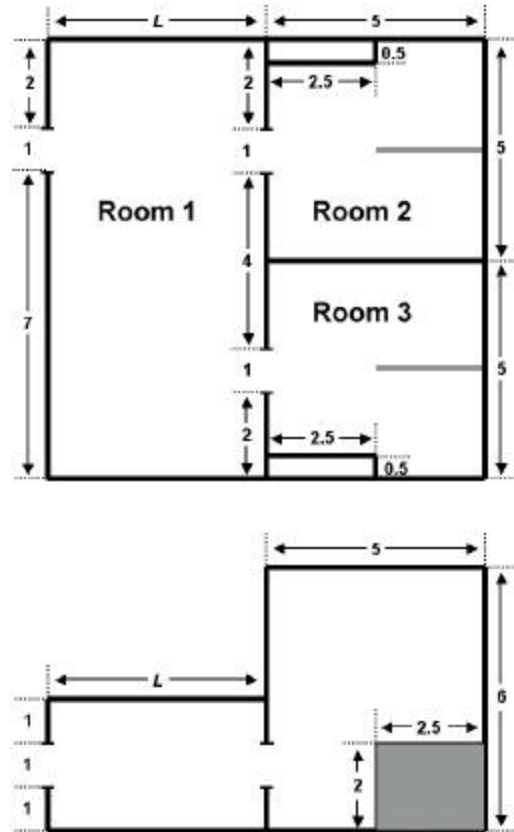


Figure 3.2

Geometry used to show momentum conservation effects in symmetric buoyancy driven case.

Air comes in through the opening on the left hand side and exits through the openings on the right hand side. A cross ventilation flow occurs, with air coming into room one and then to rooms two and three. Two cases were simulated using PHOENICS 3.3 with $k-\epsilon$ and equal, fixed heat flux vertical plates in each room (in gray in the figure). The only difference between the two cases is the length of the first room, L (3 or 6 meters).

three apertures (A_1 , A_2 and the aperture around obstacle B) produce similar results. In fact, a reduction of 14% in overall flow rate occurs due to the introduction of B in the flow path. Another case where momentum conservation is important is shown in figure 3.2. CFD simulations of this three room configuration show noticeable differences in flow rate through rooms 2 and 3. When $L=3$ (see figure 3.2) a 25% difference is found between the flow in rooms 2 and 3. When $L=6$ the difference is 10%. As in the previous case, a standard aperture equation based model fails to predict these differences.

In addition to this inaccuracy in multi-zone airflow predictions and resultant pollutant transport, the assumption of a fully mixed room leads to further modeling inaccuracy by neglecting significant internal gradients that can occur when internal pollutant sources are located in airflow recirculation zones. Recirculations occur whenever the inlet area is smaller than one half of the compartment cross-section area, a frequent geometric configuration [Carrilho da Graca & Linden, 2002].

This chapter presents two improvements to existing simple models that try to address the two problems described above. With this goal we will present:

An improved CV model, based on a momentum conservation correction for the equation that relates pressure loss to flow rate in sharp edged apertures.

An analytical model to predict pollutant levels in two main room airflow regions: inlet jet flow and recirculation.

The second model that will be presented is a development of the model developed in chapters 1 and 2 to non buoyant flows. The analytical model distinguishes zones in the flow in a similar approach to the common zonal models [Allard, 1992], but does not require iteration or introduce artificial pressure losses between the zones. We restrict attention to horizontal non-stratified flows and passive airborne contaminants or heat, ignoring buoyancy effects.

3.1 - The corrected aperture equation.

When air flows through an orifice with thin walls there are three main physical processes that lead to energy losses:

- 2 Flow contraction before the aperture: the trajectory of the fluid particles is altered making them flow towards the axis of the aperture, leading to flow contraction (flow through the aperture actually occurs through a smaller contracted area).
- 3 Friction losses in the aperture perimeter
- 4 Shear losses in the expanding jet.

In most buildings, the aperture diameter is much bigger than the wall thickness, and wall shear stresses are negligible in spite of having a fundamental impact on the flow by triggering the turbulent shear layers where most of the dissipation occurs. Further, shear layer losses are much bigger than flow contraction induced losses.

If the flow occupies a large cross section both before and after the aperture, the pressure loss due to the flow through the aperture is given by [Etheridge & Sandberg, 1996]:

$$F = C_D A_{IN} \sqrt{\frac{2(P_{IN} - P_{OUT})}{\rho}} , \quad (3.1)$$

The discharge coefficient C_D is obtained experimentally by measuring the pressure losses for a given flow through the aperture. When the flow through the aperture is turbulent, the typical case in building ventilation, the discharge coefficient is independent of the Reynolds number. For thin edged apertures it varies from 0.6 to 0.7. An analytic solution exists for two-dimensional flow through an aperture, leading to: $C_D=0.62$ [Etheridge & Sandberg, 1996]. In the validation cases presented below the flow rate is imposed, making the results independent of C_D .

The aperture equation (3.1) is used in all the multi-zone flow simulation software tools independently of whether the flow has significant momentum/kinetic energy as it reaches an aperture. This happens whenever air flows unobstructed across a room (after passing through the inlet). In the case shown in figure 3.1, when the flow reaches aperture A_2 the effects of flow contraction and organization due to passage in aperture A_1 can be important whenever the apertures face each other and are sufficiently close.

Jets flowing free from the action of external forces (gravity, surface drag) conserve their initial momentum flux and at a sufficient distance from the inlet will have an approximately self similar velocity profile so that the kinetic energy flux is given by the product of the maximum amplitude of the jet times the momentum flux.

The maximum amplitude of the jet starts to decay like x^{-1} at approximately four jet characteristic diameters (given by $A_{IN}^{1/2}$) from the inlet and the self similar profile occurs after approximately ten diameters [Malmstrom et al., 1997]. Whenever the room smallest room dimension is not one order of magnitude larger than the jet's characteristic diameter, confinement effects are clearly visible in the jet flow (as discussed in chapter 1). When modeling jet behavior in the present model we will not consider confinement effects, in addition the “bell” shaped velocity profiles at the apertures are replaced by a simpler square shaped profile. As will be shown below the accuracy of the model is adequate in spite of these approximations. Clearly confinement effects influence the rate of decay of jet velocity (one of the inputs from the model developed below), in particular reduce this rate, therefore ignoring these effects can be considered a conservative approximation.

After passing through the aperture the flow contracts (within one characteristic diameter [Idelchik, 1986]), flowing through a smaller area (given by $A_{IN} \cdot C_D$), the average inflow velocity is evaluated in this point and is given by:

$$V_{IN} = \frac{F_{IN}}{A_{IN} C_D} , \quad (3.2)$$

The velocity at a distance x , perpendicular to the inflow plane is then given by:

$$V(x) = V_{IN} \cdot f(x), f(x) = \begin{cases} 1 & , x < 4\sqrt{A_{IN}} \\ \frac{1}{x} & , x \geq 4\sqrt{A_{IN}} \end{cases} , \quad (3.3)$$

When evaluating the pressure available to drive the flow through an aperture (A_2) that is preceded by an aperture (A_1) the aperture equation can then be corrected by adding a kinetic energy term to the static pressure ($P_s(L)$), obtaining the dynamic pressure ($P_D(L)$) at a distance L from the previous aperture (see figure 3.1), given by:

$$P(L) = P_s(L) + \frac{\mathbf{r} \cdot V^2(L)}{2} , \quad (3.4)$$

Whenever aperture two (A_2 in figure 3.1) is bigger than A_1 , simple use of correction (3.4) could result in violation of energy conservation. Imposing conservation of the kinetic energy flux through the apertures so that, at best, we can have the same kinetic energy flux through both apertures, we obtain:

$$\int_{A_1} \mathbf{r} V_{IN}^3 dA = \int_{A_2} \mathbf{r} V_{MAX}(L)^3 dA \Rightarrow V_{MAX}(L) = \frac{A_1}{A_2} V_{IN} , \quad (3.5)$$

The first term in 3.5 is the inflow kinetic energy flux, the term on the right hand side is the energy flux through the outlet aperture (at best it can be equal to the inflow flux). The corrected aperture equation is then:

$$F = C_D A_2 \sqrt{\frac{2 \left(P_{IN} + \text{Min} \left(\sqrt[3]{\left(\frac{A_1}{A_2} \right)^2}, 1 \right) \mathbf{r} \cdot V_L^2(x) / 2 \right) - P_{OUT}}{\mathbf{r}}} , \quad (3.6)$$

In order to estimate this velocity in the multi-room flow configurations presented below it is necessary to determine if the aperture is in line with flow exiting the previous aperture and also account for the decay in the jet velocity. Clearly, if the model is successful it requires trading improved accuracy and feedback for increased computational effort and complexity. The factor A_1/A_2 in (3.6) results from imposing kinetic energy conservation. In the calculations presented below, (3.2) is used to calculate the flow rate through aperture 2, while (3.1) is used for all other apertures (solutions labeled –CA in figures 3.3-3.5). A solution using (3.1) for all apertures was also implemented, for comparison purposes (label –A in figures 3.3-3.5).

3.2 - Application to simplified model for pollutant concentration variations in cross-ventilated rooms.

In a fully mixed room model mass conservation leads to the following relation between flow and source strength:

$$F.C = m_s \Leftrightarrow C = \frac{m_s}{F} . \quad (3.7)$$

Figure 3.3 shows three locations where the pollutant concentration levels will be calculated in the improved simple model in the recirculation flow when it is re-entrained

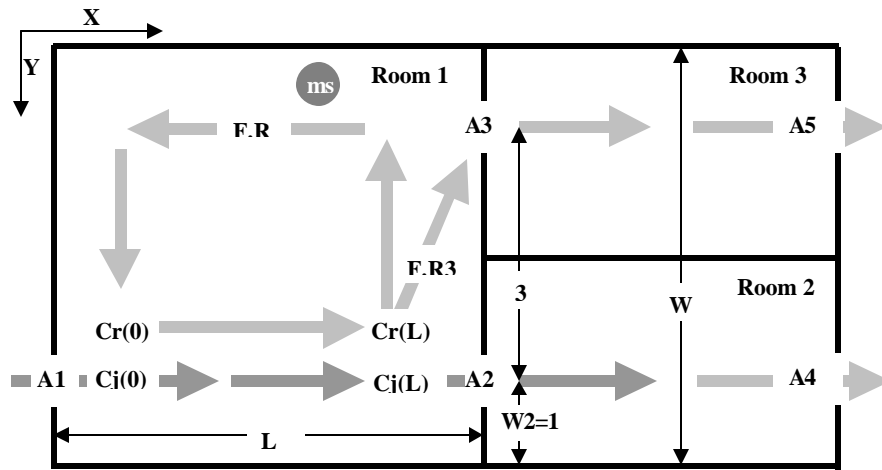


Figure 3.3

Schematic top view of the geometry of the multi-zone building studied.

The building height is equal to 2.25m. In the case with $L=9\text{m}$, $W2=2.5\text{m}$, approximately 5×10^4 grid points were used in the simulations. A contaminant source of strength one ($m_s=1\text{Kg/s}$), was placed in the recirculation region of room 1, in the region marked m_s in the figure. An inflow rate of $1\text{m}^3/\text{s}$ was imposed in aperture A1.

into the inlet jet flow ($Cr(0)$), in the inlet jet as it reaches A_2 ($Cj(L)$) and at the beginning of the recirculation ($Cr(L)$), considered equal to the concentration of the air that flows into room 3). The mixing between the jet and recirculation flows is estimated by considering that the interface between these two streams is a self-similar shear layer [Bejan, 1994]. It is considered that each stream changes temperature uniformly, a necessary approximation due to the finite volumetric flow rate of both streams.

The ratio ($R3$) between inlet flow rate and flow rate into room 3 is obtained using the corrected aperture equation model. The nondimensional ratio R is obtained by subtracting the flow rate $R3.F$ to the recirculation flow rate correlation formula [Carrilho da Graca & Linden, 2002]:

$$R = 0.14 \sqrt{\frac{L.A_r}{A1^{3/2}}} - R3 \quad , \quad (3.8)$$

In order to obtain the three concentration values the following system of equations is solved analytically (using $s=12$ and $2 \cdot \sqrt{A1}$ as an approximation to the mixing perimeter)

$$\left\{ \begin{array}{l} \frac{\partial Cj(x)}{\partial x} = \frac{V_0 \cdot 2 \cdot \sqrt{A1}}{F \cdot 4 \cdot s \cdot \sqrt{p}} \cdot (Cr(x) - Cj(x)) \\ \frac{\partial Cr(x)}{\partial x} = - \frac{V_0 \cdot 2 \cdot \sqrt{A1}}{F \cdot R \cdot 4 \cdot s \cdot \sqrt{p}} \cdot (Cr(x) - Cj(x)) \\ (1 - R3) \cdot Cj(L) + R3 \cdot Cr(L) - ms/F = 0 \\ F \cdot (Cr(0) - Cr(L)) - ms/F + r3 \cdot Cr(L) = 0 \end{array} \right. \quad (3.9)$$

The first and second equation model the pollutant exchange in the shear layer that forms the edge of the inflow. The third and fourth equations are pollutant conservation statements for the jet and recirculation regions in zone 1.

3.3 - Model validation

The method used is a combination of simplified solution of the Navier-Stokes equations, experimental correlations and CFD simulations. The theoretical basis of the models will be developed below and limited validation by comparison with a set of cross-ventilation, multi-zone pollutant removal CFD simulations will be presented.

The model is intended to produce first order accuracy and display the system features that dominate the pollutant removal process. In this context, the use of a simple turbulence model in the CFD simulations presented below is considered acceptable, under the verified assumption that the increased numerical load due to

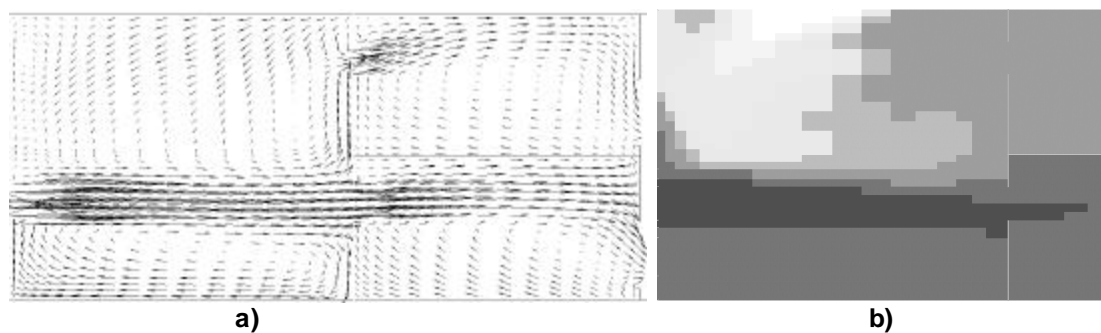


Figure 3.4

Top view of the CFD solution field for case 4. a) Flow field in the three rooms, b) Concentration field (dark gray representing lower pollutant concentrations).

the use of a low Reynolds number near wall approach is not needed because the influence of surface boundary layers in multi-zone flow rate prediction is small. The CFD simulations were performed using PHOENICS version 3.3 [PHOENICS, 2000]. Figure 3.3 shows a top view of the system geometries considered in this analysis. The arrows show the possible flow paths in the system. Three square aperture sizes were used, in conjugation with two room sizes. All the apertures were placed at equal distance from the floor and ceiling. The system geometry can be scaled with characteristic inlet dimensions (given by the square root of the aperture area). In addition, the flow rates and the pollutant concentrations scale linearly with the inlet flow rate and source strength, respectively. The cases analyzed are shown in table 1.

Table 3.1. *Geometric characteristics of the cases analyzed. Length in meters and areas in square meters.*

| CASE | L (m) | A1 (m2) | A2 (m2) | A3 (m2) | A4 (m2) | A5 (m2) |
|------|-------|---------|---------|---------|---------|---------|
| 1 | 6 | 0.5 | 1 | 1 | 2 | 2 |
| 2 | 6 | 0.5 | 0.5 | 0.5 | 2 | 2 |
| 3 | 9 | 0.5 | 0.5 | 0.5 | 2 | 2 |
| 4 | 6 | 1 | 1 | 1 | 2 | 2 |
| 5 | 6 | 1 | 1 | 2 | 2 | 2 |
| 6 | 6 | 1 | 0.5 | 1 | 2 | 2 |
| 7 | 6 | 1 | 0.5 | 2 | 2 | 2 |
| 8 | 6 | 1 | 0.5 | 0.5 | 2 | 2 |
| 9 | 6 | 2 | 2 | 2 | 2 | 2 |
| 10 | 9 | 2 | 2 | 2 | 2 | 2 |

Figure 3.4. shows a top view of the CFD airflow and pollutant concentration fields for case 2 (see table 1). The results in this case are representative of the results obtained in all other cases. These figures display the two flow features that we will model: significant momentum conservation, resulting in increased flow rate in room 3

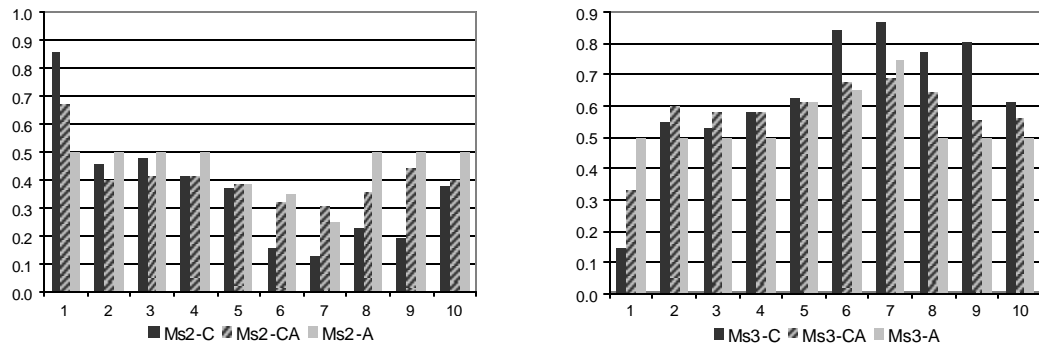


Figure 3.5

Flow rate though apertures 2 and 3 for the ten cases analyzed.

Black: CFD (label C), stripes corrected model (label CA), light gray simple model (label A).

and high pollutant concentration in the recirculation region of room 1, where the source is located.

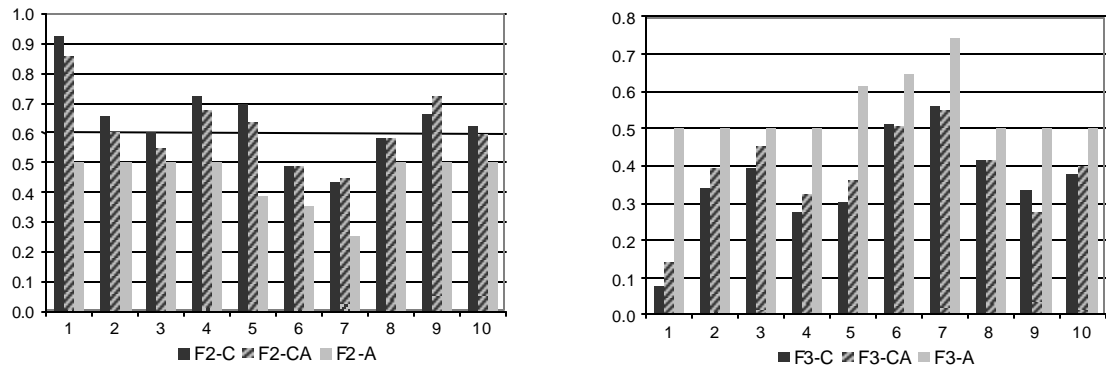


Figure 3.6

Total contaminant flux, rooms 2 and 3. $Ms_2 = F_2.C_j(L)$, $Ms_3 = F.R_3.Cr(L) = F_3.Cr(L)$.

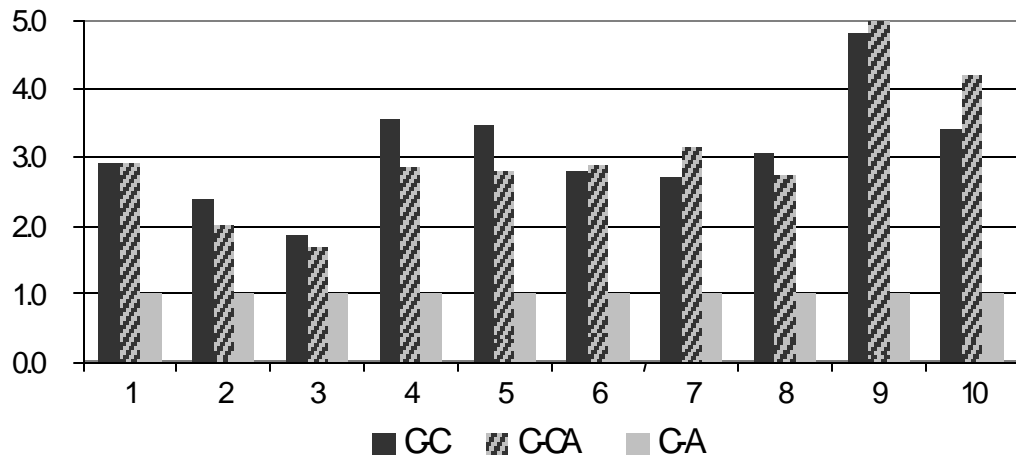


Figure 3.7

Average concentration in the recirculation region of room 1.

Prediction of improved model (-CA) given by: $Cr(0)$. Because the ratio between flow rate and contaminant source is one, existing simple models (label -C) predict a mixed concentration equal to one.

3.4 - Analysis

The comparison of flow rate predictions presented in figure 3.3 shows that the model is meets the first order accuracy goal. The results of the corrected model (gray and black) are in close agreement with the CFD- $k\epsilon$ simulations, with considerably less computational effort (the most clear example is case 1 in figure 3.3). As expected, flow rates through room 3 are smaller than through room 2.

The model clearly displays the negligible flow rate increase that results from increasing the size of A3, on the flow through A2 into room 2 (see cases: 4&5 and cases: 6&7 in figure 3.3). The flow rate predictions presented in figure 3.3 also represent the contaminant flows into rooms 2 and 3 whenever the dominant contaminant source is the inflow through aperture 1 or a source located in front of the inlet.

The predictions of contaminant fluxes when the source is placed in the recirculation region (point “ms” in figure 3.1) are shown in figure 3.4. The results are worse than in figure 3.3, which is due to the fortunate coincidence of higher flow rates and lower concentration that the existing simple model (gray in the figure) predicts for these cases. Even so, the results of the improved model are generally better. Figure 3.5 shows the value of the average pollutant concentration in the recirculation zone. As expected, the recirculation causes significant pollutant accumulation. The improved model is successful in predicting the effects of variations in room geometry in the concentration levels with first order accuracy .

3 - Conclusions

The validation of this improved simple model indicates that the dominant physical processes in the system are modeled within the first order accuracy goal.

The improved model retains the simplicity of current multi-zone, single node per zone, models while providing increased feedback on the impact of variations in room and building geometry. The model can be implemented as a refinement on existing simplified software models. In particular, the model calculates the flow through offset openings, and accurately predicts the variation in the flow with offset geometry providing a simple way to estimate pollutant removal efficiency.

4 - A simple model for heat transfer in displacement-ventilation.

This chapter presents a simple model for vertical temperature profile and heat transfer prediction in displacement ventilation. The fully-mixed room air approximation that is currently used in most whole building analysis tools is extended to a three node approach, with the purpose of obtaining a first order accuracy model for displacement ventilation systems. The use of three nodes allows for improved prediction of thermal comfort and overall building energy performance in low energy cooling strategies that make use of unmixed stratified ventilation flows.

The simplified airflow model was developed using a combination of scaled model experiments and scaling analysis. This combined approach gives insights into the mechanisms and system parameters that control the airflow pattern and the vertical temperature variations.

The model is implemented in the building thermal analysis software tool *EnergyPlus*. The implementation uses an embedded three-node structure with minimal changes to the existing code structure based on a single air node per room. Examples of the impact of using the displacement ventilation model in *EnergyPlus* are presented with emphasis on low energy cooling systems. When compared with previously available single node mixed flow models, improved quantification of the total heat transfer between ventilation air and building surfaces is achieved and noticeable temperature differences are present in the predictions.

Nomenclature

| | |
|-------------|--|
| A_{Cn} : | Ceiling surface area (m^2) |
| A_{Fn} : | Floor surface area (m^2) |
| A_{LLn} : | Area of the lateral surface that exposed to the lower zone (m^2) |
| A_{LUn} : | Area of the lateral surface that exposed to the upper zone (m^2) |
| B : | Plume buoyancy flux |
| b : | Width of a fully developed plume (m) |
| C_p : | Thermal capacity of air at constant pressure ($W\ m^3/(Kg\ K)$) |
| F : | Inlet flow rate (m^3/s). |
| FRg : | Fraction of the room convective gains that are mixed into the occupied zone |
| g : | Acceleration of gravity (N/Kg) |
| G : | Convective internal gains (W). |
| H : | Room height (m) |
| h : | Height of the interface between lower and upper layers (m) |
| h_{Cn} : | Ceiling surface heat transfer coefficient ($W/(m\ K)$) |
| h_{Fn} : | Floor surface heat transfer coefficient ($W/(m\ K)$) |
| h_{Lun} : | Lateral surface exposed to the upper zone heat transfer coefficient ($W/(m\ K)$) |
| h_{LLn} : | Lateral surface exposed to the lower zone heat transfer coefficient ($W/(m\ K)$) |
| M : | Vertical plume mass flow rate (m^3/s) |
| n : | Number of plumes in the room |
| T : | Temperature ($^{\circ}C$) |
| T_{CMF} : | Comfort temperature in the room ($^{\circ}C$) |

| | |
|---------------|---|
| T_{Cn} : | Temperature of the nth ceiling surface (°C) |
| T_{CS} : | Average temperature of the room ceiling (°C) |
| T_{Fn} : | Temperature of the nth floor surface (°C) |
| T_{FS} : | Average temperature of the room floor (°C) |
| T_{FLOOR} : | Temperature of the room air in the horizontal layer adjacent to the room floor |
| T_{IN} : | Temperature of the inflow air (°C) |
| T_{LD} : | Average temperature of the room lateral surfaces that are below h (°C) |
| T_{LLn} : | Temperature of the nth lateral surface that is below the mixed layer (°C) |
| T_{LU} : | Average temperature of the room lateral surfaces that are above h (°C) |
| T_{LUn} : | Temperature of the nth lateral surface that is above the mixed layer (°C) |
| T_{MX} : | Temperature of the room air in the upper mixed layer (°C) |
| T_{OC} : | Temperature of the room air in the occupied zone (°C) |
| T_{OUT} : | Outside air temperature (°C) |
| T_{SN} : | Temperature obtained using the single, perfectly mixed, node model (°C) |
| W : | heat flux plume (W) |
| a : | Plume entrainment constant, considering top hat plumes (measured experimentally, $\alpha=0.13$). |
| b : | $1/T$ for and ideal gas Coefficient of thermal expansion (K^{-1}) |
| r : | Air density (Kg/m^3) |

4 - Introduction

Displacement ventilation (DV) systems take advantage of the temperature stratification that is formed in a room. Air, warmed by the heat sources, moves vertically and accumulates near the top of the room where it is exhausted. In order to minimize mixing of this layer of warm air down into the occupied zone, inflow areas are sized and positioned so that low velocity inflow occurs close to the floor. In displacement systems, the dominant temperature gradient is vertical and airflow velocities are small in the whole room. In most situations where the room internal gains occur predominantly in the form of plumes, a noticeable interface occurs between the occupied zone of the room and a mixed hot layer near the ceiling of the room. Maintaining the lower boundary of this warm layer above the occupied zone is one of the many unique challenges of displacement ventilation design. Figure 4.1 shows an image of laboratory scaled experiment of a displacement ventilation flow, the lower interface of the mixed layer is clearly visible [from Cooper & Linden, 1996]. Measurements in a full scale environmental chamber also display the clear transition between layers shown in figure 4.1 [Dominique & Guitton, 1997].

Because air is admitted at low level into the occupied zone (considered here to

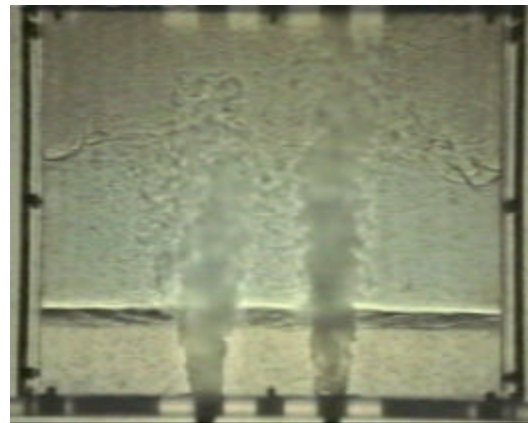


Figure 4.1

Image of a laboratory scaled displacement ventilation flow.

The flow is driven by two equal plumes whose buoyancy source is water with a higher salt concentration. Above the horizontal line visible in the figure a highly mixed region occurs.

extend between the floor and 2 m in height) the inflow temperature must be higher than in conventional mixing systems, avoiding cold draft discomfort. As will be discussed below, interaction between heat sources, furniture and wall driven flows promote a certain degree of mixing in the occupied zone, directly convecting a fraction of the internal gains into this zone.

The need for reduced inflow velocities often limits the maximum inflow rate that can be used in a given room. This, in conjunction with the higher inflow temperature results in a limitation on the maximum heat load that can be removed from the occupied zone by displacement systems to approximately 50W/m^2 . In contrast, heat loads in higher levels of the room (above the occupied zone) are removed in an ideal way by displacement flows, having no impact in the conditions of the occupied zone (except for convection induced by radiative heat transfer). Displacement ventilation is not adequate to handle high heating loads. When the inflow air is warmer than room air, short circuit can occur with the inflow air flowing almost unaffected into the outlet. In addition, the descending wall boundary layer flow that is formed whenever the room envelope is colder than the occupied zone disrupts the stratification by bringing air from the upper warmer layer into the occupied zone.

Displacement can be a better choice than mixing ventilation whenever a vertically stratified, stable temperature gradient can be established in the room. In these cases improved air quality can be obtained (limited only by the quality of the inflow air) as well as reduced energy consumption. These advantages result mainly from two factors:

- I - Reduced diffusion in the inflow. Since mixing is not promoted, the pressure drops across the typically large inflow apertures are small when compared with

mixing ventilation (where much smaller apertures with higher inflow velocities are used). Another positive consequence of decreased mixing is an improvement in air quality, as air from different pollutant sources does not mix in the occupied zone.

II - Increased inflow temperature. Whenever cooling is required in mild outside conditions, such as in most modern office buildings, the use of higher inflow temperature (typically 19°C, instead of 15°C) allows for more hours of free cooling (using direct outside air). Whenever the outside air temperature is above 19°C this advantage is mostly lost: the internal loads must be removed from the space independently of the airflow pattern (during the warmer hours buildings tend to be almost closed to the outside, operating in closed loop). The inflow temperature advantage is then only useful for the minimum outside air that must always be provided (in most cases this remaining advantage is negligible).

Naturally promoted displacement ventilation is a low energy cooling technique with a great potential. As a result of the vertical stratification, heat loads are handled in an optimal way, and, as will be shown below, the ability to obtain comfortable conditions using higher inflow temperatures, mean that acceptable comfort conditions can be obtained for higher outside temperatures. One of the challenges when using naturally driven displacement flows is to maintain the vertical temperature profile in adverse conditions such as opposing wind generated positive pressure at the outlet [Hunt & Linden, 2001], or high outside temperatures that, in conjunction with internal exposed high thermal mass surfaces (a common low energy cooling strategy) may result in

reverse stack with inflow at high level during the warmest hours of the day. One way of stabilizing the stack and controlling the airflow to desired levels is to use solar chimneys or, tall, well insulated, spaces.

Aim of the model and its implementation

The main goal in DV modeling is to predict the vertical temperature gradient in the room. This seemingly simple task is difficult as many flow and room geometry features contribute to form the stratification: room height, airflow rate and temperature, type, location and strength of the buoyancy sources. Prediction of this gradient allows for fine tuning of system design and sizing as well as more accurate predictions of energy consumption and thermal comfort.

Environmental chamber and scaled model experiments [Rees & Haves (2001), Linden et al. (1990)] of displacement ventilation systems reveal temperature profiles, or density profiles, with a smooth transition between the lowest temperature (close to the floor) and the bottom of the mixed upper layer. This smooth transition is the result of non-adiabatic walls and of the action of many buoyancy sources with different shapes and strengths, located at different heights, a situation also observed in scaled model experiments, but, in most cases not suitable for exact analytical solution [Cooper & Linden (1996), Linden & Cooper (1996)]. The many factors influencing the gradient make for a complex modeling task. A simple for this problem is only possible in some cases, clearly, restrictions in model applicability must be specified, identifying a set of cases where the dominant flow features can be modeled.

Even in a simplified modeling approach of the problem, there is a need to consider many room geometry and flow features. In addition, designers are often faced with the

task of simulating multiple rooms, occupation and outside weather scenarios. For this reason the implementation of the model in a whole building thermal simulation software tool (presented in chapter 5) is fundamental to its usability.

4.1 – Review of displacement ventilation

Currently there are four main types of models for displacement ventilation: computational fluid dynamics (CFD), experimentally based semi-empirical models, plume equation based multilayer models, and nodal models.

The use of CFD (typically using Reynolds averaged turbulence models) requires extensive expertise and time, further, in many design situations, the need to analyze multi-room ventilation geometries using weather data spanning several days or months makes CFD impractical and simpler ventilation models more practical. Often the building geometry and internal furniture elements are not fully defined, making simple modeling approaches and results more realistic than detailed flow field simulations. In a review of turbulence models for prediction of room airflow [Nielsen, 1998] discusses the application of turbulence models of varying complexity to displacement flows and exposes limitations of the standard $k-\epsilon$ model and also a zero equation model when dealing with flows that have regions with low velocity, stagnant flow. In these cases, it is clearly shown that the $K-\epsilon$ model performs better when modified with near wall damping functions and that zero equation models cannot capture all flow characteristics using a single constant ratio between the product of the flow characteristic velocity and dimension and the equivalent turbulent viscosity. However, reasonable accuracy can be expected when CFD simulations are run by expert users, particularly for cases where the internal gains are

known, and imposed as boundary condition on the simulation. Good agreement was found by [Cook & Lomas (1998)] when reproducing scaled model, plume in a box displacement ventilation flow experiments [Linden et al. (1990)], using the $k\epsilon$ model. Good agreement was also found when comparing CFD simulations and test chamber measurements [Rees et al. (2001)] (also using the $k\epsilon$ model). In the cases where surface heat transfer is important in the flow (displacement ventilation with chilled ceilings, floors or other important thermally active internal surfaces) the use of the standard $k\epsilon$ model is inadvisable as significant overestimation in heat transfer can occur. In these cases the standard wall functions are not appropriate and a low Reynolds number near wall approach is more appropriate [Awbi, 1998].

The Nodal model approach simulates displacement ventilation airflow by dividing the room into zones (both vertically and horizontally) represented by nodes [Rees & Haves (2001)]. Air movement between the nodes is modeled using pre-calculated airflow rates (obtained experimentally and by running CFD). Energy conservation is imposed on the different nodes, and the model is then solved numerically, resulting in a prediction of the vertical temperature profile and of the energy exchanges between the nodes. This approach, while successful in predicting the flow and temperature field for geometries similar to those used when developing the model, can suffer from lack of flexibility and clarity in the modeling approximations. When dealing with diverse geometries it is not clear that the flow coefficients are applicable or why they can be used since plumes, the fundamental driving mechanisms of the displacement flow, are not explicitly modeled. This is the main difference between these models and the model that will be developed below.

Experimentally based semi-empirical models provide a valuable tool for simple design assessment of displacement ventilation systems [Mundt (1996), Skistad et al. (2002)]. The simplicity and clarity in the approximations used are a positive aspect. Because the correlations are obtained for particular geometries they lack flexibility to handle variable room geometries, in addition, the existence of the vertically superimposed mixed layers is not considered.

Plume equation based multi-layer models take a more radical approach to the problem by modeling only the fundamental driving mechanism: plume flow [Morton et al. (1956), Baines & Turner (1968), Linden et al. (1990)]. For the simplest cases of one or two plumes in a room with adiabatic walls an analytical solution is possible. In this idealized case the model is accurate, simple to use and clearly displays the governing physics of the problem. The applicability of these models is limited whenever wall-driven natural convection is stronger than plume convection (in some of these cases a clearly defined displacement flow may not exist). Configurations with strong interactions between wall boundary layer flows and multiple plumes are not suitable for analytical solution.

From a fundamental point of view, the first three approaches mentioned fail to provide substantial insight into the mechanisms and system parameters that control displacement ventilation airflow. Nodal and semi-empirical models, while providing reasonable accuracy fail to represent or account for the controlling mechanisms in the physical system. While this may not be a problem in some engineering applications it limits model extension possibilities (increased accuracy and more diverse geometries). Since the fundamental physics is not explicitly considered increased versatility can only

be achieved by adding more complexity (a greater number of distinct correlations or a greater database of inter node mass flow coefficients).

The main strength of the fourth approach mentioned is the ability to identify and model the fundamental physics of the problem. Currently, numerical solution methods based on this approach are not available in a design tool. The model discussed below is an extension of this approach, trying to overcome some of its limitations and increase its applicability to more “real world” cases by providing a software tool implementation. When extending the model we tried to achieve optimal balance between modeling clarity and simplicity and modeling accuracy . The software implementation of the model is a fundamental step to making it usable in the more complex and common situations (multiple plumes in non adiabatic rooms).

4.1.1 - Single plume two layer model

The simplest form of plume equation based models applies to the case of a single plume in an adiabatic box with constant ventilation flow (steady state conditions). For this configuration two density layers form in the room: a lower layer with similar density / temperature as the inflow air and a mixed upper volume with the same density / temperature as the outflow air. The main assumption of this model, validated against scaled model experiments [Linden *et al.* (1990)], is that the interface between the two layers occurs at the height (h) where the vertical buoyancy driven plume flow rate is the same as the inflow rate. For a point source of buoyancy in a non stratified environment (a plume) the airflow rate increases with vertical distance from the source according to:

$$M = \frac{6}{5} a^{4/3} \sqrt[3]{\frac{9}{10} p^{2/3} B z^5}, \quad (4.1)$$

For an ideal gas in adiabatic conditions, the relation between variations in density and temperature is approximately given by:

$$Dr = r DT b, \quad (4.2)$$

resulting in the following relation between heat and buoyancy flux:

$$B = \frac{g b W}{r C_p}. \quad (4.3)$$

Because plume vertical flow rate increases with height, with exponent 5/3 (4.1), for any inflow rate in a room, there is always a height (h) where plume driven flow rate matches the inflow rate. The height, h , where this match occurs is obtained by setting (4.1) equal to F :

$$h = \sqrt[5]{\frac{5^4 F^3}{4 \times 3^5 a^{4/5} B p^2}} . \quad (4.4)$$

Above this “matching” height additional air entrained into the plume must be recirculated from higher levels in the room. This recirculation process results in a warm upper layer with a uniform temperature occurring at heights above h . When the ventilation flow rate becomes sufficiently large, or the buoyancy flux sufficiently small, h may be bigger than the room height H , in which case $h=H$ must be used. Introducing standard air properties at 20°C in (4.4):

$$h = 19.68 \sqrt[5]{\frac{F^3}{W}} \quad (4.5)$$

The height of the mixed layer is measured from the vertical location of the point buoyancy source. The dependence of h on the flow rate F (exponent (3/5)) is much stronger than on the plume heat flux W , exponent (1/5). Accurate prediction of h is important for displacement ventilation design: in this region the flow becomes mixed and the benefits of displacement ventilation are lost whenever h is within the occupied zone.

Simple analysis of (4.5) provides hints on the difficulties of maintaining a set of desired conditions in the occupied zone of a displacement ventilated room, such as:

average temperature, temperature gradient, and height of the mixed layer. When the heat flux in the plume increases by one order of magnitude, h is reduced by approximately one third. A similar reduction occurs when the flow rate is reduced to one half. In a first analysis it seems that this asymmetric variation can be useful to control displacement flows using a variable air volume, fixed inflow temperature system: relatively large variations in heat loads can easily be counteracted by flow rate variations. Unfortunately, as a result of energy conservation, the temperature in the occupied zone will decrease when trying to maintain a given h since this task requires unequal changes in F with W (contrary to the inverse, direct, relation that occurs in perfectly mixed systems). One way to address this problem is make adequate changes in the inflow temperature, but this requires a more complex climate control system. We continue this discussion with the multiple plume case, tending towards a physically based simple numerical model.

4.1.2 - Multiple plumes: n equal plumes

Multiple plume configurations present different modeling challenges depending on whether asymmetries in plume strength are present. In the case of multiple, equal strength plumes a straightforward extension of the single plume case is possible, but in the case of n unequal plumes n vertical layers are formed [Linden & Cooper, 1996]. Fortunately, while much more complex, this case remains suitable to simplified modeling as long as first order accuracy is considered acceptable.

For the case of multiple non coalescing plumes (n), with equal strength, the total vertical airflow for a given height is:

$$M = \sqrt[3]{n} \frac{6}{5} a^{4/3} \sqrt[3]{\frac{9}{10}} p^{2/3} \sqrt[3]{Bz^5} \quad (4.6)$$

Resulting in a mixed layer height of:

$$h = \frac{19.68}{\sqrt[5]{n}} \sqrt[5]{\frac{F^3}{W}} \quad (4.7)$$

The only difference between expressions 4.7 and 4.5 is the $n^{-1/5}$ multiplying factor. The exponent is much smaller than one, reflecting a dampened reaction of the mixed layer height to changes in the number of plumes. The mixed layer height will decrease by 20% when two plumes added to a room with a single plume (all plumes are equal) and by 40% when twelve plumes are added.

4.1.3 - Multiple plumes: n unequal plumes

In the case of n plumes with different strength n vertical layers are formed creating a increasing modeling challenge, in the predictions and in the detail required (both in input and output). In light of the goals in the present work, the question that is important to ask is:

When can n variable strength plumes be modeled as n equal (average) strength plumes (using (4.7)).

The n equal plume case only has two layers, and all vertical temperature variations occur in the transition between first and second layer. In order for this simplification to be applicable it must be able to predict, with acceptable accuracy, the height of the layer where the most important temperature transition occurs. To answer this question we start by reviewing results for two and three asymmetric plumes in a room and then proceed to the case of one strong plume in a space with n smaller equal strength plumes.

In the case of two separated plumes with different strength (B_1, B_2), three layers are formed. The concept of a matching height, mentioned above, is still applicable to obtain the height of each layer. The first layer is formed at the height (h_1) where the total upward flow rate from the two plumes is equal to the inflow rate. At this point, the weakest of the two plumes discharges, resulting in a first layer with average temperature approximately equal to the temperature of the weakest plume at the height h_1 . The stronger of the two plumes continues to flow upwards until it discharges into the upper layer, whose lower level occurs at the height (h_2) where the flow rate from the strongest plume matches the inflow rate.

In a more accurate analysis, the fact that the strongest plume entrains air at an intermediate temperature while it traverses the second layer has a small impact in the height and temperature of the third layer [Cooper & Linden, 1996]. As in previous cases, we ignore this small effect. When the weakest plume enters the second layer (where it discharges), it becomes a momentum jet, since it has, by then, acquired a non negligible momentum flux but has negligible buoyancy in the second layer. In most cases this plume has enough momentum so that it reaches the bottom of the third layer, promoting mixing between the layers. This phenomena contributes to the smooth (as opposed to

step like) vertical temperature gradients observed in most experiments (another flow component that can have similar effects are the wall boundary layers).

Multiple unequal plumes are the most common design scenario in office buildings. In this case, multiple layers are formed and the level of the lowest mixed layer is obtained by numerical solution of the equation:

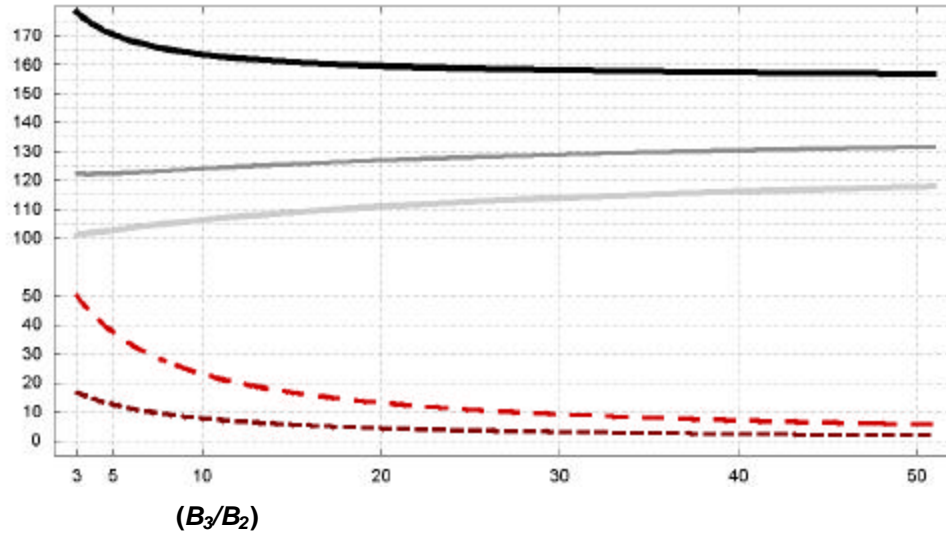
$$z^{5/3} \sum_n \frac{6}{5} a^{4/3} \sqrt[3]{\frac{9}{10} p^{2/3} \sqrt[3]{B_n}} = F \quad (4.8)$$

Multiple plume flow has one important property for the present purpose: at a given height z , the total flow rate produced by n plumes of equal strength is always higher than the flow produced by n plumes of unequal strength, whenever the total buoyancy flux of the two sets of plumes is the same. Since n equal plumes produce more flow, solving 4.8 to obtain the height of the mixed layer using n equal plumes always leads to a conservative estimation (given that a precise result is not appropriate, a systematically conservative estimation is a welcome characteristic). A conservative estimation is a welcome characteristic in a simple model as long as it is possible to know quantitatively how conservative is the model and in what situations. Given the complexity of the problem one cannot expect a simple answer. In order to analyze the problem a set of plots were produced providing a graphical image of the variation of the layer height for asymmetric plume configurations for three cases: two plumes (4.2 a)), three plumes (4.2 b)) and nine plumes (4.3).

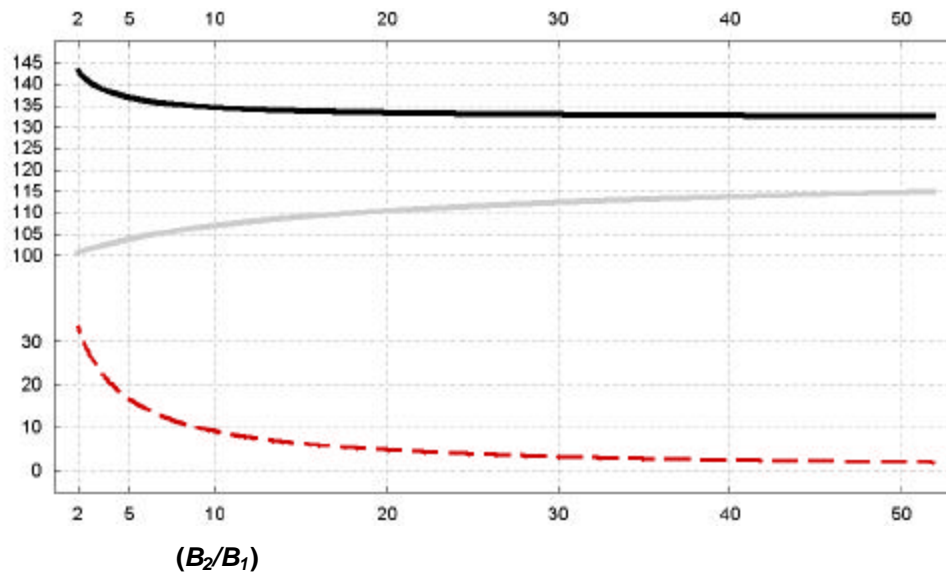
Since we are trying to evaluate the impact of using an n equal plume approach, all plots normalized using mixed layer height and temperatures predicted using this approach:

The mixed layer height for the different layers present in the flow is divided by the mixed layer height obtained with non coalescing plumes of equal strength and equal total buoyancy flux, such that, in the two plume case the average plume strength is calculated using: $B_{Average}+B_{Average}=B_1+B_2$, and in the three plume case: $B_{Average}+B_{Average}+B_{Average}=B_1+B_2+B_3$.

The fractional temperature increase (dashed lines in the plots) is divided by the temperature increase of the n equal plume case (this configuration has only one temperature change).



a)



b)

Figure 4.2

Percentage variation of the height of the mixed layers and temperature variation in asymmetric plume cases. In both plots, in red: percentage temperature increase between the layers (in a) between the first and second layer, in b) between the first and second and between second and third).

a) similar to plot a) but with three asymmetric plumes ($B_2=2.B_1$), on the horizontal axis the variable buoyancy flux ratio: B_3/B_2 .

b) two asymmetric plumes, on the horizontal axis the ratio between the buoyancy fluxes of the two plumes: B_2/B_1 . On the vertical, the height of each layer.

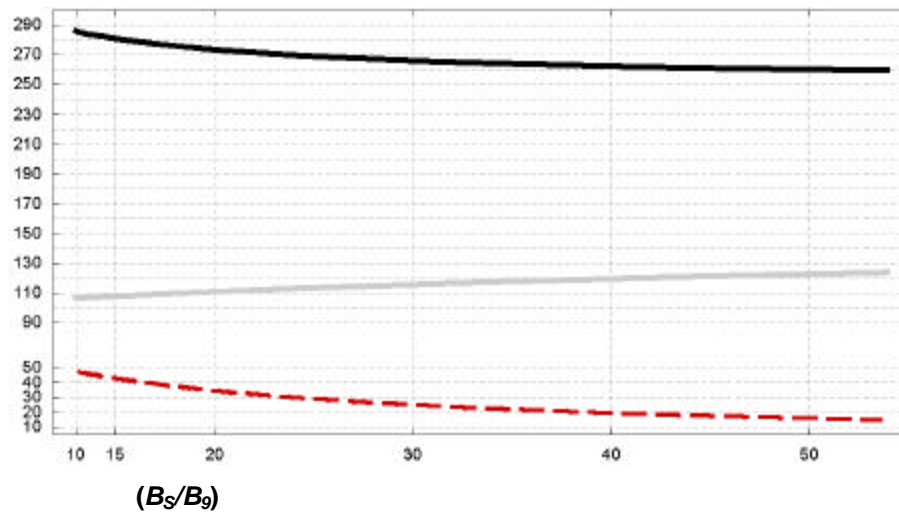


Figure 4.3

Percentage variation of the height of the mixed layers and temperature variation in a configuration with nine equal plumes (B_9) and a stronger plume with variable strength (B_S).

In red percentage temperature increase between the first and second layer.

On the horizontal axis the ratio between the buoyancy fluxes of the plumes: B_S/B_9 . On the vertical, the height of each layer, normalized by the height obtained with non coalescing plumes of equal strength with equal total buoyancy flux. Label axes

Figure 4.2 a) shows the variations in the height of the second and third layers as a function of plume strength asymmetry (on the horizontal axis B_2/B_1). The most striking fact about this chart is that the height of the first of the two mixed layers varies very little (less than 20%) as the plume strength ratio varies from one to fifty. Using the equal plume approximation results in a small under estimation of the height of the first mixed layer. Analysis of the two extreme cases: the lowest ($B_2/B_1=2$) and highest buoyancy ratios shown in the figure provides greater insight into the consequences of the approximation:

In the highest case ($B_2/B_1=50$), the percentage temperature variation between the first and second layers (dashed line in the chart) is negligible. Therefore, the transition between first and second layers is not important and the temperature profile will only show a significant temperature transition between the second and third layers. This transition is located at a height that is 30% larger than the prediction obtained considering symmetric plumes. The model is very conservative in this extreme case.

In the case with ($B_2/B_1=2$) the first layer is at the same height as predicted by the symmetric plume solution. As before, a model supposing n equal plumes is conservative in the prediction of the temperature variation: a 100% relative increase in temperature is predicted, when in fact it is 33% with the full 100% increase occurring only at a height 42% above predicted.

Analysis of the case of three asymmetric plumes shown in figure 4.2 b) leads to similar conclusions: using the symmetric plume solution leads to underestimation of the mixed layer height and temperature transition. In this case the value of the overestimation increases.

Figure 4.3 shows a more extreme configuration: 9 equal plumes in the presence of a single, much stronger plume. This configuration can occur in an office with several workstations and a large size office appliance, such as a video wall. Analysis of the figure reveals that, as in the previous cases, the height of the first mixed layer shows little dependence on the strength of the strongest plume. Unfortunately this does not mean that the n equal plumes approach is adequate for this case: the red percentage temperature variation line in the figure reveals very high temperature differences between the third and second layers. In view of this it is clear that the approximation in the n equal plume case, predicting that the whole temperature increase (100%) occurs in

the second layer results in overestimation of this layers temperature (at this height) and will mislead designers, hiding the main point of these configurations: because the heat flux of the stronger plume rises to higher levels of the space it is possible to ignore its influence in the temperatures of the occupied zone whenever the height of the transition between the second and third layers formed is above the occupied zone (black line in the chart).

This analysis leads to the conclusion that using an n symmetric plume approach to treat unequal plume configurations leads to systematic underestimation of the mixed layer height and overestimation of the magnitude of the temperature transition between first and second layers. Both systematic errors introduced by this approximation are conservative. In the cases with several equal plumes in conjunction with a stronger single plume the model is clearly too conservative and the three-layer two-plume solution should be used. The two plumes that should be used in the model are: the strongest plume and a plume obtained by grouping all the equal weaker plumes into a single, stronger, plume. The model that is presented below always considers equal plumes.

4.2 – Theoretical basis for the chosen model representation

4.2.1 – Effects of wall heat transfer

The interaction between heat transfer from internal surfaces (positively and negatively buoyant) and the vertical displacement flows generated by the heat sources in the occupied zone must be considered because: when heat flux from lateral walls or floor in the lower layer is comparable to the fluxes from the internal sources the model is not applicable. In these cases the airflow pattern may not conform to displacement ventilation and using a mixing flow model may be more adequate. For this reason we will try to define simple criterion that indicate whether a displacement flow exists. In the cases where the flow is dominated by the plumes, the height of the mixed layer is determined solely by the total buoyancy flux from the internal sources and the ventilation airflow rate, using (4.7). Whenever the flow is not clearly dominated by the plumes the model will not be applicable and a perfectly mixed flow model is used.

In order to estimate the influence of internal surface driven flows there are several options, with varying detail:

- Compare the buoyancy flux from the internal plumes with the fluxes from the boundaries. This is the simplest way to evaluate buoyancy effects. As discussed

below it can be useful in the upper warm layer, where the mixed conditions greatly simplify this assessment.

- Compare the flows that are driven by the plumes in the lower layer with the surface induced buoyancy flows. This more complex comparison method may be useful for lateral wall driven flows. Since in the model developed below the only energy transporting flows considered are the point source plumes in the lower layer it is useful to compare the flow driven by the wall boundary layers with the plume flow.

4.2.1.1 - Heat transfer from the lateral surfaces

Scaled model experiments [Linden et al., 1990] show that in a room whose only buoyancy source is a lateral wall a smooth temperature gradient is created and no clear temperature transition or layers are visible. For positively buoyant wall driven flows that have a much smaller buoyancy flux than the flow driving plumes this smoothing effect can be expected to superimpose on the two layer structure, leading to a smoother temperature transition between the two layers.

When the wall driven boundary layer flows are negatively buoyant in the upper layer region an additional energy transfer path is created, with opposite direction to the plume driven flow considered in the model. In order to model these cases this additional, reversed energy and mass flow must be considered, greatly increasing modeling complexity. Cases where these flows have a magnitude that is comparable to the inflow

are not modeled by the present model. The model that will be developed below is not applicable when:

Downward moving buoyancy driven airflow rate is of the same order of magnitude as plume driven flow (these descending currents are typically generated on lateral surfaces or in the ceiling whenever these surfaces are much cooler than the room air).

Upward moving wall or floor generated buoyancy flux in the lower layer is of the same order or magnitude as plume driven flow.

In these two cases it is not possible to ensure the flow pattern that forms the base of the model and the results produced may be misleading.

4.2.1.2 - Heat transfer in the floor surface

The effects of floor heat transfer depend on whether there is negative or positive buoyancy. Negative buoyancy at floor level will be treated as a variation (decrease) in the air temperature from which the plumes entrain.

Positive buoyancy is potentially more disruptive. In a study on the influence of buoyancy flux on the horizontal boundaries of a displacement flow [Wells et al., 1999] shows that positive buoyancy at floor level promotes mixing in the lower layer. In an experimental study using a scaled model [Hunt et al. (2002)] show that even in the presence of dominant convection from the floor surface, a buoyancy driven two layer flow can be established whenever the plume buoyancy flux is more than 1/7 of the horizontal flux. A two layer structure can also be formed when the only heat source is a

heated portion of the room floor, as long as the heated area does not exceed 15% of the room floor [Holford et al., (2002)]. In view of these results it is possible to conclude that this is the simplest case to model:

All fluxes are treated as changes in the floor level temperature (see T_{FLOOR} below). In the case of positive fluxes a check is performed to compare the plume buoyancy flux with the floor level flux.

Heat transfer in the ceiling surface

This is the simplest case since heat flux occurs into a mixed layer and the model evaluates the possible disrupting effect calculating the average mixed layer temperature. If the buoyancy flux is negative with a magnitude such that the upper layer becomes colder than the lower region the model will indicate transition into mixing flow (see below).

4.2.2 - Internal heat sources

The main approximation when treating internal sources in the present model is:

All sources of buoyancy that generate plumes are considered to be either point sources on the floor of the room or finite volume sources whose virtual, equivalent point source, origin is at floor level.

This approximation is consistent with the simplicity that is pursued in our modeling approach and its first order accuracy goal. It is relevant to mention that in the most common design situations the location and number of the buoyancy sources is not known: are the occupants sitting or standing, are they using desktop computers placed on the floor or laptops, what type of lighting system is used (task, ceiling...).

Even in the rare case where n equal plumes are present in a room, variable plume strength may occur whenever there is plume coalescence. The width of a fully developed plume increases linearly with height according to:

$$b = \frac{6}{5} a z = 0.1524 z \quad (4.9)$$

Where a is the plume entrainment constant, considering top hat plumes. The best estimate is 0.13 [Linden, 2000]. When two or more plumes are sufficiently close coalescence may occur leading to a single plume with buoyancy strength equal to the sum of the strengths of the originating plumes. When the coalescence occurs above the mixed layer height it has no significant impact on the displacement flow in the occupied region, since the height of the mixed layer will not be affected by the coalescence.

Using (4.9) it is possible to conclude that two point buoyancy sources with origin in the room floor will generate plumes that overlap before two meter height whenever their origins are less than 0.3 m apart. Experiments have shown that coalescence can occur before 2 m for inter-plume distances of less than 0.5m, as a result of mutual entrainment by adjacent plumes [Kaye & Linden (2003)]. Whenever two or more plumes coalesce near the room floor a single plume is formed, making the single plume model adequate to model these multiple plume situations. This is relevant when modeling personal

workstations: often task lighting, personal computers and occupants are less than 0.5 m apart and can be modeled as a single plume.

Typically, even in an early design phase, the average internal loads and number of occupants for a given space are known. For most internal office arrangements it is reasonable to suppose that occupants and office equipment are less than, or approximately, 0.5 m away from each other, forming a single coalesced plume including the occupant and personal equipment gains (PC and task lighting). In this context it is possible to estimate the number of plumes and the average power per plume by dividing the total convective gains in the occupied zone of the space by the number of occupants. As shown in the previous section, the challenge with this simple estimation and consequent use of (4.7) to determine h is to model the effects of isolated single more powerful sources (such as a large photocopier, a server rack, a video wall, etc).

4.2.3 – Vertical distribution of internal gains

As visible in figure 4.1, whenever the thermal plumes are the sole buoyancy sources in a room the heat in these sources is totally convected into the upper warm layer. In rooms where other effects influence the flow, this ideal scenario may not occur due to:

Interference between thermal plumes and furniture. There are several situations where this interaction occurs. A PC placed under a table is a good example: an undisturbed plume is impossible in this case, since the heat released into the plume will have to flow horizontally, around the top of the table before flowing to the top of

the room, in addition most PC's have cooling fans and tend to release the heat in a small horizontal jet. Both of these effects promote mixing in the lower layer.

Interaction between negatively buoyant wall driven boundary layers and thermal plumes in the lower layer. As these flows reach the floor and propagate across the room mixing is induced. The bulk effect of wall-generated flows depends on the magnitude of these flows when compared with the internal heat sources, as discussed above.

Positive buoyancy input at floor level. As discussed above, sources of positive buoyancy at floor level promote mixing in the lower layer.

In the presence of these effects, using a model that considers total convection of the gains in the lower layer into the upper layer is unrealistic. A simple way to introduce this effect is to place a fraction of the convective heat gains of the thermal plumes in the occupied zone into the energy balance in this zone. The challenge is then to determine what value should be used in each case. In particular cases, the value of this coefficient (the fraction mentioned above) is easier to estimate:

In an open plan office (with a low ratio of lateral wall to floor surface area) and no significant solar gains (when compared to the total internal gains that generate displacement flow driving plumes) it is reasonable to expect that this coefficient will be close to zero, but never zero. For example, simply placing a PC under a desk leads to disruption of the thermal plume as it heats the table, directly convecting gains into the lower layer.

In a small room with a large number of furniture objects in the occupied zone and lateral walls with significant heat transfer (compared with the internal sources) this coefficient will have a higher value.

It is beyond the scope of the present model to determine the exact value of this coefficient, but even to be able to recommend approximate values, additional work is needed; either using appropriate detailed numerical simulation methods or laboratory experiments. At the moment, the best way to handle this uncertainty is to restrict the application of the model to rooms that are close to the first of the two cases mentioned above. Even in these cases it is advisable to use a conservative estimate for this fraction (in the simulations presented in section 4.5 the value of $1/3$ is used). In the equations presented below this gain distribution fraction is called FR_g .

4.3 – Description of the model implemented in EnergyPlus

The model that is proposed here predicts three temperatures considered essential to simply characterize a displacement ventilation flow (see figures 4.4 and 4.5):

The floor level temperature (T_{FLOOR}) allowing for accurate treatment of floor heat transfer and its effect on the inflow air that will then be entrained by the plumes in the occupied zone.

The occupied zone temperature (T_{OC}), representing the room occupied zone.

The upper node representing the mixed layer / outflow temperature (T_{MX}) essential for overall energy budget calculations and to model comfort effects of upper layer temperature.

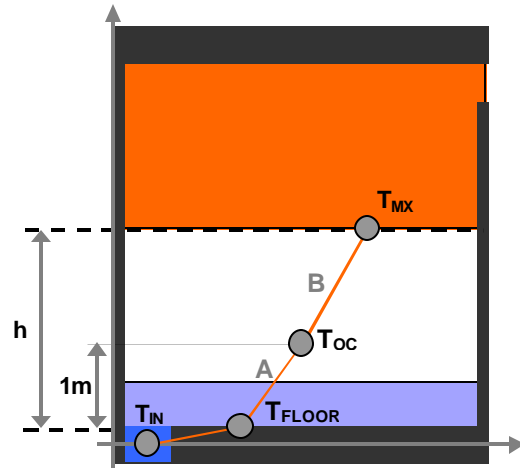


Figure 4.4

Schematic representation of the three temperature points and temperature gradients. The two temperature gradients are labeled A and B.

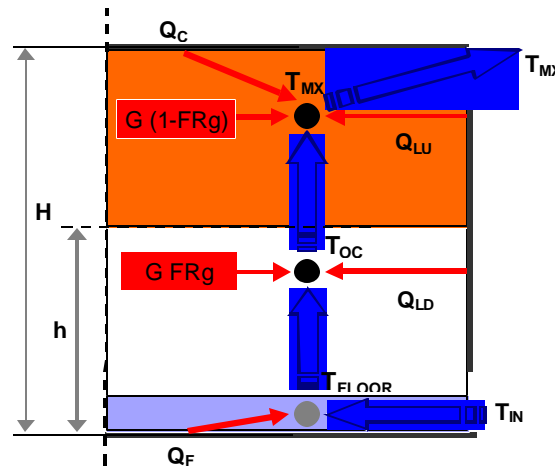


Figure 4.5

The structure of the three-node model. Shown in black are the two main nodes (T_{OC} and T_{MX}). The auxiliary node T_{FLOOR} is shown in gray.

The model uses the following approximations:

- All plumes are considered to have equal strength.
- All plumes are modeled as point sources of buoyancy located in the room floor.
- The effects of convection due to lateral wall boundary layers on the airflow pattern are not considered. The only convective heat transfers between vertical nodes occur upwards in the plumes.
- Heat transfer from each internal surface is evaluated using natural convection correlations. The room air temperature is represented by the room node that is in direct contact with the surface (see figure 4.5). The floor surface (or surfaces in case there is subdivision) is coupled to the floor level room air temperature node (T_{FLOOR}). The lateral surfaces are coupled to the occupied (T_{OC}) or mixed zone (T_{MX}) depending on their vertical location. In the case of a lateral surface that is in contact with both layers an area weighted room air temperature is used to model surface heat transfer.
- The total plume driving buoyancy flux is estimated by adding all the convective internal gains that are located in the occupied zone (G) that are not convected directly into the lower zone. The total plume driving gains are given by: $FRgG$.
- The height of the mixed layer (h) is determined using expression 4.5, considering n equal plumes.

The prediction of the room temperatures begins with the floor level temperature (T_{FLOOR}) and then proceeds to the occupied zone temperature (T_{OC}) and finally the mixed upper layer temperature (T_{MX}).

The floor level temperature is obtained by solving the energy equation, supposing a mixed layer above the floor (transferring heat only to the floor) and advecting heat into the occupied zone in a flow with flow rate F (see figure 4.5):

$$r C_P F (T_{FLOOR} - T_{IN}) = \sum_n^N h_{Fn} A_{Fn} (T_{FLOOR} - T_{Fn}) \quad (4.10)$$

The model allows for N floor surfaces to increase its flexibility and to allow for improved heat transfer calculation for each surface. The floor level temperature is then given by:

$$T_{FLOOR} = \frac{r C_P T_{IN} + \sum_n^N h_{Fn} A_{Fn} T_{Fn}}{r C_P + \sum_n^N h_{Fn} A_{Fn}} \quad (4.11)$$

The occupied zone temperature is obtained by noting that air flows into the occupied zone with temperature T_{FLOOR} , and by allowing for:

- Heat transfer with N lateral surfaces (for surfaces whose maximum height is smaller than h or that have a portion of its area exposed to lower layer air):
- A fraction of the convective gains to flow directly into this layer of the model.

This analysis results in the following energy conservation equation:

$$r C_p F(T_{OC} - T_{FLOOR}) = \sum_n^N h_{LLn} A_{LLn} (T_{OC} - T_{LLn}) + G.FRg \quad (4.12)$$

The occupied zone temperature is:

$$T_{OC} = \frac{r C_p T_{FLOOR} + \sum_n^N h_{LLn} A_{LLn} T_{LLn} + G.FRg}{r C_p + \sum_n^N h_{LLn} A_{LLn}} \quad (4.13)$$

Similarly, for the upper layer:

$$r C_p F(T_{MX} - T_{OC}) = \sum_n^N h_{LU n} A_{LU n} (T_{MX} - T_{LU n}) + \sum_n^N h_{Cn} A_{Cn} (T_{MX} - T_{Cn}) + G.(1 - FRg) \quad (4.14)$$

And the mixed upper layer temperature is:

$$T_{MX} = \frac{r C_p T_{OC} + \sum_n^N h_{LU n} A_{LU n} T_{LU n} + \sum_n^N h_{Cn} A_{Cn} T_{Cn} + G.(1 - FRg)}{r C_p + \sum_n^N h_{LU n} A_{LU n} + \sum_n^N h_{Cn} A_{Cn}} \quad (4.15)$$

The occupied zone temperature (T_{OC}) is meant to represent the room air temperature as felt by the occupants. The two other temperatures that are predicted have relevant roles in improving accuracy in surface heat transfer, and can be used to refine the prediction of user thermal comfort. For this prediction we will introduce a

derived temperature that is obtained from the three predicted temperatures in an attempt to extract all available model information to predict thermal comfort (the comfort temperature called T_{CMF}).

We begin by introducing a further approximation: consider that T_{OC} represents the temperature in the middle of the occupied zone (at one meter high, for the two meter occupied zone that is used. With this approximation it is possible to define two temperature gradients (between T_{FLOOR} and T_{OC} and between T_{OC} and T_{MX}), allowing us to use the information provided by the three node model to its fullest extent. Note that, for simplicity, T_{FLOOR} is defined as the air temperature at floor level (zero meter height).

From figure 4.5 we see that the comfort temperature can be obtained by calculating the average between the temperature in the first meter height, given by $(T_{FLOOR} + T_{IN})/2$ and the average temperature between one and two meter height:

$$T_{CMF} = \frac{1}{2} \left(\frac{T_{FLOOR} + T_{OC}}{2} + T_{OC} + \frac{1}{2} \frac{T_{MX} - T_{OC}}{h-1} \right) \quad (4.15)$$

Expression 4.15 is only meant to be used when $h \geq 1.5m$, when h is such that the mixed layer is in the occupied zone the benefits of the displacement flow are lost.

The average temperature gradient in the occupied zone is defined as the temperature difference between T_{FLOOR} and the temperature at 2m height (with this definition, when h is below 2m the average gradient does not increase). The maximum temperature gradient will be the higher of the two gradients shown in figure 4.4 (labels A and B in gray).

4.4 - Capabilities and limitations of the model

The model presented in the sections above should not be used in all situations. It is important to note that the model that was presented has been validated only for the simple configurations that form the basis for its development: a single or n -equal non-coalescing plumes in an adiabatic box [Linden et al., 1990]. For these cases the model is accurate and may even be better than CFD using the K- ϵ model [Cook & Lomas (1998)], that typically shows a small overestimation in entrainment, resulting in an under prediction of the mixed layer height. As shown in section 4.2, the n -equal plume model leads to conservative results when applied to asymmetric plume cases. The results in these cases are clearly superior to the perfectly mixed approach. In addition to these cases it is reasonable to expect that the model will also perform well when additional flow effects are present but are not disruptive to the simple vertical stratification that forms the basis of the model:

Whenever the heat flows generated by the lateral surfaces are much smaller than the flow driving thermal plumes in the occupied zone.

When a chilled floor is present (as long as radiative coupling with the ceiling does not lead to over cooling of the warm upper layer).

When the ceiling or the lateral surfaces that in contact with the upper layer have temperatures above T_{MX} .

The model should not be used in the following situations:

When the presence of a chilled ceiling leads to $T_{MX} < T_{OC}$ (in this case the model implemented will automatically perform a prediction using the mixed flow model).

Whenever the heat flows generated by the lateral surfaces are comparable to the flow driving thermal plumes in the occupied zone.

Whenever heat gains from the floor surface are comparable to the heat gains in the occupied zone.

In all cases that are between the two extreme situations described in the previous two paragraphs, the accuracy of the model is not known and further work is needed in two main areas:

Validation of the model and its implementation using experimental measurements in test chambers. For this purpose the implementation in *EnergyPlus* is essential, allowing for accurate simulation of the test chamber boundary conditions.

Improved definition of limits of model applicability.

Model extension to three vertical layers, improving its accuracy in configurations with highly asymmetric multiple plumes (see figure 4.3)

In order to simplify the use of the model, automating the many checks that are needed when accessing its applicability (influence of buoyancy driven flow from the internal surfaces, inflow conditions) a flow pattern selection algorithm is presented in chapter 5. This algorithm is also implemented in *EnergyPlus* and is expected to assist the user in using the models (both displacement and cross ventilation) developed in this thesis.

4 - Conclusions

A physically based simplified displacement ventilation model for temperature gradient and heat transfer prediction was successfully developed and implemented in EnergyPlus.

Further validation of the model and its implementation using experimental measurements in test chambers is needed in order to determine model accuracy in cases where other flow elements compete for flow dominance.

The model provides significantly improved accuracy when compared to existing perfectly mixed flow models, and is able to accurately predict vertical temperature variation and heat transfer with room internal surfaces for cases where the dominant heat fluxes in the room are a set of n equal plumes in the occupied zone of the room (considered to be between 0 and 2m height). When the plumes have variable strength the model produces conservative estimations, with decreased accuracy .

Tests of the model implementation show that the model is useful when designing displacement ventilation systems, both naturally and mechanically driven. In both cases, the ability to model vertical stratification leads to results that are not only more detailed, but also predicting lower indoor temperatures in the natural case, and lower energy consumption predictions in the mechanical case, hopefully leading to increased use of free running buildings using naturally driven displacement ventilation.

5 – Implementation of the models and a flow pattern selection algorithm

Abstract

This chapter presents the software implementation of the models developed in chapter 1-4 and a study on flow pattern selection resulting in a set of rules that are used to decide between flow patterns during and before a simulation. The models and a flow pattern selection algorithm are integrated in an existing whole building thermal simulation tool: EnergyPlus. The flow pattern selection method uses a set of simple geometry and flow scaling criterion to distinguish between: mixing, displacement and CV flows. The development of this set of decision rules had several goals: to develop simple criterion to distinguish between flows; to assist non-expert users in the selection of the correct flow pattern model and finally to automate the choice of models during numerical simulations in energy simulation software. This last point is particularly important in simulation of naturally driven ventilation systems where flow conditions can change several times per day, often leading to changes in airflow pattern. The decision rules and their software implementation are presented. An example of the automated use of the flow pattern selection rules in EnergyPlus is presented.

5 - Introduction

The implementation in EnergyPlus of the displacement and cross ventilation models developed in the first three chapters of this thesis is a fundamental component of this research effort, it significantly extends the impact of the work by allowing designers to apply the models, ultimately leading to better designed low energy cooling systems.

EnergyPlus [Crawley et al. (2001)] is a whole building thermal simulation software that was developed from two existing codes: BLAST and DOE2. This software simulation tool integrates three main components: the building thermal simulator, the HVAC system simulator and the naturally driven airflow simulator (COMIS [Huang et al. (1999)]). Starting from a simplified three-dimensional building geometry, materials, external apertures, local climate, internal gains and HVAC system (if any), EnergyPlus predicts room and building surface temperatures as well as humidity levels and energy consumption of the HVAC system. The unmixed-flow heat transfer models whose implementation is presented here will be used in EnergyPlus to calculate air to surface heat transfer. These energy transfers and room temperatures are then used to evaluate thermal comfort, determine HVAC system energy consumption and calculate naturally driven airflows. Simulations can be performed for a given period of the year using a user defined time step (between ten minutes and an hour).

This chapter presents the implementation of the models presented in chapters 1-4 in EnergyPlus, in addition a flow pattern selection routine is introduced. The new

capabilities that are introduced as a result of the implementation work presented below are:

Ability to model heat transfer and internal temperatures in displacement-ventilation airflow (subroutine CalcDisplacementVent).

Ability to model heat transfer and internal temperatures in cross-ventilation airflow of type R (subroutine CalcCrossVentRE).

Ability to model heat transfer and internal temperatures in cross-ventilation airflow of type C (subroutine CalcCrossVentCR).

A flow pattern selection algorithm subroutine that can decide which ventilation heat transfer model should be used at any given moment during a simulation.

As discussed, the models are introduced in EnergyPlus as additional surface heat transfer calculation methods. The existing methods are: Simple (using a constant, user defined heat transfer coefficient), Detailed (based on ASHRAE recommended correlations [ASHRAE, 2001]) and Ceiling Diffuser (this model calculates surface heat transfer with a ceiling diffuser, correlating forced convection heat transfer to inflow momentum flux). The user selects between existing room air heat transfer models and the four options presented above in a new input field, described in table 5.1. Table 5.2 shows details of a new input group that was created to contain additional input data for the models.

In order to distinguish between the three flow patterns considered, a Flow Pattern Selection (FPS) routine is implemented. This routine decides between mixed and

unmixed airflow patterns, depending on geometry, indoor surface temperatures, and

Table 5.1. *Modified input field, to be included in the currently existing ZONE field in EnergyPlus.*

| <i>Field</i> | <i>Description</i> | <i>Accepted Values</i> | <i>Additional Information</i> |
|-------------------------|--|---|---|
| Convection Algorithm | Type of airflow pattern assumed | Existing (simple, detailed...) and unmixed-flow: Displacement Ventilation C—V Recirculation C—V Corridor Flow Pattern Selection Algorithm | FPSA is the Flow Pattern Selection Algorithm. The models call the subroutines shown in the table below: CalcDisplacementVent CalcCrossVentR CalcCrossVentC CalcFPSA |

internal loads. In addition to making decisions on what flow pattern model is more adequate for a particular room with typical flow rates and geometry conditions, the FPS routine can also change the flow pattern model during the simulation.

Table 5.2. Description of the new input fields. The fields shown below are grouped in a new input group, named *Unmixed-flow* located after the existing *ZONE* input.

| Field | Description | Accepted Values | Additional Information |
|---|---|------------------------------|--|
| Zone Name | Name of Zone being described | Any existing zone name | - |
| Gain Distribution Schedule | Distribution of the convective heat gains between the two zones that exist in the unmixed models | $0 \leq \text{Value} \leq 1$ | In the DV model 1 means all convective gains in the lower layer. |
| Relaxation Factor | Numerical relaxation factor | $0 < \text{Value} \leq 1$ | When set to 1 the model uses the new value, when set to 0.5 the model uses the average between the current and previously calculated values. |
| Temp. Difference Threshold for Displacement Ventilation | Minimum temperature difference between predicted upper and lower layer temperatures above which the DV model is used. | $0 < \text{Value}$ | When the predicted temperature difference is below this threshold the model performs a mixing calculation. Only used in the DV model. |
| Comfort Temp. Distribution | Weighting factor for calculation of the comfort temperature using... For DV model: the lower and upper layer temperatures. | $0 \leq \text{Value} \leq 1$ | In the DV model using 1 makes the comfort temperature equal to the lower layer temperature. |
| Natural Convection Correlation | Correlation used for natural convection | ASHRAE or Awbi&Hatton | Awbi, H., B., Hatton, A., Natural convection from heated room surfaces, Energy and Buildings, 30, (1999) 233-244. |
| Number of plumes per occupant | As named. The model supposes a direct linear relation between the number of equal plumes and the occupants. | Any value above zero | The concept behind this approximation is that there is coalescence between occupants and equipment generated plumes. |

5.1 – Criterion for distinction between airflow patterns

The introduction of this thesis briefly discusses the three types of flow patterns that are subsequently analyzed. Table 5.3, below, synthesizes the discussion presented there. The four columns in the table show the fundamental set of flow and room geometry characteristics that distinguish the three flow patterns.

Most of the information presented in table 5.3 is straightforward to understand. The flow pattern that is most sensitive to inlet location is displacement ventilation due to the reliance on a stable vertically stratified temperature profile. If inflow has insignificant momentum, inlets whose height is below the middle of the occupied zone will not disrupt the stratification (as in previous chapters extending between 0 and 2 m in height). In the case of mixed and cross ventilation systems the word “Any” is only valid in a simplified modeling context.

The accuracy of the modeling approaches presented in this thesis does not extend to detailed issues of inflow aperture position. Clearly, placing a high momentum inlet close to or directly pointed at the occupied zone is not acceptable even in a mixing ventilation system, but those detailed problems are beyond the scope of the present work. The same reasoning applies to the use of the word “Any” in the column labeled outlet location. In the case of the cross ventilation model, all that is required is that the outlet is away from the inlet, so that the inflow momentum, can propagate across the room, defining a cross ventilation flow pattern. Due to limitations of the cross ventilation model developed, the FPS routine developed below requires the outflow aperture to be in front of the inlet. In the case of displacement ventilation, any outlet location above the occupied zone will allow for displacement ventilation. This does not mean that the flow

and heat transfer with internal surfaces in these cases is not influenced by the outlet: the height of the outlet defines the maximum value of the mixed layer height.

Table 5.3. *Basic flow pattern characteristics.*

| <i>Flow type</i> | <i>Ratio between Momentum and mass flux</i> | <i>Momentum conservation between inlet and outlet</i> | <i>Inlet location</i> | <i>Outlet location</i> |
|--------------------------|---|---|--|-------------------------|
| Mixed | Significant | Insignificant | Any | Any |
| Cross-ventilation | Significant | Significant | Any | Away from the inlet |
| Displacement ventilation | Insignificant | Insignificant | Below the middle height of the occupied zone | Above the occupied zone |

Table 5.4. *Situations that can lead to transition between flow patterns.*

| <i>From</i> | <i>To</i> | <i>Due to...</i> |
|-------------------|-------------------|---|
| Displacement | Mixing | Increased load removal in chilled ceiling system Increased momentum flux at the inlet Decrease in heat loads in the lower part of the room Negative or decreased heat flux through the room envelope |
| Mixing | Displacement | Increase in heat loads in the lower part of the room Increased heat flux through the envelope Decrease in load removal in chilled ceiling system Decreased momentum flux at the inlet |
| Cross-Ventilation | Mixing | Increased mixing in the room due to furniture and other obstacles Decreased momentum flux at the inlet |
| Mixing | Cross-Ventilation | Increased momentum flux at the inlet |

In addition to the flow properties presented in table 5.3, buoyancy effects also influence the flow pattern and can cause transition between the three flow patterns considered. Table 5.4 shows a set of situations where transition between flow patterns occurs, due to buoyancy and inflow momentum related effects.

5.2 – Example simulations using the CV model in *EnergyPlus*

In order to show the capabilities of the new model a set of simulations were performed for the single zone, naturally ventilated office building, shown in figure 5.1. Wind driven airflow was modeled using COMIS. Average experimentally measured pressure coefficients for a low rise building in open terrain were used [Swami & Chandra, 1987].

Using a set of three typical days of summertime San Francisco weather data a comparison between internal temperatures predicted by the cross ventilation model, case R and the ASHRAE detailed model (the single node, perfectly mixed room heat transfer model, currently available in EnergyPlus) was performed. The internal gains were placed in the Jet region, in front of the inlet.

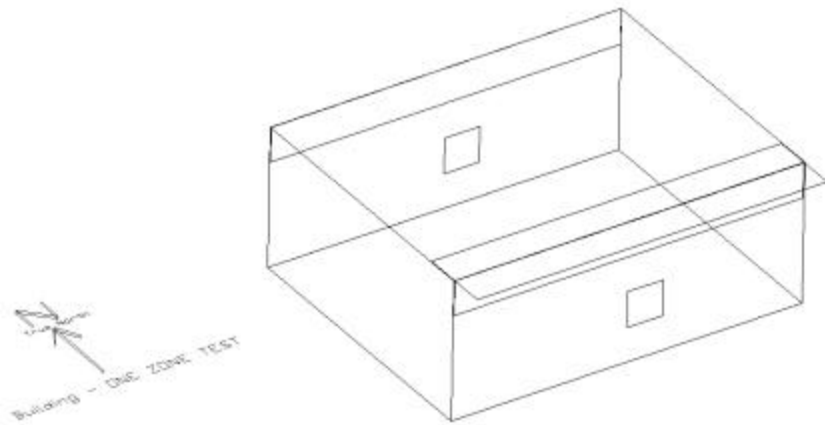


Figure 5.1

Single zone building used to test the implementation of the C—V(case R) model.

The building measures 10m (along the East-West direction), 8m (along the North-South direction) and 4m in height. One meter high clear glazing windows are used along the top of the South and North facades. The lateral walls are composed of two layers: 10cm of concrete on the inside and 5cm insulation on the outside. Ten occupants are present in the building between 9am-7pm. The occupation and internal gains are inserted and removed progressively from the building in the beginning (7-9 am) and end (7-8 pm) of the work day. The total internal gains (occupants and electric) are 50W/m². A 50% split between convection and radiation was used.

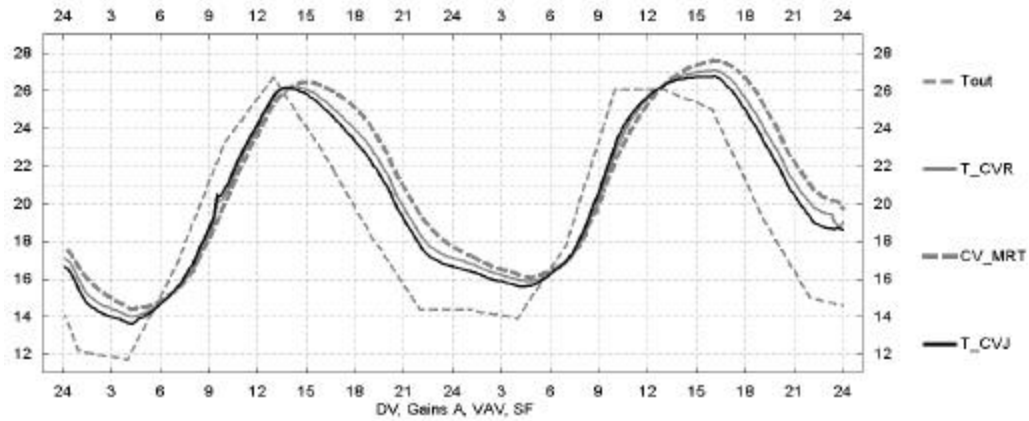


Figure 5.2

Predicted temperatures for two summer days in San Francisco using the cross ventilation case R model in EnergyPlus.

Tout: outside dry bulb temperature, T_CVR: air temperature in the recirculation region, T_CVJ: air temperature in the jet region, CV_MRT: mean radiant temperature for the cross ventilation flow model simulation.

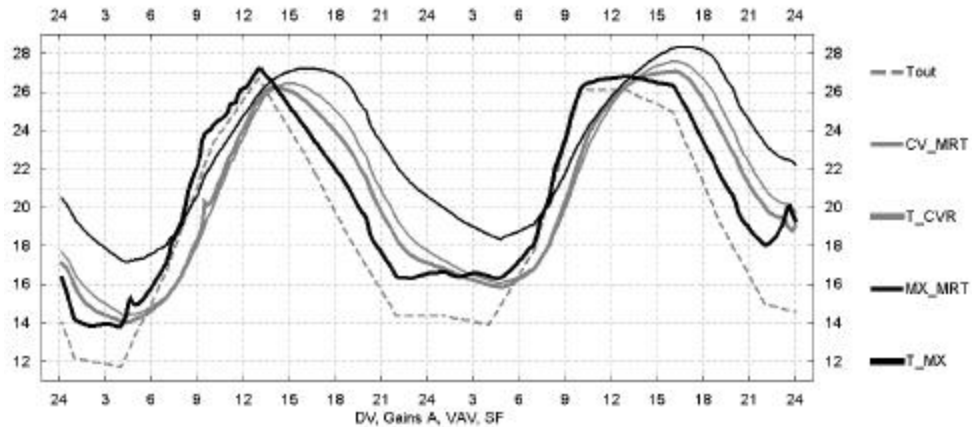


Figure 5.3

Comparison between predicted temperatures for two summer days in San Francisco using the cross ventilation case R model and the perfectly mixed flow model in EnergyPlus.

Tout: outside dry bulb temperature, T_CVR: air temperature in the recirculation region, T_MX: air temperature for the perfectly mixed flow simulation, MX_MRT: mean radiant temperature for the perfectly mixed flow simulation, CV_MRT: mean radiant temperature for the cross ventilation flow model simulation.

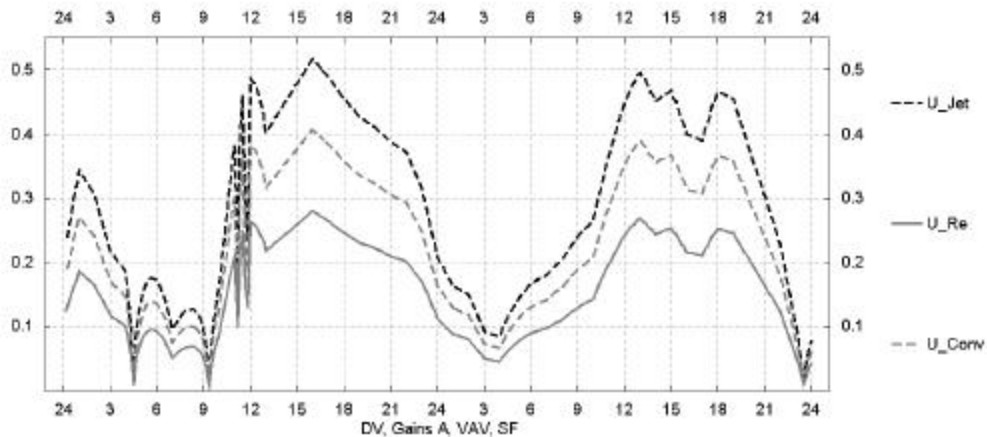


Figure 5.4

Predicted temperatures for two summer days in San Francisco using the cross ventilation case R model in EnergyPlus.

U_Jet: average airflow velocity in the jet region. U_Re: average air velocity in the recirculation region. U_Conv: average forced convection velocity near the internal surfaces.

Figure 5.2 shows the internal temperatures predicted using the new cross ventilation, case R model. During the morning, the jet-region temperature (in the chart: TCV_J) is similar to the recirculation region (TCV_R) and lower than the outside temperature: the benefits of heat absorption by the high thermal mass internal surfaces are clear (the average temperature of these surfaces is represented by CV_MRT in the chart). In the afternoon, as heat is accumulated in the thermal mass, both air temperatures are higher than outside temperature. During the night, gains are not present and, as expected, the temperature in the recirculation region is closer to the internal surface temperature.

Figure 5.3 shows a comparison between the predictions of the two models, and clearly there are significant differences. It is important to note that these differences are not solely due to the airflow pattern. The predictions also differ because the perfectly mixed model does not consider forced convection heat transfer (since a correlation for

average forced convection velocity was not available). The predicted internal airflow velocities are shown in figure 5.4. Clearly, the forced convection component is important in the present case.

5.3 - Simulations using the displacement ventilation model in *EnergyPlus*

In order to test and display the capabilities of the displacement ventilation model implementation in *EnergyPlus* a set of simulations were performed on a single zone (see figure 5.5), for selected days of San Francisco climate in the summer (TMY2 weather file).

Comparisons will be shown between the predictions of the new model and the currently available completely mixed model for three cases:

- 1 - A variable air volume system with an outside air economizer.
- 2 - A free running naturally ventilation system, using nighttime cooling ventilation.
- 3 - A chilled floor system with natural displacement ventilation, using a solar chimney.

Case 1 is the simplest application of the model and the advantages of displacement ventilation are expected to be clearly displayed. Case 2 is a more challenging application, a configuration where the model is expected to display clear differences in predicted temperatures that are generated by subtle airflow pattern properties. Case 3 is based on case 2: a chilled floor system is added. Once cooling is added, maintaining a

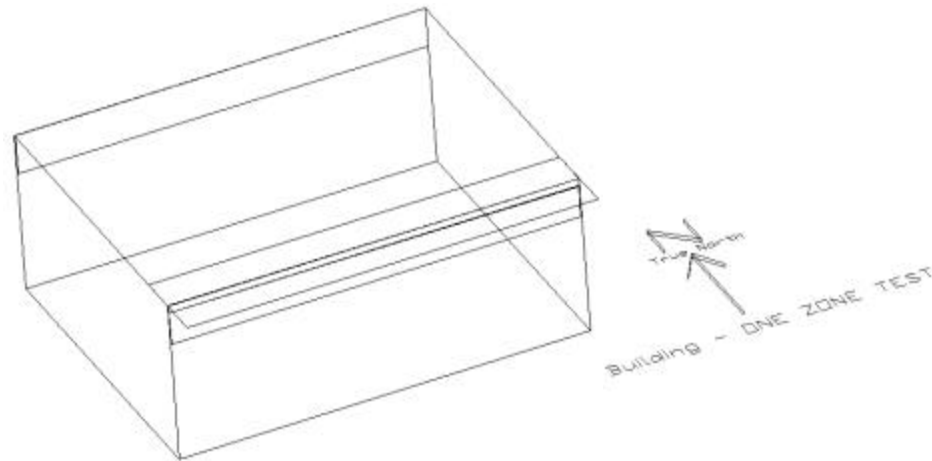


Figure 5.5

Model single zone office building used to test the model.

The building measures 10m (along the East-West direction), 8m (along the North-South direction) and 4m in height.

One meter high clear glazing windows are used along the top of the South and North facades (the south window is shaded).

The lateral walls are composed of two layers: 5cm of concrete on the outside and 5cm insulation on the inside.

Exposed thermal mass exists only on the floor and ceiling surfaces that are composed of two layers: 7.5cm of insulation on the outside and 7.5cm of concrete on the inside.

Ten occupants are present in the building between 9am-7pm. The occupation and internal gains are inserted / removed progressively from the building in the beginning (7-9 am) and end (7-8 pm) of the work day. Two gains scenarios are considered, with total gains of:

Case A = 40W/m^2 , Case B = 65W/m^2 (including occupant gains)

naturally driven airflow with the correct direction for displacement is not possible during the warmest hours of the day. In order to solve this problem a solar chimney system is added, with positive results. This last geometry has significant potential as a low energy cooling system, with the chilled floor being used only in very warm days, still the complexity of behavior of the system is visible as mixing conditions occur for some hours of the day.

In all simulations it is considered that the fraction of the internal gains that is convected directly into the occupied zone is 1/3 (as discussed in chapter 4 further research is needed to define the correct value to use for this variable).

5.3.1 - Variable air volume system with outside air economizer

We begin with a standard application of displacement ventilation, testing the ability of the model to characterize vertical stratification and display the known advantages of displacement ventilation when used with EnergyPlus. A sequence of two mild days, followed by a warm day was chosen to illustrate model behavior. The airflow system was tuned at design conditions so that the bottom limit of the mixed layer was located at a

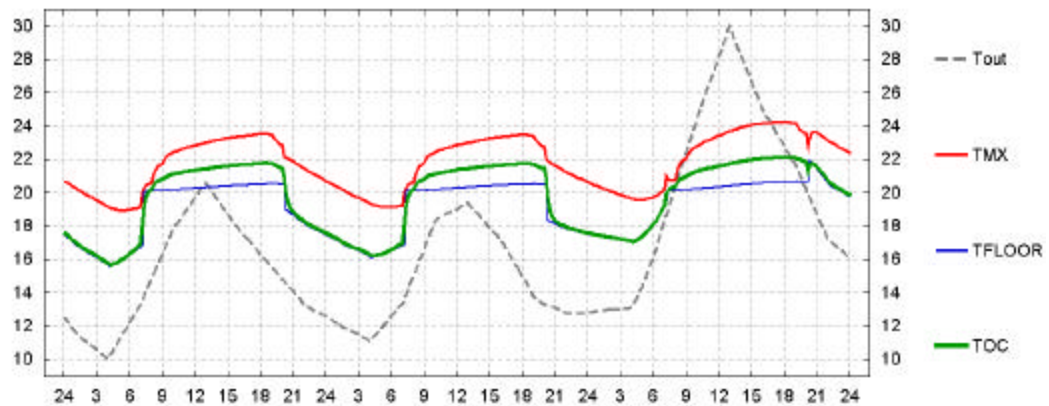


Figure 5.6

Temperatures in the three layers of the displacement ventilation model for a sequence of summer days in San Francisco. Vertical axis in °C, horizontal axis in hours.

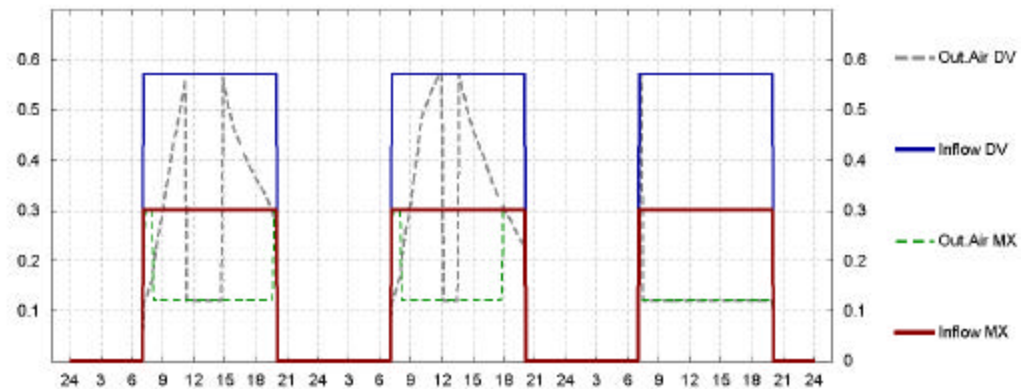


Figure 5.7

Room airflow and direct outside air in the variable air volume system for two ventilation systems.

Vertical axis: m^3/s , horizontal axis in hours. The lines labeled DV are for the Displacement Ventilation system, the lines labeled MX are for a mixing ventilation system.

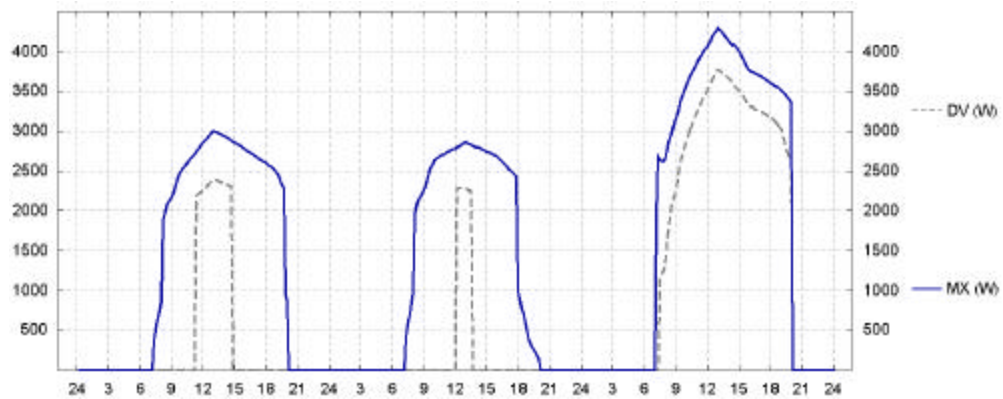


Figure 5.8

Cooling load required by the mixing and displacement systems for the days shown in figure 8. Vertical axis in Watts, horizontal axis in hours.

height of 2m. Fixed inflow temperature was set to 20°C in the displacement system and 15°C in the mixed system.

The predicted temperatures are shown in figure 5.6. The floor level temperature increases during the day as result of an increase in temperature of the floor surface due to solar and internal gains. During the unoccupied period there is infiltration (1Ach/h) and there are no internal gains and the occupied zone temperature is similar to the floor level temperature.

Due to the absence of thermal plumes the height of the mixed layer $h=H$, and the mixed layer temperature predicted by the model is influenced by the warm ceiling surface.

Figure 5.7 shows the room airflow and direct outside air in the variable air volume system for two ventilation systems. Figure 5.8 shows the predicted cooling load required by the mixing and displacement systems for the days shown in figure 5.6.

In figure 5.7 it is visible that, in order to maintain h above the occupied zone, higher airflow rates are required (probably leading to higher fan power usage). The effects of the higher inflow temperature are clearly visible (dashed lines) as the displacement ventilation system makes extended use of outside air in the two mild days.

In figure 5.8, the cooling load reflects the highly reduced energy consumption of displacement systems on mild days. The difference between the mixed and displacement systems is very small during the warmer day.

5.3.2 – DV in a free running naturally ventilated building, using nighttime cooling ventilation

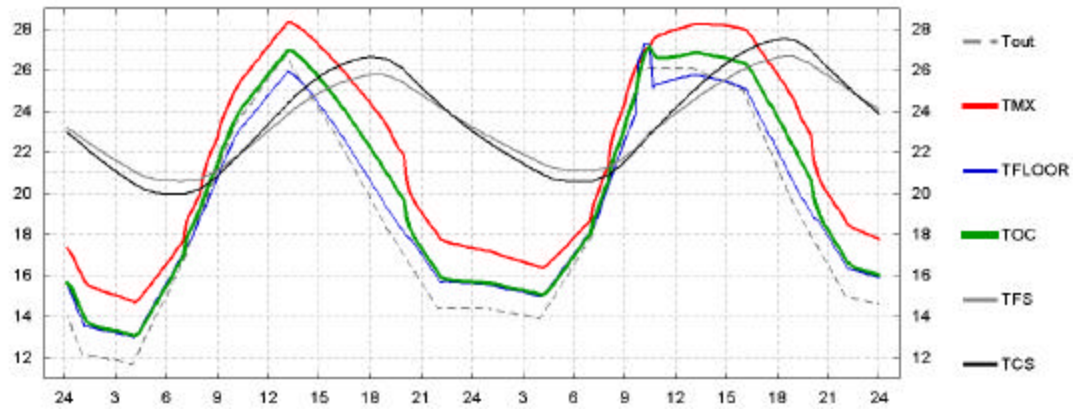


Figure 5.9

Temperatures in the three air layers, floor and ceiling of a displacement natural ventilation system for a sequence of summer days in San Francisco. Vertical axis in °C, horizontal axis in hours.

In this section we model the behavior of the building shown in figure 5.5 when using natural displacement ventilation (please see caption in figure 5.5 for building characteristics). A lower level inflow window is used on the north façade (outlet on the top of the south window, near the shading element). The inflow and outflow apertures have 1.5m^2 and the gain scenario *B* was used (65W/m^2). In order to simplify the interpretation of this example, no wind effects were considered.

Figure 5.9 shows the predicted room and internal thermal surface temperatures (ceiling and floor). Although moderate internal gains are present, the predicted occupied zone temperature (T_{OC} , green line in the figure) is close to the outside temperature during the morning, as a result of the night cooling effect (see temperature decrease of the ceiling and floor during the night period). In the afternoon the internal air temperature is above the outside temperature as a result of reduced ability to absorb heat in the floor and ceiling surfaces due to heating throughout the day. One of the interesting results of this simulation is that stratification allows for natural ventilation to occur from lower inlet to top outlet even when the occupied zone temperature is below outside temperature. In

a similar situation a mixed model would predict inverse natural flow (inflow through the top of the room) as well as an increased indoor temperature.

At 10 am on the second day the displacement ventilation flow cannot be maintained, this behavior is due to:

Accumulation of heat in the internal surfaces (comparison between the two simulated days, at 9 am shows that ceiling and floor are approximately one degree higher than in the previous day).

Hot outside air comes into the lower layer and makes it warmer than the upper mixed layer that is exposed to the lateral walls and ceiling and has a similar air temperature, making the implemented displacement model use a perfectly mixed flow approximation and output a value of zero for h , see figure 5.11.

Figure 5.9 presents a comparison between the prediction of occupied zone temperature of the displacement and mixed models for the present case. The relevant impact of displacement ventilation is clearly displayed, as predicted temperatures are 1-2°C below the predictions of the mixed model.

Figure 5.10 shows the predicted natural airflow rate and mixed layer fractional height

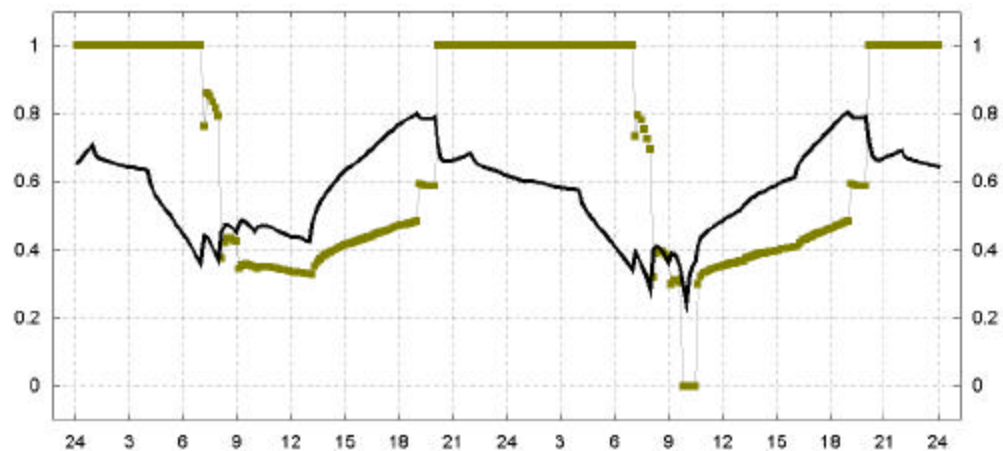


Figure 5.10

Fractional height of the mixed layer (h/H , squares) and naturally driven airflow (in black, m^3/s) for the two day period shown in figure 5.9.

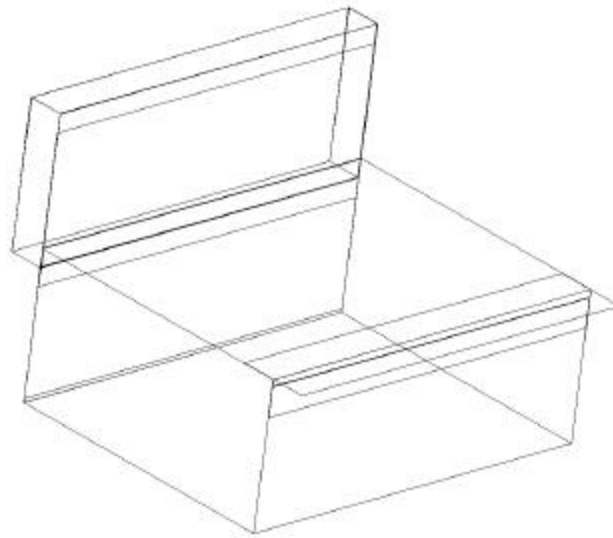


Figure 5.11

The single zone building in figure 5.5 with a solar chimney attached to the top of the North wall. The solar chimney is glazed on the South façade. The surfaces of the solar chimney are composed of an external layer of 5cm insulation and a 2.5cm internal layer of black painted concrete.

(h/H). Except for the hours where the flow becomes mixed, the height of the mixed layer stays above 1.5m even in this natural case.

5.3.3 - A chilled floor system with natural displacement ventilation using a solar chimney

When using natural displacement ventilation the use of a complementary radiative cooling system can be a solution to control indoor temperature in the warmer hours.

Although chilled ceiling systems are a popular solution to provide increased cooling power to displacement systems, their use when no air cooling system (as in the present example) is problematic: in these cases, the mixed upper layer can cool excessively

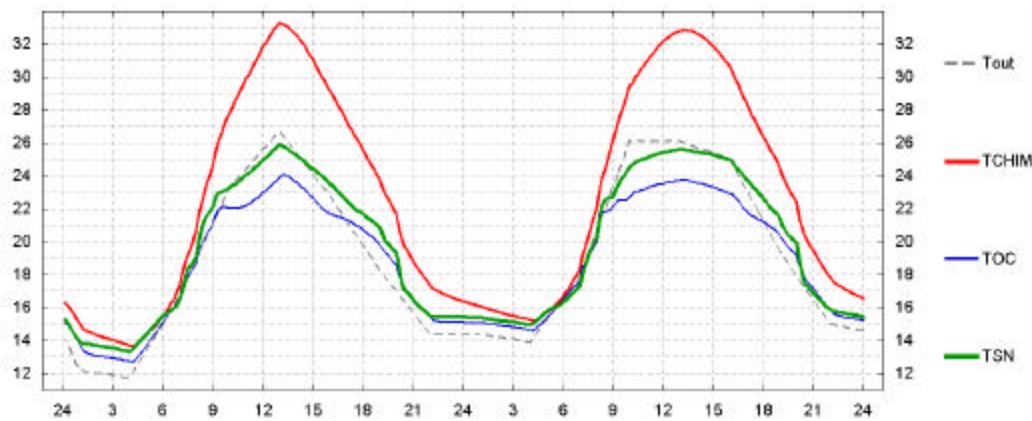


Figure 5.12

Comparison between the occupied zone temperature predicted by the displacement ventilation model (TOC), the room air temperature predicted by the perfect mixing model (TSN) and the average temperature predicted for the solar chimney in the displacement case.

(since the ceiling is the only cooling source during the warm periods of the day), eventually reaching the same temperature as the lower layer, inducing mixed conditions. In view of this, the use of a chilled floor system is more appropriate, cooling the inflow air and contributing to a stable stratification. The challenge is sustain natural displacement ventilation in the warmer hours of the day: if the vertically averaged internal temperature is below outside temperature the ventilation flow reverses and the flow tends to mix.

The natural solution to this problem is to use a solar powered chimney coupled to the outlet, increasing the stack effect and compensating the interior temperatures in the occupied zone. Figure 5.11 shows the geometry used with the solar chimney coupled to the north wall of the single zone building used in the previous two simulations.

Figure 5.12 clearly illustrates the success of this combined system, the temperatures in the solar chimney (line with the highest lines in the figure) are approximately 8°C higher than the occupied zone, generating the desired stack even in the warmer hours of the day. Comparison between the air temperatures in the occupied zone for the mixed

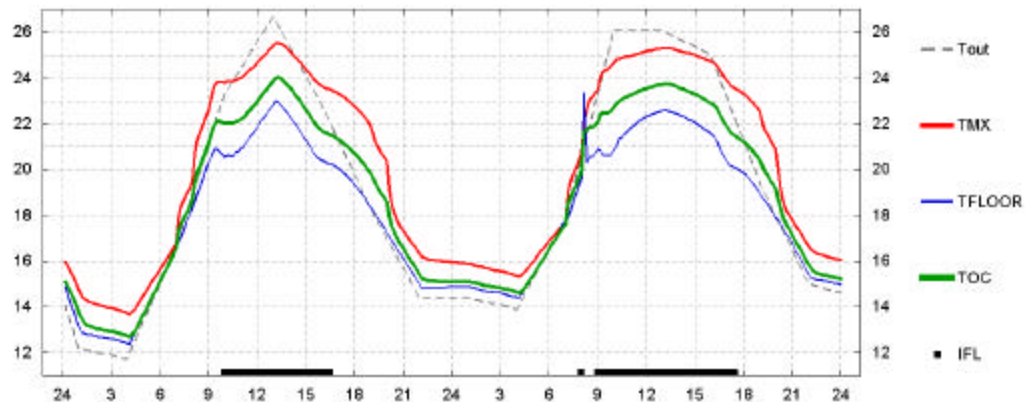


Figure 5.13

Temperatures in the three air layers, floor and ceiling of a displacement natural ventilation system using a solar chimney, for a sequence of summer days in San Francisco. The black squares labeled "IFL" signal time steps where the simulation with no solar chimney predicted reversed, mixed flow with inflow occurring at high level.. Vertical axis in °C, horizontal axis in hours.

and displacement ventilation systems show relevant differences (in order to make the comparison a similar maximum flow rate was used in the chilled floor systems for both cases).

As seen in figure 5.12, higher temperatures are obtained in the occupied zone in the mixed case as a result of having to handle all the internal gains with the same cooling power. The energy consumptions predicted for the two systems in the two days shown were similar (10%less in the displacement system).

Figure 5.13 shows the detailed internal air temperatures predicted by the displacement ventilation system. As in the previous case the system mixes in the early morning of the second day. The black squares shown in the figure indicate the hours where the same building, without the solar chimney would have reversed natural flow. Figure 5.14 shows the height of the mixed layer and predicted airflow rate. Note in the

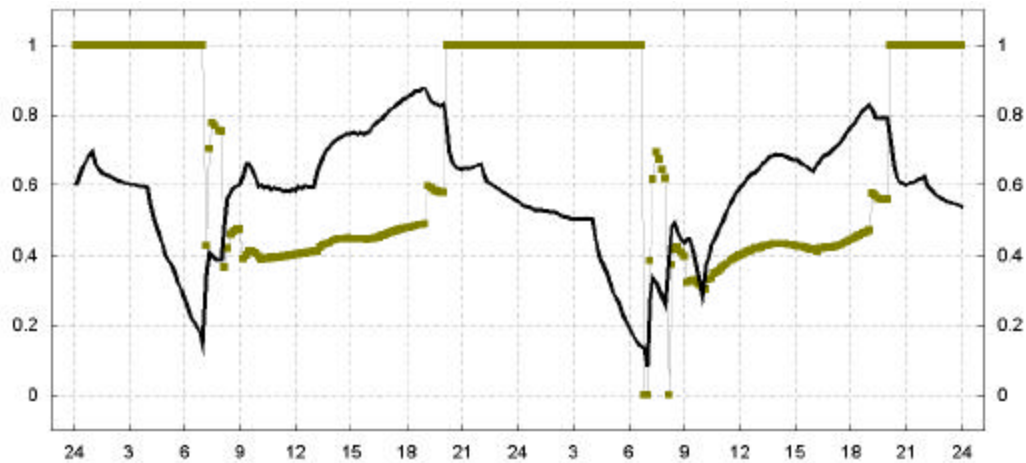


Figure 5.14

Fractional height of the mixed layer (h/H , in squares) and naturally driven airflow (in black, m^3/s) for the two day period shown in figure 5.13.

early morning of the second simulated day the effects of transition to mixing (h/H is then zero).

5.4 – Example of FPS operation: a free running building with a solar chimney and night cooling

In order to display the capabilities and advantages of the FPSA routine the building shown in figure 5.15 below was simulated using two typical days of San Francisco summer climate. A variable inflow opening geometry was used, leading to: natural wind and buoyancy driven displacement ventilation during the day and wind driven cross-ventilation during the night. This transition is obtained by doubling the area of apertures A and B (see figure 5.15) during the night.

As a comparison case for the simulation using the FPS algorithm a simulation was performed using the mixed flow model at all times. Figure 5.16 shows the results of the

two simulations (mixed model: gray line, FPS model: black line). During the day the FPS subroutine selects the DV model and the predicted occupied zone temperature is lower than the mixed model prediction. As the aperture areas of *A* and *B* increase (at 5pm) the FPS algorithm selects the cross-ventilation model and a higher occupied zone temperature is predicted (T_R from the CV model).

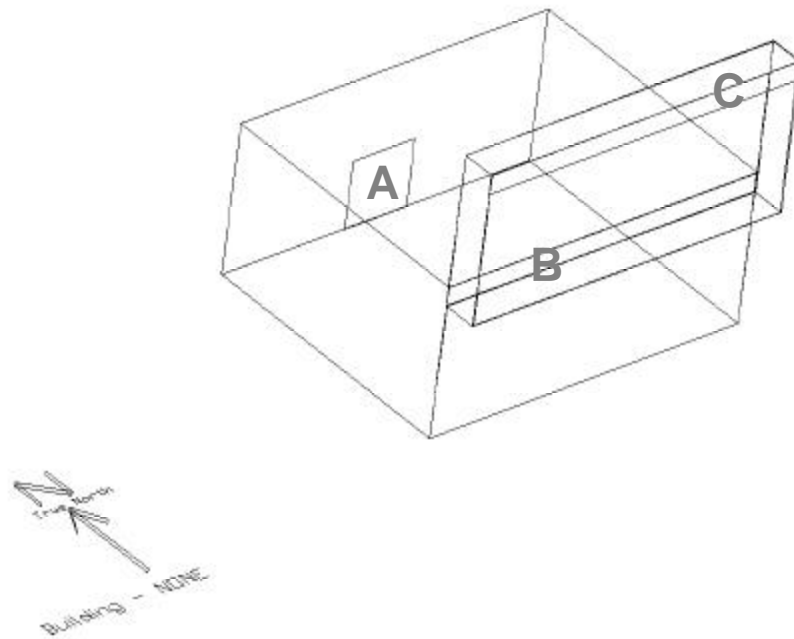


Figure 5.15
Geometry used to show test the FPS subroutine.

The single zone building is naturally ventilated with using a solar chimney. The area of the north inflow aperture (label *A*) varies throughout during the day (8am-5pm): $A_{IN}=1.8 \text{ m}^2$ in the reminding hours: $A_{IN}=3.6 \text{ m}^2$.

The area variation is obtained by changing the opening height. The chimney outflow aperture has 5 m^2 at all times (label *C*). The link between the zone and the chimney varies between 2.5 m^2 during the day and 5 m^2 at night (label *B*). Internal gains: 65 W/m^2 (including occupant gains)

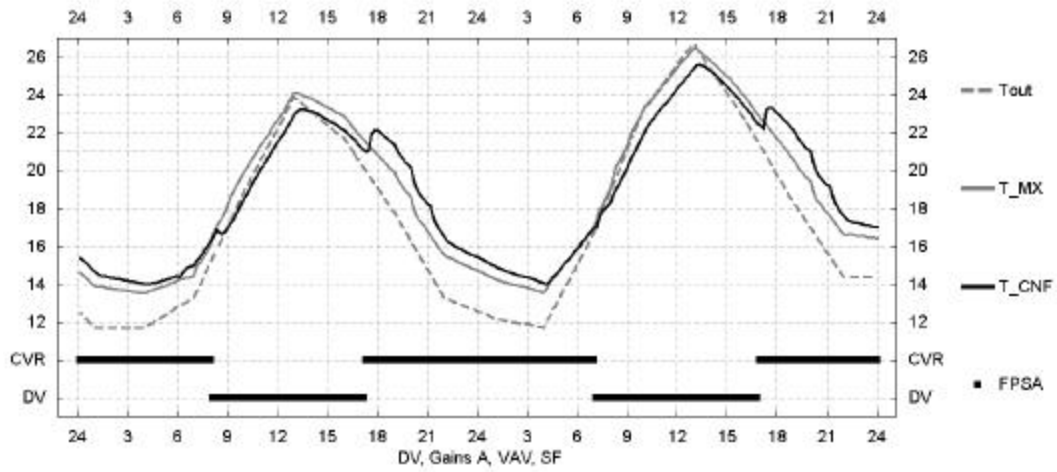


Figure 5.16

Results of the simulation of the case shown in figure 5.16 using the FPS routine.

In the plot: T_{out} is the outside air temperature, T_{MX} is the indoor air temperature predicted using the mixed flow model for the whole simulation period. FPS is an output variable from the FPSA subroutine that indicates, in each time step, which model is used. T_{CNF} is the comfort, occupied zone temperature predicted using the FPS algorithm. This temperature depends on which model is being used in the previous time step. When the DV model is used the FPSA algorithm outputs the T_{CNF} (see chapter 3), when the C-V model is used T_R is used (see chapter 2).

5 – Conclusions

The three unmixed-flow models developed in this thesis were successfully implemented in EnergyPlus. A flow pattern selection algorithm was also implemented, allowing for automated selection of the room air flow heat transfer model to use during the simulation.

The implementations minimize changes to the existing code structure, maintaining the existing room air node (use to represent the outflow temperature) and introducing additional nodes that are needed to model unmixed-flows. A room air temperature is introduced for each room surface, greatly improving accuracy of surface heat flux calculations.

A set of simulations using the new models confirm the significant differences in predicted results between mixed and unmixed-flow models that were found in chapters 2 and 4. Additional work is needed in the FPS routine, so that more geometries and flow transition situations can be modeled. The software implementation of the models greatly increases their usability in real design situations and their potential impact. Clearly, additional validation is needed for all the implemented models.

Conclusions

The work presented in this thesis provides a better understanding of the important parameters in the performance of cross ventilation and displacement ventilation systems. The approach used in this study was successful in capturing the dominant physical processes for these problems with first order accuracy, resulting in simple models that show the correct system behavior trends.

A new modeling approach to convective heat transfer between the building and the outside was presented: the concept of equivalent room heat transfer coefficient. This modeling approach clearly quantifies the reducing effect of air heating in room ventilation for the three ventilation geometries studied.

Chapters 1 and 2 a new approach to simplified modeling of cross-ventilation (CV) flows. The model developed in these chapters meets the proposed first order accuracy goal, while retaining simplicity in its form and application. By identifying the shear layer as the dominant flow feature, it became possible to simply model, within first order accuracy, a set of relevant flow variables in a complex flow. The functional dependences of the flow characteristics on the different room geometry parameters are clearly identified. A simple criterion to distinguish between different types of CV flow (C, R and CR) is introduced. The correlations presented in (1.16)-(1.19) model several relevant flow parameters in a compact way, making design and control of CV systems a simpler task. The analysis of effects of furniture presented in the second half of chapter 1 is only exploratory. Its relative success indicates that more scaling parameters and additional knowledge of the flow may be possible as a development of the present work, not only

on the effects of furniture but also to account for the effects of multiple inlets and non-rectangular room geometries.

The global room heat transfer coefficient introduced in chapter 2 proved to be a useful analytic concept for the cases with simpler airflow pattern (perfectly mixed flow and CV case C), displaying the reduction in heat transfer due to flow confinement effects. In flows of type R the coefficient has a complex expression and further simplification is needed to obtain sufficiently simple results. This simplification shows that, in this case shear layer heat transfer strongly influences the heat transfer process. The results of the CFD validation for the flows with surface heat transfer show that the perfectly mixed approach is inadequate to model cross ventilation flows, resulting in systematic overestimation of overall heat transfer, and failing to predict first order changes that are caused by variations in room aspect ratio.

In the cases combining internal heat gains with surface heat transfer the validation was limited and further work is needed. The results here indicate that the model is applicable in these combined cases and leads to improvements similar to the case with no internal gains, when compared with the perfectly mixed model.

Chapter 3 presents two contributions to simplified modeling of airborne pollutant removal in multi-zone cross-ventilated buildings. These contributions are applicable on two scales: inter-room flows and in-room pollutant concentration. On the first scale an improved CV model, obtained by introducing a momentum conservation term in the equation that relates pressure variations to flow through apertures is presented. On the room scale a development to non-buoyant flow of the work presented in chapter 2 is proposed. The resultant multi-zone pollutant removal model retains most of the simplicity of current simple models and is able to correctly calculate the flow through

offset outlet openings, predicting the variation in the flow rates with offset geometry. The predicted airflow and pollutant removal rates display the sensitivity of pollutant concentration to building geometry.

Chapter 4 presents a physically based simplified displacement ventilation model for temperature gradient and heat transfer. The model is an extension of an existing model to include surface heat transfer, with the goal of producing an implementation in a software tool. The model provides greatly improved accuracy when compared to existing perfectly mixed flow models and is able to accurately predict vertical temperature variation and heat transfer with room internal surfaces for cases where the dominant heat fluxes in the room are a set of n equal plumes in the occupied zone of the room (considered to be between 0 and 2m height). When the plumes have variable strength the model produces conservative estimations, with decreased accuracy. This model needs further research in how to deal with displacement flows in spaces with significant wall driven flows. The model may need to be modified to deal with these cases.

Chapter 5 presents the software implementation of the models developed in chapters 1-4 and a study on flow pattern selection. A set of rules, used to decide between flow patterns during and before a simulation, is presented. This flow pattern selection algorithm is expected to be a fundamental tool when using the models, particularly within a software tool in a building design context.

The models and a flow pattern selection algorithm are integrated in an existing whole building thermal simulation tool: EnergyPlus. A set of tests runs using the implemented models in EnergyPlus show that the models are useful when designing displacement and cross ventilation systems, both naturally and mechanically driven. In both cases, the ability to model unmixed flows leads to increased accuracy hopefully

leading to increased use of free running buildings using naturally driven displacement ventilation.

Further validation of the models and their software implementation using experimental measurements in test chambers and running buildings is needed in order to determine model accuracy in cases where other flow elements compete for flow dominance.

Appendix A - Shear layer momentum transfer

The shear layer that forms in the perimeter of the inflow jet is the transmission media for the momentum flux between jet and recirculation. If the recirculation flow keeps the momentum flux acquired in the entrainment process it is possible to estimate the momentum flux into the recirculation by estimating the momentum flux into the entrained room air.

Fig. 1.5 shows a schematic representation of the shear layer that develops in the perimeter of the inflow jet. Shear layers share a relevant feature with boundary layer flows: the main flow variations occur in the direction perpendicular to the main flow allowing for a solution strategy that neglects momentum diffusion in the flow direction.

The shear layer momentum flux scaling law is obtained by considering a control surface defined by moving the perimeter of the inflow aperture into the room (see in Fig. 1.5 the surface obtained by moving the perimeter B_1 , C_1 , D_1 and E_1 along the positive X-direction) and integrating the momentum flux through this surface, resulting in an estimate of the total momentum flux into the entrained flow.

If we consider that the entrained flow keeps the acquired momentum when it separates from the jet near the outlet, the shear layer scaling assumption for the recirculation flow momentum flux closes the problem. For simplicity, we will perform this analysis for the shear layer whose mid plane is defined by the points: D_1 - E_1 - E_2 - D_2 in Fig. 5. For simplicity, the boundary layer flow parallel to this plane will be modeled as two dimensional (no Z dependence). The momentum flux through this plane, per meter in Z, will be estimated and the resulting expression extended to the whole shear layer by

multiplying by the perimeter of the inlet, P . In this last step, all tri dimensional effects due to the rectangular geometry of the inlet and presence of the room are neglected. The averaged momentum equation for two-dimensional boundary layer flow in the XY plane with CV flow in the X direction is (introducing a eddy diffusivity, \mathbf{n}_T):

$$\bar{u} \frac{\partial \bar{u}}{\partial x} + \bar{v} \frac{\partial \bar{u}}{\partial y} = -\frac{1}{r} \frac{\partial \bar{p}}{\partial x} + \frac{\partial}{\partial y} \left[(\mathbf{n}_L + \mathbf{n}_T) \frac{\partial \bar{u}}{\partial y} \right] \quad (\text{A.1})$$

the over bar indicates a time averaged values. In addition, the flow conforms to the mass conservation equation:

$$\frac{\partial \bar{u}}{\partial x} + \frac{\partial \bar{v}}{\partial y} = 0 \quad (\text{A.2})$$

An average eddy diffusivity or turbulent kinetic viscosity will be used (ν_T). The result obtained will only be applicable when the eddy diffusivity does not vary in the Y direction and is much bigger than the laminar diffusivity ($\nu_T \gg \nu_L$). The solution is only valid in the turbulent part of the shear layer flow and, as shown below, depends on the experimental observation that turbulent shear layers grow linearly with X [Bejan, 1994]. A shear layer velocity scale U_0 will be used, representing the velocity variation between the two flow streams that compose the shear layer. In CV, the recirculation flow has negligible velocity when it is re-entrained, therefore, the shear layer velocity scale is given by the average inlet velocity, U_N .

The first and second terms on the right hand side of the momentum equation scale in a similar way. This becomes clear when using the mass conservation equation in the scaling process. In this way it is possible to scale v using U_0 and x :

$$\frac{\partial \bar{u}}{\partial x} = -\frac{\partial \bar{v}}{\partial y} \Rightarrow \partial \bar{v} \approx \partial y \frac{\partial \bar{u}}{\partial x} \Leftrightarrow \bar{v} \approx \partial y \frac{U_0}{x} \Rightarrow \bar{v} \frac{\partial \bar{u}}{\partial y} \approx \frac{U_0^2}{x} \quad (\text{A.3})$$

Scaling of the first term in A.1 is straightforward:

$$\bar{u} \frac{\partial \bar{u}}{\partial x} \approx \frac{U_0^2}{x} \quad (\text{A.4})$$

The right hand side of equation A.1, neglecting variations of pressure along X and eddy viscosity along Y, is given by:

$$\frac{\partial}{\partial y} \left[(n_L + n_T) \frac{\partial \bar{u}}{\partial y} \right] \approx n_T \frac{\partial^2 \bar{u}}{\partial y^2} \approx n_T \frac{U_0}{D^2} \quad (\text{A.5})$$

Inserting the scaling relations A.3, A.4 and A.5 in the momentum equation, A.1, leads to:

$$\frac{U_0^2}{x} \approx n_T \frac{U_0}{D^2} \quad (\text{A.6})$$

D is the shear layer width (from experiments: $D \sim O(x)$). In order for this simplified relation to apply, comparable magnitudes should occur on both sides, resulting in the following scaling for the effective turbulent viscosity in the shear layer:

$$n_T \approx U_0 x \quad (\text{A.7})$$

For convenience, this expression is multiplied by a constant when solving the momentum equation, resulting in the following formula for the effective turbulent viscosity:

$$n_T = \frac{1}{4\sigma^2} U_0 x, \quad (\text{A.8})$$

where σ is a constant that is determined experimentally (measured values range between 10 and 14 (Bejan, 1994)),

The solution for this approximate momentum equation (A.1 using A.8) is then:

$$\bar{u} = -\frac{U_0}{2} \cdot b\left(s, \frac{y}{x}\right) = -\frac{U_0}{2} \left[1 + \text{Erf}\left(s \frac{y}{x}\right) \right] \quad (\text{A.9})$$

Integrating A1 along Y, considering for convenience that the axis origin is in point D₁ and that $u(x, \delta)$ and $v(0, y)$ are zero, using the mass conservation equation in a standard integral analysis manipulation, results in:

$$\frac{d}{dx} \int_{y=0}^{y=d} \bar{u}^2 dy = -n_\tau \frac{\partial \bar{u}}{\partial y} \bigg|_{y=0} \quad (\text{A.10})$$

where δ is the size of the boundary layer (in the present case, generally never more than one quarter of the room width). As a result of using a two dimensional shear layer approximation, in plane $D_1-E_1-E_2-D_2$, expression A-10 is valid per meter, in the Z direction. This equation states that the momentum flux variations in the entrained flow (the region with: $0 < y < d$) are proportional to the momentum flux through the shear layer plane. Using A.9 to calculate the momentum flux through the mid plane of the shear layer (right side of A.10) leads to:

$$n_\tau \frac{\partial \bar{u}}{\partial y} \bigg|_{y=0} \cong -\frac{1}{4s^2} U_0 \cdot x \cdot e^{-\frac{y^2 s^2}{x^2}} U_0 s / \sqrt{p} \cdot x \bigg|_{y=0} \cong -\frac{U_0^2}{4s \sqrt{p}} \quad (\text{A.11})$$

We conclude that, under the assumptions used, the momentum flux is independent of the location in the shear layer interface. An overall analysis of the flow simulations presented in this thesis indicates that the length of the shear layer entrainment region (before the mass rejection stage) is approximately two thirds of the room length. Variations in the location of the starting point of the mass rejection stage, and therefore in the length of the shear layer, will be neglected. Inserting A.11 in A.10 and integrating in x between 0 and L , leads to:

$$\int_{y=0}^{y=d} \bar{u}^2 dy \bigg|_{y=0}^L = \frac{U_0^2}{4s \sqrt{p}} L \quad (\text{A.12})$$

The total momentum flux through the shear layer is obtained approximately by multiplying A.12 by the inlet perimeter (P). Further by considering that the recirculation flow occurs in an area proportional to the room cross section (A_R) and that this flow inherits the momentum flux into the entrained flow (left hand side of A.12), we obtain the following scaling result:

$$A_R \cdot U_R^2 = P \cdot L \cdot \frac{U_{IN}^2}{4s\sqrt{p}} \quad (\text{A.13})$$

When the perimeter is replaced by four times the square root of the inlet area, a more universal length scale for the inlet flow, A.13 leads to:

$$U_R = \sqrt{\frac{\sqrt{A_{IN}} L}{A_R s \sqrt{p}}} \cdot U_{IN} \quad (\text{A.14})$$

Appendix B - Heat transfer in a shear layer.

The analysis of heat transfer in a shear layer is similar to the momentum transfer analysis presented in Appendix A. The two processes are similar with heat and momentum transfer occurring in the turbulent eddies in a similar way and that is reflected in the equations and approximations used when modeling both processes. The heat equation is then similar to the momentum equation in a shear layer, and allows for similar approximations, in particular, two dimensional treatment and neglecting second derivatives in the shear flow direction (see figure 1.5):

$$\bar{u} \frac{\partial \bar{T}}{\partial x} + \bar{v} \frac{\partial \bar{T}}{\partial y} = \frac{\partial}{\partial y} \left[(\mathbf{a}_L + \mathbf{a}_T) \frac{\partial \bar{T}}{\partial y} \right] \quad (\text{B.1})$$

Two further approximations are possible that make the equation similar to the momentum equation solved previously, they are, neglecting the laminar heat diffusivity (α_L) and further stating the similarity in the two turbulent mixing processes by using:

$$Pr_T = \frac{\mathbf{n}_T}{\mathbf{a}_T} \approx 1 \Rightarrow \mathbf{a}_T = \frac{1}{4s^2} U_0 x \quad (\text{B.2})$$

Where Pr_T is turbulent Prantl number, the ratio between heat and momentum eddy diffusivities. With these approximations the solution for the temperature variation across

the shear layer is similar to the velocity profile, but with temperature differences replacing the velocities:

$$\bar{T} - T_R \cong \frac{T_{IN} - T_R}{2} \left[1 + \text{Erf} \left(s \frac{y}{x} \right) \right] \quad (\text{B.3})$$

Again following the previous analysis there is particular interest in the heat transfer across the middle plane of the shear layer:

$$\frac{q_{y=0}}{r C_p} = a_T \left(\frac{\partial \bar{T}}{\partial y} \right)_{y=0} = \frac{U_0}{4sp^{\frac{1}{2}}} (T_J(x) - T_R(x)) \quad (\text{B.4})$$

integrating this result in the surface that limits the shear layer, extending over the full length (L) of the room and the perimeter of the shear layer in the direction perpendicular to the flow, we obtain:

$$\frac{Q_{y=0}}{r C_p} = L \cdot P \frac{U_0}{4sp^{\frac{1}{2}}} DT_{SL} \quad (\text{B.5})$$

Where DT_{SL} is the average temperature difference across the shear layer in the room, defined by integrating along the shear layer surface:

$$DT_{SL} = \frac{\int_{SL} T_J(x) - T_R(x) ds}{L \cdot P} \quad (\text{B.6})$$

As in chapter 1, we estimate the characteristic velocity of the shear layer according to:

$$U_0 = \frac{F}{C_D \cdot A_{IN}} \quad (B.7)$$

For the purpose of analyzing cross ventilation flows of type R we define an area for the shear layer and a shear layer heat transfer coefficient in the following way:

$$A_{SL} = L \cdot P, h_{SL} = \frac{r C_P F}{C_D \cdot A_{IN} \cdot 4 s \sqrt{p}} \quad (B.8)$$

Resulting in a compact form for total heat transfer across the shear layer:

$$Q_{y=0} = A_{SL} h_{SL} dT_{SL} \quad (B.9)$$

Without the integration along the X direction (B.9) becomes:

$$r C_P F \frac{\partial T_J(x)}{\partial x} = - \frac{A_{SL}}{L} h_{SL} (T_J(x) - T_R(x)) \quad (B.10)$$

Appendix C - Simplified analysis of buoyancy effects on the airflow pattern.

Room heat transfer cases, where buoyancy dominates or competes for dominance in the flow pattern and associated momentum fluxes, will not be treated in this work because they fall outside the definition of CV flows. The horizontal flow pattern that forms the base of the cross ventilation model developed in chapter 2 can be disrupted whenever buoyancy induced flow has comparable magnitude to the CV flow. This appendix presents a simple analysis of buoyancy effects with the goal of clarifying the limits of model applicability.

Clearly, in a room with no internal sources and a very high flow of air with a small temperature difference with the internal surfaces, buoyancy recirculations will not influence the flow pattern and heat transfer path. When the flow rate decreases, there is a point when buoyancy effects start to interfere and are significant. Buoyancy forces are a consequence of a basic property of gaseous mixtures: when heat is absorbed by a fluid element of its temperature increases resulting in a small expansion that decreases its density, the opposite occurs when the fluid element releases heat. When a fluid element has a different density from its surroundings it is subjected to a buoyancy force that can change its momentum, and, therefore, the momentum flux through a given control volume in the room. Although buoyancy induced flows are vertical, horizontal flows can occur in order to close convection loops generated as buoyancy entrained air is replaced by room air, ensuring mass conservation in a similar way to the previously described

horizontal recirculation flows. The buoyancy induced convection loops that can occur in CV flows are perpendicular to the cross flow direction and create, in that plane, a short circuit in the heat transfer path. When the buoyancy-induced recirculations have a higher flow rate than the recirculation the flow can be unstable, and the heat transfer problem is much more complex to model and to simulate numerically (a transient instantaneous numerical model approach such as LES or DNS [Pope, 2000] would be needed).

In the case of flow patterns of type C, buoyancy effects contribute to enhanced mixing (perpendicular to the cross ventilation flow direction), this is one of the assumptions used in the model, so, buoyancy makes the fully mixed assumption in the model more applicable.

While the effects of buoyancy fluxes on the flow pattern are visible in many room airflow situations, they are difficult to quantify. In any room heat transfer case it is possible to estimate the magnitude of the buoyancy flux by estimating the total heat transferred into the fluid. Unfortunately this does not result in an appropriate scaling of buoyancy effects because buoyancy induced flow appears in several forms: wall boundary layers, thermal plumes and changes in inflow jet propagation path due to buoyancy. In the next paragraphs we will attempt to evaluate these different elements.

Vertical motion of the inflow jet due to buoyancy forces

Whenever the inflow jet is cooler than the room surfaces the inflow jet drops as it flows through the room. This vertical motion can invalidate the horizontal cross ventilation hypothesis that forms the base of the present model by introducing a strong vertical component in the room flow. In order to estimate the magnitude of this effect we will

obtain a non-dimensional factor that approximately determines whether the inflow jet drops to the room floor before exiting the room. Clearly, if this drop occurs close to the inlet the disrupting effect is significant, whereas if the jet exits the room before dropping the effect is small. As in previous cases, we will perform a first order analysis, based on scaling arguments, ignoring viscous effects.

Since the model predicts the total heat flux between the internal surfaces and the airflow (Q_T in watts) it is possible to estimate the negative buoyancy flux from the inflow jet:

$$B = \frac{g b Q_T}{r C_p} \quad (C.1)$$

Supposing a flat inflow velocity profile, and considering a flow contraction into an area $A_{IN} C_D$ (see chapter 1), the specific inflow momentum flux is given by:

$$M = \frac{F^2}{C_D^2 A} \quad (C.2)$$

The units of C.1 are m^4/s^3 , the units of C.2 are m^4/s^2 , therefore the length scale after which the jet will be affected by buoyancy is given by the product: $M^{3/4}/B^{1/2}$. (the jet length).

This length scale can then be compared with the room length:

$$g = \frac{\left(\frac{F^2}{C_D^2 A} \right)^{3/4} / \left(\frac{g b Q_T}{r C_p} \right)^{1/2}}{L} \quad (C.3)$$

When $\gamma \gg 1$ the cross ventilation flow pattern is significantly affected by this drop, whereas when $\gamma < 1$ this effect is expected to be negligible.

Buoyancy flow induced by point sources of buoyancy (thermal plumes)

In this case, the most likely situation when buoyancy can be important in the flow is when it competes for dominance with the flow in the recirculation region. For this reason, its effects can be estimated by comparing the flow rate in the recirculation region (expression 1.18) with the total flow rate due to the thermal plumes.

In chapter 3, expression 3.7 gives the buoyancy induced flow rate for the case of multiple non coalescing plumes (n), with equal strength, the total vertical airflow for a given height is:

$$M = \sqrt[3]{n} \frac{6}{5} a^{4/3} \sqrt[3]{\frac{9}{10}} p^{2/3} \sqrt[3]{B z^5} \quad (C.4)$$

For scaling purposes, it is adequate to set: $z=H$.

Buoyancy flow induced by vertical surfaces

Because of their geometrical configuration the room surfaces have the ability to generate buoyancy in an organized way. For this reason this analysis focuses mainly on the effect of these surfaces. It is illustrative of the complexity of buoyancy to consider qualitatively the effect on buoyancy fluxes of the different room surface orientations: A heated ceiling produces no significant buoyancy flux because all heat that goes into the fluid induces motion in the direction of the ceiling, therefore resulting in no induced momentum flux. Buoyancy flux from the floor tends to be reduced by the descending motion that cool air entering the room displays. In this way the possible momentum fluxes due to heating at floor level are reduced, still, they have an effect in the flow. In this simple analysis this effect is not considered. We are then left with the lateral room surfaces and their favorable geometry for buoyancy induced momentum variations.

The following analysis will focus on these boundary layers, taking advantage of the available experimental results to estimate the buoyancy induced mass flow rate that the lateral walls can generate. This analysis continues with the estimation of the magnitude of the buoyancy driven volumetric flow rate and compares it with the forced, recirculating flow component.

The analysis presented so far in this appendix applies to heated room surfaces, the following analysis of buoyancy effects will also be based on this more common case. It should be noted that the model is also applicable to warm air and cooled surfaces. In order to estimate the buoyancy induced volumetric flow rate the following analysis uses the boundary layer velocity and temperature profiles proposed by Eckert and Jackson [1951] in conjunction with the experimental correlations for heat transfer from compartment surfaces obtained by Awbi & Hatton [1999].

The analysis begins by introducing the velocity and temperature profiles in the boundary layer in the energy equation followed by a volumetric integration in the boundary layer region. After this step, the correlations [Awbi & Hatton, 1999] are introduced and the energy equation will be integrated in the vertical direction between zero and the room height (H). This analysis does not include, the effects of the horizontal recirculating airflow. The joint effect of forced and natural flows is analyzed in part 2 of this thesis. Eckert and Jackson [1951] proposed the following velocity and temperature functions to characterize the variations in the direction perpendicular to the boundary layer:

$$V(x) = \frac{V_{MAX}}{0.537} \left(1 - \frac{x}{\delta}\right)^4 \left(\frac{x}{\delta}\right)^{\frac{1}{7}}, T^*(x) = \frac{T(x) - T_{\infty}}{T_w - T_{\infty}} \left(1 - \left(\frac{x}{\delta}\right)^{\frac{1}{7}}\right) \quad (C.5)$$

Where:

x is the coordinate perpendicular to the boundary layer.

δ is the boundary layer thickness ($V(\delta)V_{MAX}/100$).

$V(x)$ is the dominant velocity component in the boundary layer (in the z direction).

V_{MAX} is the maximum vertical velocity in the boundary layer.

$T(x)$ is the temperature profile in the boundary layer.

T_w is the room surface temperature.

T_{∞} is the outer layer temperature (in this case a point inside the room, $x=\delta$).

T^* is the non-dimensional boundary layer temperature.

The energy equation, using the common boundary layer approximation (neglecting the second derivative in the boundary layer flow predominant direction) is:

$$U(x)\frac{\partial T(x)}{\partial x} + V(x)\frac{\partial T(x)}{\partial y} = \frac{\partial}{\partial x} \left((\alpha_L + \alpha_T) \frac{\partial T(x)}{\partial x} \right) \quad (C.6)$$

Where:

$U(x)$ is the velocity perpendicular to the surface.

α_L is the laminar heat diffusivity coefficient.

α_T is the turbulent heat diffusivity coefficient.

Introducing profiles in 25 in equation 26 and integrating across the boundary layer, we obtain a simple ODE whose variable is the product $V_{MAX} \cdot \delta$:

$$\frac{0.0366}{0.537} (T_w - T_\infty) \frac{\partial}{\partial y} (V_{MAX} \cdot \delta) = \frac{q_w}{r C_p} \quad (C.7)$$

Since the volumetric flow rate (the integral of the velocity across the boundary layer) is proportional to this product (the constant is 0.273 show explicitly), solving this equation results in the desired estimate. Here we introduce the approximate formula for heat transfer introduced in section 2.3.3 (expression 2.28):

$$q_w = 1.6 (T_w - T_\infty)^{\frac{4}{3}} \quad (C.8)$$

Integrating this solution around the perimeter of the room (obtained taking an horizontal cross section) and between zero and H results in:

$$V_{MAX} d = \frac{H.h_c.(T_W - T_\infty)^{\frac{1}{3}}}{r.C_p} \Rightarrow Q_B \approx \frac{H.(W + L).(T_W - T_\infty)^{\frac{1}{3}}}{100} \quad (C.9)$$

In figure C.1, we see the result of this preliminary estimate. The main conclusion is that for moderate to high flow rate, buoyancy induced flow due to internal heated surfaces is negligible when compared with the recirculation horizontal volumetric flow rate. For lower flow rates, buoyancy induced flow becomes comparable to the horizontal momentum driven flow. In this region the model may not be applicable and further analysis is needed.

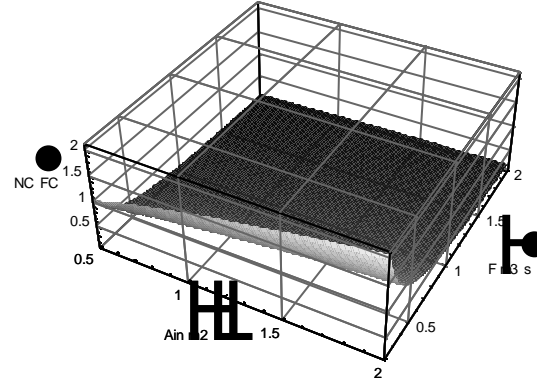


Figure C.1

Ratio between buoyancy driven volumetric flow rate and horizontal momentum driven recirculation volumetric flow rate. Horizontal axis: C—Vflow rate, inlet aperture area. $T_W=30$, $T_{IN}=27$, $W=5$, $L=5$, $H=5$.

Appendix D – Software implementation of the models

The internal structure of EnergyPlus room air temperature calculation uses a single node to model room air temperature. This approximation is adequate if room air is perfectly mixed. However, whenever there is stratification, or recirculating flow, significant errors result from using the perfectly mixed approach. One of the challenges of the implementation process was to add as little complexity as possible to an already complex code. In order to make minimal changes to the existing code structure, the implementation uses an embedded multi-node structure. While a single node (representing the temperature of the outflow air) is maintained, additional nodes are introduced, allowing for the inclusion of the recirculation zone or the horizontal layers of the displacement model.

Even in this very simplified form one additional problem remains; the equations used to model the flow and associated heat transfer processes are nonlinear and interrelated. For example, in the case of the displacement ventilation model:

Heat transfer with the lateral surfaces depends on h (see expression 4.5), air and surface temperatures that, in turn, depend on heat flux from the walls. In addition, the local heat transfer coefficients depend on the temperature difference and flow regime.

Because the unmixed-flow heat transfer models are introduced in EnergyPlus as part of sequential calculation process that cannot be changed in a simple way, a coupled

analytical solution is not possible. The solution is then to solve iteratively, calculating the heat transfer coefficients, then the mixed layer height and finally the three layer temperatures. This calculation must be repeated until the predicted changes from the previous iteration are insignificant (less than 10^{-3}). In the software implementation presented below it was found that, in all cases tested, this solution procedure is stable and five iterations are sufficient for convergence. Table D.1 contains a description of the subroutines used in the implementation.

The algorithms implemented to perform the calculations required by the unmixed-flow models operate along the following steps:

- 1- Check if it is the first call to the model in the simulation: if YES, initializes the surface temperature and location arrays (by calling the subroutine `IniUnmixFlow`), performing an organization of information already available in `EnergyPlus`, allowing for a more compact implementation and use of the code.
- 2- Proceed to the main calculation. In the DV model: the matching height (h) is calculated, followed by the calculation of the three room air temperatures and finally the calculation of the surface heat transfer coefficients. In the CV model the recirculation and cross ventilation temperatures are calculated, followed by the heat transfer coefficients. In both models, this process is repeated five times to ensure convergence (changes in all calculated variables between iterations are lower than 0.1%) of the nonlinear system.
- 3- For DV: if the occupied zone and mixed layer temperatures differ by less than the mixed ventilation threshold defined by the user, a mixed

calculation is performed. The CV model is always used unless the room geometry and inflow velocity tests fail.

In the implementations of both models, an equivalent room air temperature is calculated for each surface. This temperature depends on the surface location in the room, for example the floor in a displacement system is always in contact with the floor layer and the room air temperature that is used for the heat balance of this surface is T_{FLOOR} . This temperature is used to calculate the convective heat transfer coefficients and surface convection, in each time step. The room air temperatures for each surface in a room are stored in the array: *TAirSurface*.

Figures D.1 and D.2 show the schematic operation sequence for the CV case C and R modeling subroutines. Figure D.3 shows the schematic operation sequence for the displacement ventilation modeling subroutine. Tables D.2 and D.3 shows the new outputs of the models.

Table D.1. Description of the subroutines used in the implementation of the heat transfer models in EnergyPlus.

| <i>SubRoutines</i> | <i>Description</i> |
|-----------------------------|---|
| <i>IniUnmixFlow</i> | Unmixed-flow models initialization subroutine. All the data preparation needed to run the unmixed flow models. The subroutine sets up arrays with the locations in the main EnergyPlus surface array of ceiling, windows, doors and walls. The zone maximum and minimum height is calculated. |
| <i>CalcDispVent</i> | Subroutine for displacement ventilation modeling. This subroutine calculates the mixed layer height, surface heat transfer coefficients and room air equivalent temperatures and three space temperatures (floor level, occupied zone and upper, mixed layer temperature). Figure D.1 shows the schematic operation of the subroutine. If the space temperatures show mixed conditions the subroutine sets the mixed layer height to zero and calculates a mixed temperature. |
| <i>CalcCrossVent RE</i> | Subroutine for CVmodeling for the “corridor like” flow pattern case. This subroutine calculates the surface heat transfer coefficients and room air equivalent temperatures for surface heat transfer and two space temperatures (the jet outlet temperature and the mean jet temperature). Figure D.2 shows the schematic operation of the subroutine. |
| <i>CalcCrossVent CR</i> | Subroutine for CVmodeling for the recirculating flow pattern case. This subroutine calculates the surface heat transfer coefficients and room air equivalent temperatures for surface heat transfer and two space temperatures (the jet outlet temperature and the mean recirculation temperature). |
| <i>HcUnmixFlow</i> | Main subroutine for convection calculation, used by all unmixed-flow models. This subroutine calls three other subroutines (HcFromSurface, HcToSurface and HcVertical) containing the convection heat transfer algorithms. The room surface air temperature array is calculated. Depending on what model is being used the subroutine uses different calculation methods to obtain the total convection transfer with the room surfaces. |
| <i>HcUnstable</i> | Calculates convection heat transfer for horizontal surfaces in cases where surface convection generated airflow moves away from the surface (heated floor or cooled ceiling). |
| <i>HcStable</i> | Calculates convection heat transfer for horizontal surfaces in cases where surface convection generated airflow moves into the surface (heated ceiling or cooled floor). |
| <i>HcVertical</i> | Calculates convection heat transfer for vertical surfaces. A surface is considered vertical whenever its tilt is above 10°. |

Table D.2. *New outputs of the displacement ventilation model.*

| Model | Outputs |
|--------------------------|--|
| Displacement Ventilation | Floor level temperature (TFLOOR). Temperature in the intermediate layer (TOC). Temperature in the upper mixed layer (TMX). Height of the upper, mixed layer. Maximum and average temperature gradient in the occupied zone (between 0 and 2m). Ratio between current inflow into the room and minimum predicted flow to maintain the mixed layer above 1.5m (measured from the room floor). Mixing flag, equal to one whenever the displacement model predicts a mixed flow. |

Table D.3. *New outputs of the CV model.*

| Model | Outputs |
|-----------------------------|--|
| Cross Ventilation Case R | Zone, Average, Recirculation Region Temperature [°C] Zone, Average, Jet Region Temperature [°C] Zone, Average, Velocity of the air in the recirculation region [m/s] Zone, Average, Velocity of the air in the jet region [m/s] |
| Cross Ventilation Case C | Zone, Average, Room Air Temperature (case C) [°C] Zone, Average, Velocity of the air in the jet region (case R) [m/s] |

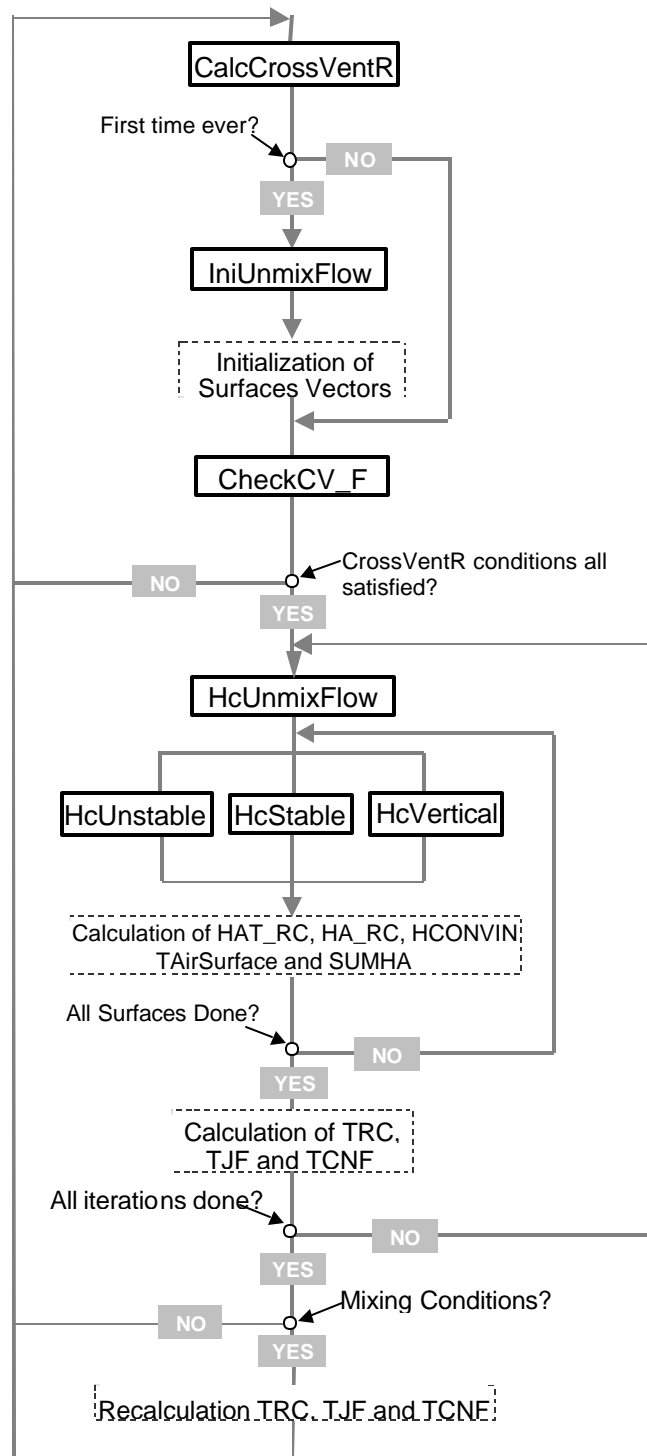


Figure D.1

Schematic operation sequence for the C—V case “R” modeling subroutine.

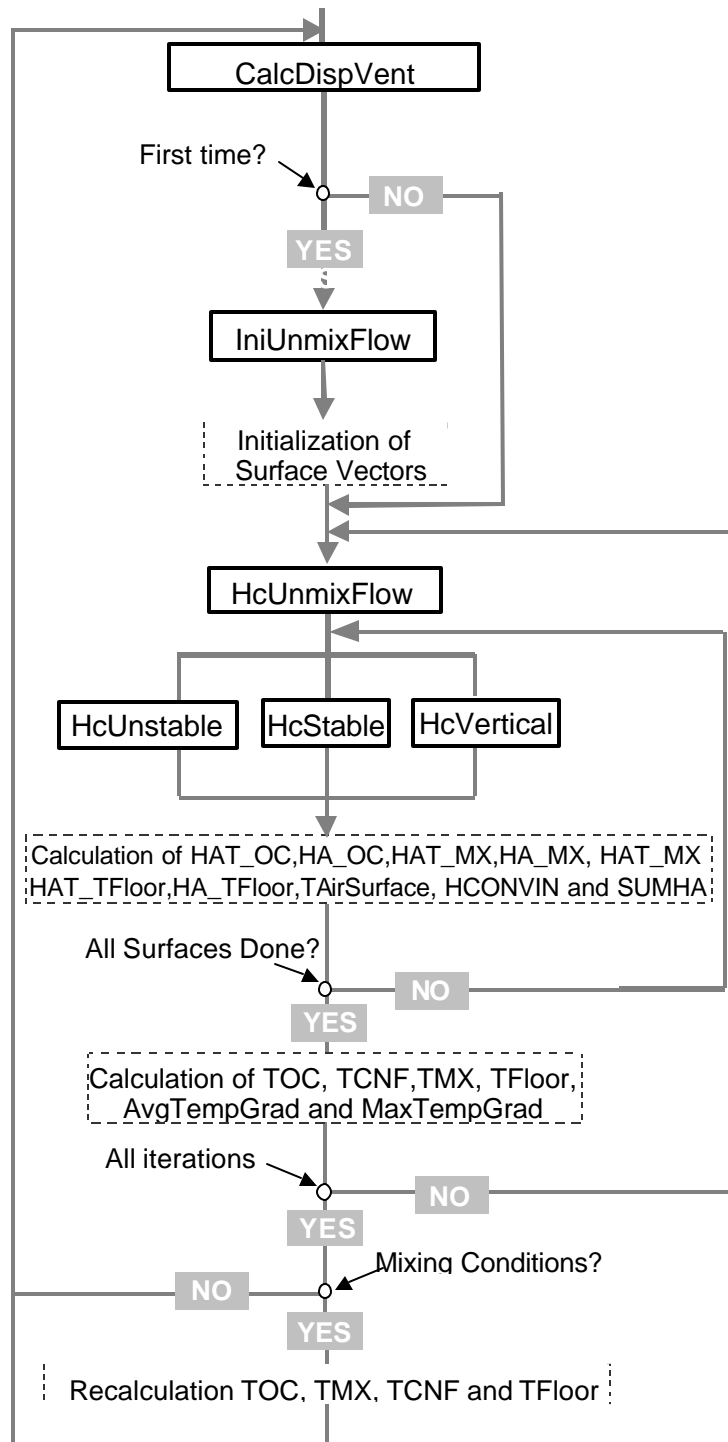


Figure D.2

Schematic operation sequence for the displacement ventilation modeling subroutine.

Implementation structure for the unmixed-flow pattern selection algorithm (FPS)

Figure D.3 shows the structure of the flow pattern selection algorithm (FPSA). The FPSA routine selects between four possibilities depending on a set of room geometry and airflow checks that are performed in four subroutines (CheckCV_F, CheckCV_B, CheckDV_F and CheckDV_B). These subroutines perform two types of checks:

Room geometry and inflow conditions evaluation (routines labeled “_F”).

Evaluation of buoyancy effects on the flow pattern (routines labeled “_B”).

Subroutine CheckDV_F

Purpose:

Identify dominant inflow aperture, check room geometry and airflow velocities.

Check:

Check if more than 90% of the inflow occurs at a height that is below 1m (measured from the room floor).

Check if more than 90% of the outflow occurs at a high that is above 2m (measured from the room floor). Set the maximum mixed layer height to the lowest value of all the outflow apertures.

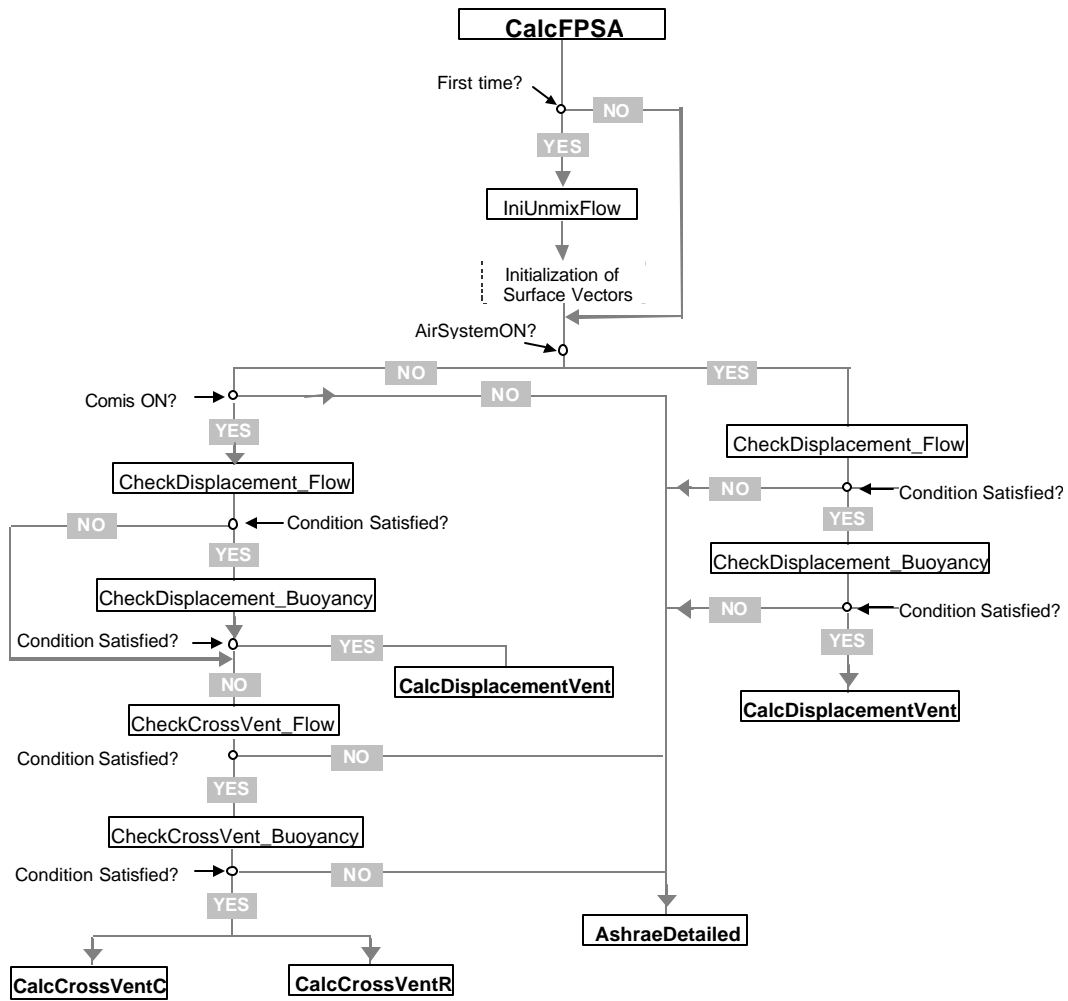


Figure D.3

Organization of the Flow Pattern Selection Algorithm subroutine (CalcFPSA)

Check if average inflow velocity is below 0.2m/s. Inflow velocity (V_{IN}) is calculated using:

$$V_{IN} = \frac{Q_{IN}}{A_{IN}} < 0.2 \text{ m/s} \quad (D.1)$$

Check if average floor level velocity (V_{FL}) is below 0.2m/s. Average floor level velocity is calculated supposing that the floor level boundary layer is 0.2m high. A characteristic floor width is calculated from the floor area:

$$V_{FL} = \frac{Q_{IN}}{0.2 * 4 * \sqrt{A_{RF}}} < 0.2 \text{ m / s} \quad (D.2)$$

If all checks are true, set the DV_F flag to TRUE.

Subroutine CheckCV_F

Purpose:

Identify dominant inflow aperture and select cross ventilation model that will be used.

Check:

Check if more than 90% of the inflow occurs through a single, dominant aperture (area A_{IN}).

Check if average inflow velocity for the dominant aperture is above 0.2m/s.

Check if more than 90% of the outflow occurs in the surface in front of the dominant aperture.

Check the ratio between inflow area and room cross section and decide on which CV model to use, case all other checks are “true”:

$$A^* = \frac{A_{IN}}{A_{CS}}, \begin{cases} A^* < 1/2, \text{ Set CV model to R} \\ A^* \geq 1/2, \text{ Set CV model to C} \end{cases} \quad (D.3)$$

If all checks are true, set the CV_F flag to TRUE.

Subroutine CheckDV_B

Purpose:

Calculate selected buoyancy driven flows that can disrupt the displacement flow

Check:

A= Sum of the absolute value of all buoyancy flows generated by vertical surfaces in the lower layer (flow rates are evaluated using expression C.9 in appendix C).

B= Sum of the absolute value of all negative buoyancy flows (surface temperature lower than air temperature) in the upper layer.

C= Calculate the total value of plume driven flow rate at room ceiling height, considering n floor level sources of buoyancy per occupant (an input field).

Logic structure for the checking process:

IF $(A+B)/C > 1/2$ THEN set the DV_B flag to FALSE, ELSE set the DV_B flag to TRUE

Subroutine CheckCV_B

Purpose:

Calculate selected buoyancy driven flows that can disrupt the cross ventilation flow

Check:

A= Sum of the absolute value of all buoyancy flows generated by all lateral flows (flow rates are evaluated using expression C.9 in appendix C).

C= Calculate the total value of plume driven flow rate at room ceiling height, considering n floor level sources of buoyancy per occupant (an input field).

Logic structure for the checking process:

For case CVR:

IF $(A+C) > F R$ THEN set the CV_B flag to FALSE, ELSE set the CV_B flag to TRUE

For case CVC:

IF $(A+C) > F$ THEN set the CV_B flag to FALSE, ELSE set the CV_B flag to TRUE

References.

Allard, F., Inard, C., Natural and Mixed Convection in Rooms, Prediction of Thermal stratification and Heat Transfer By Zonal Models, Proceedings of ISRACVE, pp. 335-342, Tokyo, 1992. Published by ASHRAE, USA

Altmayer, E.F., Gadgil, A.J., Bauman, F.S., Kammerud, R.C., Correlations for convective heat transfer from room surfaces. ASHRAE Transactions, No. 2764.

ASHRAE Handbook of Fundamentals, American Society of Heating Refrigerating and Air-Conditioning Engineers, Atlanta, GA, 2001.

Awbi, H.B. & Hatton, A., Mixed convection from heated room surfaces, Energy and Buildings, 32, (2000) 153-166.

Awbi, H.B. & Hatton, A., Natural convection from heated room surfaces, Energy and Buildings, 30, (1999) 233-244.

Awbi, H. B., Calculation of convective heat transfer coefficients of room surfaces for natural convection. Energy and Buildings 28 (1998).

Aynsley, R.M. 1999. Unresolved Issues in Natural Ventilation for Thermal Comfort, Technical Paper, First International One day Forum on Natural and Hybrid Ventilation, HybVent Forum'99, Sydney, Australia.

Aynsley, R.M., Melbourne, W., Vickery, B.J., Architectural Aerodynamics. Applied Science London (1977).

Aynsley, R. M.. A Resistance Approach to Estimating Airflow Through Buildings with Large Openings Due to Wind. ASHRAE Transactions (1988), 1661-1668.

Baines, W.D., Turner, J.S., Trubulent buoyant convection from a source in a confined region, J. Fluid Mech., Vol. 37, 51-80 (1968).

Baturin, V. V. , Billington, N. S., Fundamentals of Industrial Ventilation, Franklin Book Company 1972, pp. 174-179.

Bejan, A. 1994., Convection Heat Transfer 2nd ed, Wiley, USA.

Carrilho da Graça, G., Chen, Q., Gliksman, L.R., Norford, L.K.. Simulation of wind-driven ventilative cooling systems for an apartment building in Beijing and Shanghai. Energy and Buildings 1354 (2001), 1-11.

Chandra, S., Kerestecioglu, A.A., Heat transfer in naturally ventilated rooms data from full-scale measurements, ASHRAE Transactions, Volume 90, part 1b (1984) 211-224.

Cook M.J., Lomas K.J. (1998). Buoyancy Driven Displacement Ventilation Flows: Evaluation of Two Eddy Viscosity Turbulence Models for Prediction. Building Services Engineering Research and Technology, Vol. 19, No. 1, pp. 15-21. ISSN 0143-6244.

Cooper, P. & Linden, P.F., Natural ventilation of an enclosure containing two buoyancy sources. Journal of Fluid Mechanics, CUP, 311, 1996, p 153-176.

Crawley, D.B, Winkelmann, F.C., Lawrie, L.K., and Pedersen, C.O., "EnergyPlus: New Capabilities in a Whole-Building Energy Simulation", Proceedings of Building Simulation '01, IBPSA, Rio de Janiero, Brazil. 2001.

Dominique, M., Guitton, P. Validation of Displacement ventilation simplified models. Proceedings of building simulation 1997.

Eckert, E.R.G., Jackson, T.W.. Analysis of turbulent free-convection boundary layer on flat plate. Report 1015, National Advisory Committee for Aeronautics, Washington, DC, 1951.

EnergyPlus: A New-Generation Building Energy Simulation Program, Proceedings of R.A.E.S., 1999, Hawaii.

Ernest, D.R., Bauman, F.S., Arens, E.A., The Prediction of Indoor Air Motion for Occupant Cooling in Naturally Ventilated Buildings. ASHRAE Transactions 1991, 525-538.

Etheridge, D, Sandberg, M., 1996. Building Ventilation: Theory and Measurement. Wiley.

Feustel, H.E., Dieris, J. A survey of air flow models for multizone structures LBL-30288. Lawrence Berkeley National Laboratory. Springfield, Virginia: National Technical Information Service, 1991.

Givoni, Man, B., Climate and Architecture. 2d ed. Essex, England: Applied Science, 1976.

Henks, R.A.W.M., Hoogendoorn, C.J., Comparison of turbulence models for the natural convection boundary layer along a heated vertical plate, International Journal of Heat and Mass Transfer 32 (1989), 157-169.

Holford, J.M., Hunt, G.R. & Linden, P.F., Competition between heat sources in a ventilated space. Proceedings of RoomVent 2002, 2002, p 577-580.

Huang, J., Winkelmann, F.C., Buhl, W.F., Pedersen, C.O., Fisher, D., Liesen, R., Taylor, R., Strand, R., Crawley, D.B. and Lawrie, L.K., "Linking the COMIS Multi-zone Air Flow Model with the EnergyPlus Building Energy Simulation Program," Proceedings of Building Simulation '99, IBPSA, Kyoto, Japan. 1999.

Hunt, G.R., Holford, J.M. & Linden, P.F., Characterization of the flow driven by a finite area heat source in a ventilated enclosure. Proceedings of RoomVent 2002, 2002, p 581-584.

Hunt, G.R. & Linden, P.F. Steady-state flows in an enclosure ventilated by buoyancy forces assisted by wind. *J. Fluid Mech.*, 426, 2001, p 355-386.

Hussein, H.J., Capp, S.P., George W.K., Velocity measurements in a high-reynolds-number, momentum-conserving, axisymmetric, turbulent jet. *Journal of Fluid Mechanics*, 258:31, 1994.

Idelchik, IE. 1986. Handbook of hydraulic resistance, Hemisphere Pub. Corp., USA.

ISO. 1993. Moderate Thermal Environments – Determination of the PMV and PPD Indices and Specifications for Thermal Comfort, International Standard 7730, 1993.

Jackman, P., Air movement in rooms with sill mounted grilles – a design procedure. Laboratory report no. 65, Bracknell, UK, 1970.

Kalema, T., Haapala, T., Effect of interior heat transfer coefficients on thermal dynamics and energy consumption, *Energy and Buildings* 22 (2) (1995) pp. 101-113.

Kato, S., Murakami, S., Mochida, A., Akabayashi, S., Tominaga, Y., Velocity-pressure Field of CV with Open Windows Analyzed by Wind Tunnel and Numerical Simulation. *Journal of Wind Eng. And Industrial Aerodynamics.*, 41-44 (1992) 2575-2586.

Kaye, K.N., Linden, P.F., Coalescing axisymmetric turbulent plumes. In preparation for submission to the *Journal of Fluid Mechanics*

Klein, S. A., Duffie, J.A., and Beckman, W.A., " TRNSYS - A Transient Simulation Program," *ASHRAE Transactions*, 82, 623 (1976).

Lam, C.K.G., Bremhost, K., A modified form of the K- ϵ model for predicting wall turbulence, Transactions of ASME, J. Fluids Eng. 103 (1981), 456-460.

Launder, B.E., & Spalding, D.B., The numerical computation of turbulent flows, Computational Methods in Applied Mechanics & Engineering., Vol.3, pp269, (1974).

Linden, P.F. The fluid mechanics of natural ventilation. *Theoretical & Applied Mech.*, Eds. T. Tatsumi, E. Watanabe & T. Kambe, Elsevier, 1996 pp. 551-566.

Linden, P.F, 2000 Convection in the environment. In *Perspectives in Fluid Mechanics*, Eds. Batchelor, G.K, Moffatt, H.K. & Worster, M.G, Cambridge University Press, pp. 287-343.

Linden, P.F. & Cooper, P., Multiple sources of buoyancy in a naturally ventilated enclosure. Journal of Fluid Mechanics, CUP, 311, 1996, p 177-192.

Linden, P.F., Lane-Serff, G.F. & Smeed, D.A., Emptying filling boxes: the fluid mechanics of natural ventilation, Journal of Fluid Mechanics, CUP, 212, 1990, p 300-335.

Malmstrom, T.G., Kirkpatrick, A.T., Christensen, B., Knappmiller, K.. Centerline velocity decay measurements in low-velocity axisymmetric jets, J. Fluid Mech. 346, 363, 1997.

Morton, B.R., Taylor, G.I. & Turner, J.S., Turbulent gravitational convection from maintained and instantaneous sources. Proceedings of the Royal Society of London. 1956 A 234 (1196), p 1-23.

Mundt, E., The Performance of Displacement Ventilation Systems – Experimental and Theoretical Studies, Ph. D. Thesis. Bulletin N38, Building Services Engineering KTH, 1996, Stockholm.

Murakami, S., Kato, S., Akabayashi, S., Mizutani, K., Kim, Y.-D., Wind Tunnel Test on Velocity-Pressure Field of CV with Open Windows. ASHRAE Transactions: Symposia (1991), USA 525-538.

Neiswanger, L., Johnson, G.A., Carey, V.P., An experimental study of high Raleigh number mixed convection in a rectangular enclosure with restricted inlet and outlet openings. Transactions of ASME, Vol. 109, 1987, 446-453.

Nielsen, P.V., The selection of turbulence models for prediction of room airflow. ASHRAE Transactions, 104, Pt 1B, 1119-1127 (1998)

Ohba, M., Irie, K., Kurabuchi, T., Study on airflow characteristics inside and outside a CV model, and ventilation flow rate using wind tunnel experiments. Journal of Wind Engineering and Industrial Aerodynamics, in press, 2001.

PHOENICS Version 3.3. 2000. CHAM Ltd., London, UK.

Pope, S.B., Turbulent Flows, Cambridge University Press (2000).

Rees, S.J., McGuirk J.J. and Haves P. 2001. Numerical Investigation of Transient Buoyant Flow in a Room with a Displacement Ventilation and Chilled Ceiling System. Int. Journal of Heat and Mass Transfer, Vol. 44, No.6, pp. 3067-3080.

Rees, S.J. & Haves, P. 2001. A Nodal Model for Displacement Ventilation and Chilled Ceiling Systems in Office Spaces. Building and Environment, Vol.36, No.6, pp. 753-762.

Siebers, D. L., Schwind, R. G., Moffat, R. J., 1983, Experimental Mixed Convection Heat Transfer From a Large Vertical Surface in a Horizontal Flow. SAND 83-8225, Sandia National Laboratories, Livermore CA.

Skistad, H., Mundt, E., Nielsen, P., Hagstrom, K. & Railio, J., Displacement ventilation in non-industrial premises. REHVA Guidebook N1, 2002, Brussels.

Spitler, J. D., Pedersen, C.O., Fisher, D.E., Interior Convective Heat Transfer in Buildings with Large Ventilative Flow Rates. ASHRAE Transactions, Vol. 97, Pt.1(1991), pp. 505-515.

Swami, H.V., Chandra, S., Procedures for calculating natural ventilation flow rates in buildings. Final report FSEC-CR-163-86. Florida Solar Energy Center. Cape Canaveral, FL (1987).

Tennekes, H., & Lumley, J.L., A First Course in Turbulence, Cambridge: The MIT Press, 1994.

Wells, M.G., Griffiths, R.W. & Turner, J.S. Competition between distributed and localized buoyancy fluxes in a confined volume, Journal of Fluid Mechanics, CUP, 311, 1999, p 319-336.

Wilcox, DC. 2000. Turbulence modeling for CFD. DCW Industries, La Canada, USA (2000).

Winkelmann, F.C., Birdsall, B.E., Buhl, W.F., Ellington, K.L., Erdem, A.E., Hirsch, J.J., Gates, S.. DOE-2 Supplement, Version 2.1E, LBL-34947, Lawrence Berkeley National Laboratory. Springfield, Virginia: National Technical Information Service, 1993.

Wolfram, S. Mathematica 3.0. Wolfram Research, 1999.

Yap, C., Turbulent heat and momentum transfer in recirculating and impinging flows, PhD Thesis, Faculty of Technology, University of Manchester, (1987).